

REPORT DOCUMENTATION PAGE

AFRL-SR-AR-TR-04-

Public reporting burden for this collection of information is estimated to average 1 hour per response, including the time for reviewing instructions, searching existing data sources, gathering the data, reviewing the collection of information, and completing the collection of information. Send comments regarding this burden estimate or any other aspect of this collection of information, including suggestions for reducing the burden, to Washington Headquarters Service, Directorate for Information Operations and Reports, 1215 Jefferson Davis Highway, Suite 1204, Arlington, VA 22202-4302, and to the Office of Management and Budget, Paperwork Project Director (0304-0188), Washington, DC 20503.

and reviewing
information

1. AGENCY USE ONLY (Leave blank)		2. REPORT DATE February 25, 2004	3. REPORT TYPE AND DATES COVERED Final Technical Report (1 Nov 99 - 31 Oct 02)
4. TITLE AND SUBTITLE Directionally Solidified Eutectic Ceramics: In-Situ Composites for High Temperature Structural Applications			5. FUNDING NUMBERS F49620-00-1-0048 2302/CX 61102F
6. AUTHOR(S) Ali Sayir			
7. PERFORMING ORGANIZATION NAME(S) AND ADDRESS(ES) Case Western Reserve University Dept of Materials Science and Engineering Cleveland, OH 44106			8. PERFORMING ORGANIZATION REPORT NUMBER
9. SPONSORING/MONITORING AGENCY NAME(S) AND ADDRESS(ES) AFOSR/NA 4015 Wilson Blvd., Room 713 Arlington, VA 22230-1954 Program Manager: Dr. Joan Fuller			10. SPONSORING/MONITORING AGENCY REPORT NUMBER
11. SUPPLEMENTARY NOTES			
12a. DISTRIBUTION AVAILABILITY STATEMENT APPROVED FOR PUBLIC RELEASE, DISTRIBUTION IS UNLIMITED			12b. DISTRIBUTION CODE
13. ABSTRACT (Maximum 200 words) Eutectics are multiphase structures formed by the cooperative growth of two or more phases. Although the internal structure can vary widely, the development of continuous rods or plates in a matrix can be achieved and, within limits, can be controlled or "tailored" through directional solidification. The eutectic architecture of a continuous reinforcing phase within a higher volume phase or matrix, can be described as a naturally occurring in-situ composite. In-situ composites have been demonstrated to possess mechanical properties intermediate between monolithic materials and man-made composites and therefore may produce low cost high temperature structural material. Although several eutectic systems are currently being studied, two eutectics systems Al ₂ O ₃ /RE ₃ Al ₅ O ₁₂ (RE = Y, Er, Gd, Nd, Ho, Eu) and Al ₂ O ₃ /ZrO ₂ (Y ₂ O ₃) have been selected for the detailed examination of the advantages and the challenges associated with directional solidification. The Al ₂ O ₃ /Y ₃ Al ₅ O ₁₂ is comprised of two highly creep resistance oxides whereas Al ₂ O ₃ /ZrO ₂ (Y ₂ O ₃) combines a highly creep resistant material (Al ₂ O ₃) with one having very poor creep properties (c-ZrO ₂ (Y ₂ O ₃)). To elucidate the potential of this family of materials for high temperature applications, parallel research efforts at different organizations are integrated. The ongoing research is closely coordinated with the efforts of Dr. S. C. Farmer at NASA Glenn Research Center (GRC), Prof. A. S. Argon at Massachusetts Institute of Technology (MIT) and Prof. E. Dickey at Penn State University (PSU). The efforts at MIT focuses on the high deformation characteristics of directionally solidified Al ₂ O ₃ /ZrO ₂ (Y ₂ O ₃). The efforts at PSU focuses on the correlation of interface structure and bonding from the atomistic length scale.			
14. SUBJECT TERMS			15. NUMBER OF PAGES
			16. PRICE CODE
17. SECURITY CLASSIFICATION OF REPORT U			18. SECURITY CLASSIFICATION OF THIS PAGE U
19. SECURITY CLASSIFICATION OF ABSTRACT U			20. LIMITATION OF ABSTRACT

20040311 052

DIRECTIONALLY SOLIDIFIED EUTECTIC CERAMICS; *IN-SITU* COMPOSITES FOR HIGH TEMPERATURE STRUCTURAL APPLICATIONS

AFOSR GRANT #F49620-00-1-0048

ABSTRACT

Ali Sayir

Department of Materials Science and Engineering
Case Western Reserve University, Cleveland, Ohio.

Eutectics are multiphase structures formed by the cooperative growth of two or more phases. Although the internal structure can vary widely, the development of continuous rods or plates in a matrix can be achieved and, within limits, can be controlled or "tailored" through directional solidification. The eutectic architecture of a continuous reinforcing phase within a higher volume phase or matrix, can be described as a naturally occurring *in-situ* composite. In-situ composites have been demonstrated to possess mechanical properties intermediate between monolithic materials and man-made composites and therefore may produce low cost high temperature structural material.

Although several eutectic systems are currently being studied, two eutectics systems $\text{Al}_2\text{O}_3/\text{RE}_3\text{Al}_5\text{O}_{12}$ ($\text{RE} = \text{Y, Er, Gd, Nd, Ho, Eu}$) and $\text{Al}_2\text{O}_3/\text{ZrO}_2(\text{Y}_2\text{O}_3)$ have been selected for the detailed examination of the advantages and the challenges associated with directional solidification. The $\text{Al}_2\text{O}_3/\text{Y}_3\text{Al}_5\text{O}_{12}$ is comprised of two highly creep resistance oxides whereas $\text{Al}_2\text{O}_3/\text{ZrO}_2(\text{Y}_2\text{O}_3)$ combines a highly creep resistant material (Al_2O_3) with one having very poor creep properties ($\text{c-ZrO}_2(\text{Y}_2\text{O}_3)$). To elucidate the potential of this family of materials for high temperature applications, parallel research efforts at different organizations are integrated. The ongoing research is closely coordinated with the efforts of Dr. S. C. Farmer at NASA Glenn Research Center (GRC), Prof. A. S. Argon at Massachusetts Institute of Technology (MIT) and Prof E. Dickey at Penn State University (PSU). The efforts at MIT focuses on the high deformation characteristics of directionally solidified $\text{Al}_2\text{O}_3/\text{ZrO}_2(\text{Y}_2\text{O}_3)$. The efforts at PSU focuses on the correlation of interface structure and bonding from the atomistic length scale.

Research Objective

The objectives of this program are: (i) to develop directionally solidified eutectic ceramics with high strength, superior creep resistance and toughness, and (ii) to formulate *in-situ* composite mechanics for multiphase structures. The focus of the proposed project is to examine polyphase material systems across a broad compositional and therefore microstructural range, which includes but is not limited to eutectic growth (i.e. off-eutectic and eutectic materials).

$\text{Al}_2\text{O}_3/\text{ZrO}_2(\text{Y}_2\text{O}_3)$ System

Al_2O_3 - $\text{ZrO}_2(\text{Y}_2\text{O}_3)$ eutectic material exhibit a minimum creep rate of 10^{-9} s^{-1} under 50 MPa and 10^{-5} under 300 MPa load at 1400 °C. These values are better than the creep value

expected for off-axis sapphire but substantially below c-axis Al_2O_3 creep values. Increasing the amount of Al_2O_3 , the more creep resistant phase, is one means to improve the high temperature creep resistance of Al_2O_3 - ZrO_2 (Y_2O_3) eutectic materials. Mechanical properties are expected to be affected not only by the volume per cent of Al_2O_3 but also by the ZrO_2 polymorph. The creep resistance of c- ZrO_2 at 1400 °C exhibits a two-fold increase in flow stress with increase in solute content due to solid solution hardening [1]. Partially stabilized ZrO_2 (cubic plus tetragonal polymorphs) crept under similar conditions shows potent high temperature precipitation hardening [2]. The purpose of this study was to examine the effect of increasing Y_2O_3 addition on the room temperature tensile strength of an Al_2O_3 - ZrO_2 material containing excess Al_2O_3 . Results on mechanical properties and microstructures of these materials were used to define compositions for creep testing in future work at MIT. Al_2O_3 - ZrO_2 is of fundamental interest for creep studies as it combines a creep resistant material, Al_2O_3 , with a very low creep resistance material, ZrO_2 .

The range of compositions studied was selected so that materials with distributions of both tetragonal ZrO_2 and cubic ZrO_2 could be examined [3]. The 68 m/o Al_2O_3 32 m/o ZrO_2 composition is calculated to have ~77 volume per cent Al_2O_3 , a 10 volume per cent increase relative to the 62 m/o Al_2O_3 (~67 volume per cent) eutectic composition [4]. Adding Y_2O_3 affects both the ZrO_2 polymorph(s) and the phase content. Y_2O_3 is soluble in Al_2O_3 at the ppm level. Therefore the 1.1 m/o Y_2O_3 ternary corresponds to a 3.5 m/o ZrO_2 (Y_2O_3) solid solution and is expected to be tetragonal. The 3.2 m/o Y_2O_3 materials, a 10 m/o ZrO_2 (Y_2O_3) solid solution, are expected to be fully cubic- ZrO_2 . The 5.1 m/o Y_2O_3 composition lies adjacent to the boundary of the Al_2O_3 + ZrO_2 + $\text{Y}_3\text{Al}_5\text{O}_{12}$ ternary phase field [3] and some $\text{Y}_3\text{Al}_5\text{O}_{12}$ formation will occur. The 7.6 m/o Y_2O_3 composition lies well within the ternary field. Additionally, x moles of Y_2O_3 yield a 2x mole increase in ZrO_2 solid solution. So even with no $\text{Y}_3\text{Al}_5\text{O}_{12}$ formation, the volume percent of Al_2O_3 continuously decreases from its maximum value of 77 percent.

The study examined fracture strength of directionally solidified 68 m/o Al_2O_3 hypoeutectic compositions at varying Y_2O_3 contents (Figs. 1 and 2). The Y_2O_3 content had a pronounced effect on the microstructure and fracture characteristics. Both the degree of supercooling caused by Y_2O_3 additions and the degree of solute rejection to the colony boundary regions were profound, Figs. 3 and 5. This effect was underestimated in the design of this study. Hypoeutectic materials with Al_2O_3 contents intermediate between 68 m/o and the 62 m/o Al_2O_3 eutectic composition and with minimal Y_2O_3 contents will be pursued in further studies. The Al_2O_3 - ZrO_2 (Y_2O_3) materials were highly tolerant of growth defects maintaining an average strength of 1 GPa in the presence of pores and large shrinkage cavities, which extend with crack-like morphology along the fiber axis, Fig. 4. Critical defects were external facets for specific compositions (Fig. 6), intercolony pores and other stress concentrators contained within the low toughness Al_2O_3 phase that is in residual tension.

$\text{Al}_2\text{O}_3/\text{Er}_3\text{Al}_5\text{O}_{12}$ System

A systematic study has been initiated aimed at identifying the sources of high levels of creep resistance in the directionally solidified $\text{Al}_2\text{O}_3/\text{Er}_3\text{Al}_5\text{O}_{12}$ system. The results presented here are part of a broader research effort involving the study of single crystals of Al_2O_3 , $\text{Er}_3\text{Al}_5\text{O}_{12}$, directionally solidified eutectic and hypoeutectic compositions of the $\text{Er}_3\text{Al}_5\text{O}_{12}/\text{Al}_2\text{O}_3$ system. We first report the results on creep experiments of directionally solidified $\text{Al}_2\text{O}_3/\text{Er}_3\text{Al}_5\text{O}_{12}$ fibers at the Al_2O_3 rich region of the Al_2O_3 - Er_2O_3 phase diagram [5] followed by discussion of deformation study of the eutectic composition. There are no previous deformation studies on the $\text{Al}_2\text{O}_3/\text{Er}_3\text{Al}_5\text{O}_{12}$ eutectic systems and the hypoeutectic solidification in this system has not been previously explored.

A representative cross-section of directionally solidified $\text{Al}_2\text{O}_3/\text{Er}_3\text{Al}_5\text{O}_{12}$ hypoeutectic ceramic is shown in Fig. 7. The microstructure consists of Al_2O_3 cells (black contrast) as the major component and $\text{Er}_3\text{Al}_5\text{O}_{12}$ (white contrast) or $\text{Al}_2\text{O}_3/\text{Er}_3\text{Al}_5\text{O}_{12}$ eutectic boundaries (black/white contrast). The cell size ranges between 10 and 30 μm with size increasing toward the center of the fiber. Figure 8 shows the longitudinal section of a representative fiber. The Al_2O_3 cells have large aspect ratios with lengths ranging from 100 μm to 1 mm. The cells are longer and wider in the center of the fiber due to the reduced thermal gradient in the center of the molten zone during fiber growth.

Under applied stress, the fibers show a short primary creep regime (decreasing creep rate) followed by a constant strain rate creep regime that lasts for deformations up to 1%. Typically two apparent steady-states were obtained in each experiment. The steady-stage creep stage ends with an acceleration of the deformation prior to fracture. The $\text{Al}_2\text{O}_3/\text{Er}_3\text{Al}_5\text{O}_{12}$ system exhibits remarkable creep resistance. The $\text{Al}_2\text{O}_3/\text{Er}_3\text{Al}_5\text{O}_{12}$ system with hypoeutectic composition results in a unique cellular microstructure with Al_2O_3 cells having aspect ratios up to 100. The creep resistance of the hypoeutectic $\text{Al}_2\text{O}_3/\text{Er}_3\text{Al}_5\text{O}_{12}$ system is comparable to that of c-axis sapphire and is four orders of magnitude better than 15° off axis sapphire as shown in Fig. 9. The high creep resistance of these fibers is even more remarkable because the Al_2O_3 cells must have some degree of misalignment. The differences in phase spacing between the Al_2O_3 and $\text{Er}_3\text{Al}_5\text{O}_{12}$ components are believed to create a unique response for each phase and superior creep resistance of the system. In the Al_2O_3 cells the dislocations may glide without great difficulty until they reach an interface where they may pile up. Transmission electron microscopy studies are necessary to reach unambiguous conclusions about the effect of the microstructure on test results.

The deformation study of the eutectic composition augmented our understanding about the mechanism of the deformation. The materials produced at the invariant eutectic point of $\text{Al}_2\text{O}_3/\text{Er}_3\text{Al}_5\text{O}_{12}$ system had a fine interpenetrating microstructure (Fig. 10) with a typical phase spacing of 0.5 μm and aspect ratio 10. The creep resistance of eutectic $\text{Al}_2\text{O}_3/\text{Er}_3\text{Al}_5\text{O}_{12}$ is two orders of magnitude better than hypoeutectic $\text{Al}_2\text{O}_3/\text{Er}_3\text{Al}_5\text{O}_{12}$ at 1400 $^\circ\text{C}$. This is due to lower phase spacing of the Al_2O_3 phase and increased volume fraction of creep resistant $\text{Er}_3\text{Al}_5\text{O}_{12}$ phase. At low stress levels, the creep rate decreases monotonically with time ($<10^{-10} \text{ s}^{-1}$). This transitory regime occurs in both compositions, and may last up to 0.1 % of deformations and up to 50 hours. It may give an erroneous appearance of steady state creep deformation. At high stress levels, the system reaches an apparent steady state and deformation continues until failure. There is a regime of accelerated creep prior to failure in most of the experiments (some cases up to 0.5 % strain at 10 hours). In conclusion, the system does not reach steady state. TEM analysis of the deformed specimens revealed the dislocation activity was contained only in the Al_2O_3 phase and was very limited. The absence of dislocations on the deformed specimen and the particular characteristic of the transitory creep leads to the conclusion that creep is controlled by diffusion.

Future studies will concentrate on several fundamental aspects of directionally solidified eutectic ceramics. The completion of TEM studies of crept specimens are necessary to elucidate creep characteristic (phenomenological understanding of stress relaxation phenomena) and coarsening will be described. Further studies will concentrate on strengthening the Al_2O_3 phase and increasing the amount of crack deflection experienced at the $\text{Al}_2\text{O}_3\text{-ZrO}_2$ and $\text{Al}_2\text{O}_3/\text{RE}_3\text{Al}_5\text{O}_{12}$ interfaces through use of dopants in order to achieve a combination of high strength and an acceptable toughness.

Tensile Strength

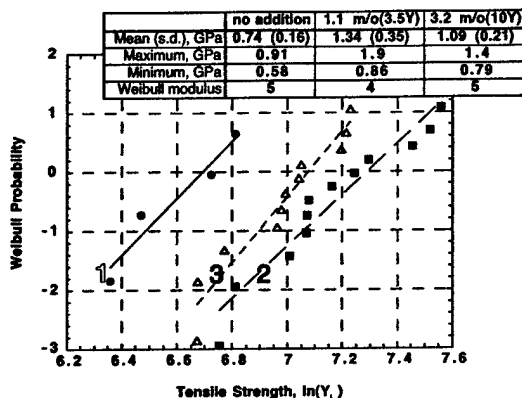


Fig.1 Weibull probability plot of tensile strength for (1) 0 m/o, (2) 1.1 m/o and (3) 3.2 m/o Y_2O_3 compositions.

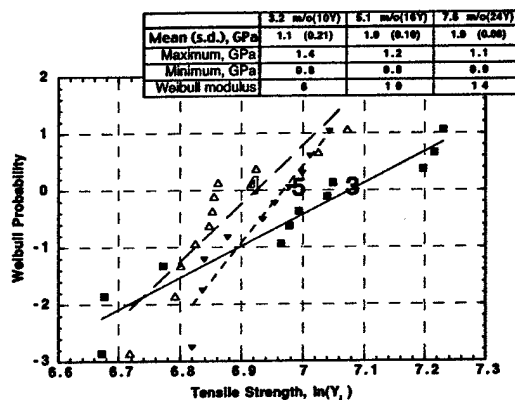


Fig. 2 Weibull probability plot of tensile strength for (4) 3.2 m/o, (5) 5.1 m/o and (6) 7.6 m/o Y_2O_3 compositions.

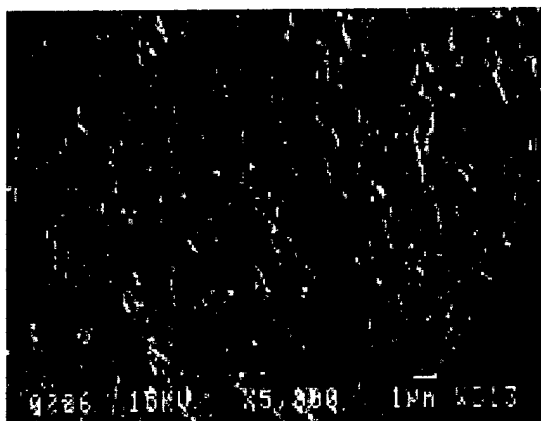


Fig.3 Fine lamellar microstructure of eutectic material, 62 m/o Al_2O_3 - 38 m/o ZrO_2 .

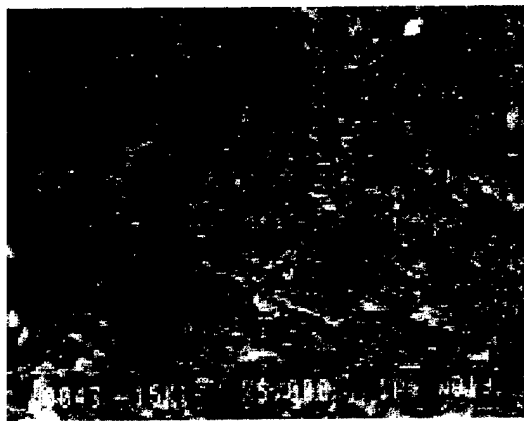


Fig.4 Banded lamellar microstructure of alumina rich material, 68 m/o Al_2O_3 - 32 m/o ZrO_2 .

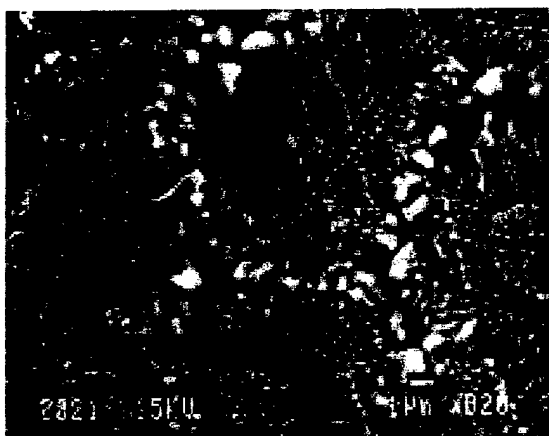


Fig.5 Primary fracture surface in central fiber region. Fracture occurs within Al_2O_3 with minimal deflection.



Fig.6 7.6 m/o Y_2O_3 material. $Y_3Al_5O_{12}$ solidifies within intercolony regions along with smaller (lighter contrast) ZrO_2 particles.

REFERENCES

- [1] A. Dominguez-Rodriguez, A.H. Heuer and J. Castaing, "dislocations and the Mechanical Properties of Stabilized ZrO_2 , *Rad. effect. and Def. in Sol.*, 119-121, 759-569 (1991).
- [2] A. Dominguez-Rodriguez, V. Lanteri and A.H. Heuer, "High Temperature Precipitation Hardening of Two-Phase Y_2O_3 Partially-Stabilized ZrO_2 Single Crystals: A first Report", *J. Am. Ceram. soc.*, 69[3], 285-287 (1986).
- [3] L.M. Lopato, L.V. Nazarenko, G.I. Gerasimiyuk and A.V. Shevchenko, "Interaction in ZrO_2 - Y_2O_3 - Al_2O_3 System at 1650°C", *Inorg. Matl.* 26[4] 701-704 (1990).
- [4] G.R. Fischer, L.H. Manfredo, R.N. McNally and R.C. Doman, "The Eutectic and Liquidus in the Al_2O_3 - ZrO_2 System" *J. Mat. Sci.*[16] 3447-3451 (1981).
- [5] P. Wu and A. D. Pelton, "Coupled Thermodynamic-Phase Diagram Assessment of the Rare Earth oxide-aluminium Oxide Binary Systems", *J. of alloys and Compounds*, 179 (1992) 259-287.
- [6] G.S. Corman, "High Temperature Creep of Some Single Crystals Oxides", *Ceram. Eng. Sci. Proc.* 12 [9-10] (1991) 1745.
- [7] R. J. Garboraud, "Fluage Haute Temperature du Sesquiosy d'Ytrium: Y_2O_3 ", *Phil Mag*, 44A [3] (1981) 561.
- [8] A.H. Clauer and B.A. Wilcox, "High Temperature Tensile Creep of Magnesium Oxide Single Crystals", *J. Am. Ceram. Soc.*, 59 [3-4] (1976) 89.
- [9] L.E. Matson and N. Hecht, "Microstructural Stability and Mechanical Properties of Directionally Solidified Alumina/YAG Eutectic Monofilaments", *J. Europ. Ceram. Soc.*, 19 (1999) 2487.
- [10] D. Gómez García, J. Martínez Fernández, A. Domínguez Rodríguez and J. Castaing, "Mechanisms of High Temperature Creep Behaviour of Fully Stabilized Zirconia Single Crystals as a Function of the Ytria Content", *J. Am. Ceram. Soc.* Vol. 80, pp.1668-72 (1997).
- [11] A. Sayir, in *Computer Aided Design of High-Temperature Materials*, "Directional Solidification of Eutectic Ceramics," Eds.A. Pechenik, R. K. Kalia, and P. Vashista, Oxford University Press (1999)197 - 212.

PERSONNEL SUPPORTED

Ali Sayir	PI (10 %)
J. Martínez Fernández	Research Associate (100%)
Fred. W. Dyns	Research Associate (15%)

PUBLICATIONS

A. Sayir and S. C. Farmer, "The Effect of the Microstructure on Mechanical Properties of Directionally Solidified $\text{Al}_2\text{O}_3/\text{ZrO}_2(\text{Y}_2\text{O}_3)$ Eutectic," *Acta Mat.*, 48 (2000) 4691 - 4697.

A. Sayir, "Directionally Solidified Eutectic Ceramics," in Proc. 10th International Metallurgy and Materials Congress, Istanbul (Chamber of Metallurgical Eng. Turkey, Publ. 37, 2000) pp.480-484. (Invited Paper)

J. W. Palko, W. M. Kriven, S.V. Sinogeikin, J. D. Bass, and A. Sayir, "Elastic Constants of Yttria (Y_2O_3) Monocrystals to High Temperatures," *J. Appl. Physics*, 89 [12] (2001) 7791-7796.

A. Sayir and S. C. Farmer, "Fracture Characteristic of Single Crystal and Eutectic Fiber, " accepted for publication as Book Chapter in "*FIBRE FRACTURE*" Elsevier (2001).
(Invited Paper)

S. C. Farmer and A. Sayir, "Tensile Strength and Microstructure of $\text{Al}_2\text{O}_3\text{-ZrO}_2$ Hypo-eutectic Fibers" accepted in Publication in *Int. J. Fracture* (2001)

J. M. Fernández and A. Sayir, "Creep of Directionally Solidified $\text{Al}_2\text{O}_3/\text{Er}_3\text{Al}_5\text{O}_{12}$ Fibers with Hypo-Eutectic Composition," in press in *Ceram. Eng. & Sci. Proc.*, (2001).

C. Frazer, E. Dickey and A. Sayir, "Crystallographic Texture and Orientation Variants in $\text{Al}_2\text{O}_3/\text{Y}_3\text{Al}_5\text{O}_{12}$ Directionally Solidified Eutectic Crystals," accepted publication in *J. Crystal Growth* (2001).

A. S. Argon, J. Yi and A. Sayir, "Creep Resistance of Directionally Solidified Ceramic Eutectics of $\text{Al}_2\text{O}_3/\text{c-ZrO}_2$ with Sub-micron Columnar Morphologies" in print in *Materials Science and Engineering*, (2001).

AWARDS RECEIVED

(Best Poster Award)

J. M. Fernández and A. Sayir, "Creep of Directionally Solidified $\text{Al}_2\text{O}_3/\text{Er}_3\text{Al}_5\text{O}_{12}$ Fibers with Hypo-Eutectic Composition," *Int. Conf. on Advanced Ceramics & Composites Meeting*, (2001).



Pergamon

Available online at www.sciencedirect.com

SCIENCE @ DIRECT®

Acta Materialia 51 (2003) 1705–1720



www.actamat-journals.com

High temperature creep deformation of directionally solidified $\text{Al}_2\text{O}_3/\text{Er}_3\text{Al}_5\text{O}_{12}$

J. Martinez Fernandez^{abc,*}, A. Sayir^{ab}, S.C. Farmer^a

^a NASA Glenn Research Center, 21000 Brookpark Road, Cleveland, OH 44135, USA

^b Case Western Reserve University, Cleveland, OH 44135, USA

^c Departamento de Física de la Materia Condensada, Universidad de Sevilla, Seville, Spain

Received 12 September 2002; received in revised form 13 November 2002; accepted 30 November 2002

Abstract

The microstructure of directionally solidified $\text{Al}_2\text{O}_3/\text{Er}_3\text{Al}_5\text{O}_{12}$ (19.5 mol% Er_2O_3) is analyzed and high temperature creep deformation studied using fibers in tension between 1400° C and 1550° C. The directionally solidified $\text{Al}_2\text{O}_3/\text{Er}_3\text{Al}_5\text{O}_{12}$ system is an in situ composite and has a fine eutectic- microstructure with sub-micron phase spacing. The microstructure is elongated in the direction of growth. Transmission electron microscopy observations revealed well-bonded interfaces and scatter within the crystallographic alignment of the constituent phases. The creep resistance of the system was very high, comparable to c-axis sapphire, and failure initiated at the lamella interfaces. The influence of the different elastic and plastic behaviors of the eutectic components on creep is examined. A critical discussion on the origin of the high stress dependence of the creep rate, the existence of steady state creep, and the relevant microscopic deformation mechanisms is presented.

© 2003 Acta Materialia Inc. Published by Elsevier Science Ltd. All rights reserved.

Keywords: Creep; High temperature; Eutectic; Strain recovery

1. Introduction

The eutectic architecture of a continuous reinforcing phase within a continuous higher volume phase or matrix can be considered as a naturally occurring in situ composite. Directionally solidified eutectic ceramics show superior creep resistance and attractive high temperature strength reten-

tion [1–13] but a clear explanation of the origin for the superior mechanical properties is not available.

A systematic study has been initiated at NASA Glenn Research Center aimed at identifying the sources of high levels of creep resistance in directionally solidified in situ composites. Directional solidification at compositions near the eutectic composition produces very fine microstructures, whereas solidification at off-eutectic compositions alters both the size and volume fraction of each phase. Directional solidification over a selected composition range of the phase field produced microstructures ranging from the 100 nm scale at the eutectic composition to 50 μm at strongly

* Corresponding author. Tel.: +34-954-556-956; fax: +34-954-612-097.

E-mail address: martinez@us.es (J. Martinez Fernandez).

hypo-eutectic compositions (cellular microstructure) [6, 7, 14]. The nature of the interphase-interfaces [1, 3, 13] is not expected to change during solidification at different volume fraction of the phases, or at eutectic or hypoeutectic compositions. The focus of this article is on the deformation characteristic of the $\text{Al}_2\text{O}_3/\text{Er}_3\text{Al}_5\text{O}_{12}$ system near the eutectic region and the effect of volume fraction (lamella dimensions) at hypoeutectic compositions will be presented in a future article.

The $\text{Al}_2\text{O}_3/\text{Er}_3\text{Al}_5\text{O}_{12}$ composition was selected to examine intrinsic characteristics of the directionally solidified $\text{Al}_2\text{O}_3/\text{garnet}$ systems. There are no previous deformation studies on the $\text{Al}_2\text{O}_3/\text{Er}_3\text{Al}_5\text{O}_{12}$ system. Data on the $\text{Al}_2\text{O}_3/\text{Y}_3\text{Al}_5\text{O}_{12}$ system is available [1, 2, 8, 12] and provides a basis for comparison with different $\text{Al}_2\text{O}_3/\text{rare-earth garnet}$ systems. The approach for the use of monofilaments has been adopted to permit a uniaxial tension test that provides data regarding the intrinsic potential of the $\text{Al}_2\text{O}_3/\text{Er}_3\text{Al}_5\text{O}_{12}$ system.

2. Experimental procedure

$\text{Al}_2\text{O}_3/\text{Er}_3\text{Al}_5\text{O}_{12}$ fibers (19.5 mol% Er_2O_3) were grown by the laser heated float zone method in air as described in previous publications [5, 6]. The source rods were prepared by extrusion without pre-sintering. To initiate directional solidification, a seed of single crystal $\langle 0001 \rangle$ Al_2O_3 was used. The pulling rate was the same for all the fibers (38 cm/h). The monofilament diameter ranged from 140 to 160 μm (typical diameter oscillation of approximately 10 microns along the fiber) with lengths up to 40 cm.

Tensile creep deformation was studied using dead-weight loads and cold grips at elevated temperatures. Most of the deformation experiments were run in air placing the central part of the fiber in a MoSi_2 furnace (CM. Inc., Bloomfield, NJ, USA) with a 2.5 cm hot zone. The monofilament was protected with a high purity polycrystalline alumina or sapphire tube to eliminate any interaction with the heating elements and to thus minimize fiber contamination. Experiments in vacuum

were run using a tantalum furnace (Oxy-gon Industries Inc, Epsom, NH, USA) with a 7 cm hot zone. The use of a vacuum environment eliminates the strain reading noise caused by oscillations of the room temperature and by the flow of hot air. This is very critical for the accurate study of loading transients and creep recovery. The test temperatures ranged from 1400° C to 1550° C. The applied stresses ranged from 80 to 500 MPa. The elongation was measured with a linear variable differential transducer (LVDT).

The microstructures of as-fabricated and deformed monofilaments, mounted in epoxy resin and polished, were studied by scanning electron microscopy (SEM). The small diameter monofilament geometry was particularly effective in that it cools rapidly. Quenching better retains the high temperature microstructure. Specimens were thinned to electron transparency and studied using transmission electron microscopy (TEM). Special care was taken when preparing TEM foils from crept samples. A precision ion thinner was used and the electron transparent regions were obtained at distances less than 2 mm from the fracture surface.

3. Results

3.1. As-fabricated microstructure

A representative cross-section of directionally solidified $\text{Al}_2\text{O}_3/\text{Er}_3\text{Al}_5\text{O}_{12}$ ceramic is shown in Fig. 1. The microstructure consists of alternating lamellae of Al_2O_3 (black contrast) and $\text{Er}_3\text{Al}_5\text{O}_{12}$ (white contrast). The $\text{Er}_3\text{Al}_5\text{O}_{12}$ volume fraction calculated from the area fraction on SEM micrographs is $60.4 \pm 8.6\%$, the scatter being due to variation between sectional cuts of the fiber. The microstructure consists of eutectic regions and erbium-rich precipitates indicating that the selected composition (the eutectic composition on the phase diagram [15]) lies slightly outside the cooperative growth region of this system for the processing conditions used. The average lamellae widths for Al_2O_3 and $\text{Er}_3\text{Al}_5\text{O}_{12}$ phases were $0.31 \pm 0.23 \mu\text{m}$ and $0.46 \pm 0.35 \mu\text{m}$, respectively. Figure 2 shows a representative longitudinal section. The cells are

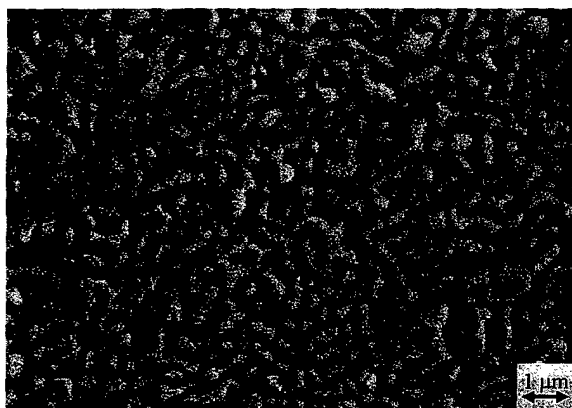


Fig. 1. SEM micrograph of directionally solidified $\text{Al}_2\text{O}_3/\text{Er}_3\text{Al}_5\text{O}_{12}$ cross-section showing the complexity of the fine interlocking microstructure. The white regions are garnet and the black regions are alumina.

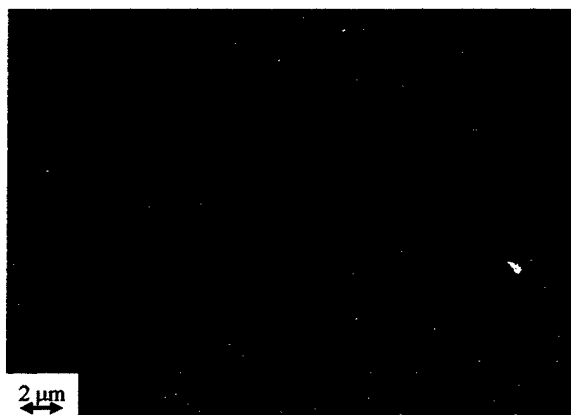


Fig. 2. SEM micrographs of directionally solidified $\text{Al}_2\text{O}_3/\text{Er}_3\text{Al}_5\text{O}_{12}$ longitudinal section showing that the microstructure is elongated in the direction of growth. The tri-dimensional continuity of the phases is clear from Figs 1 and 2.

elongated in the direction of growth with aspect ratios between 5 to 25. In many areas, however, it was difficult to assign an aspect ratio due to the tri-dimensional continuity of the phases.

There is scatter in the crystallographic orientation between Al_2O_3 and $\text{Er}_3\text{Al}_5\text{O}_{12}$ erbium aluminum garnet.¹ In Fig. 3 some frequently found orientations are shown: c-axis in the alumina

¹ Garnet will be used from now on to refer to erbium aluminum garnet phase.

lamella is forming 5° – 10° with the fiber axis (zone axis $[2\bar{1}10]$ at 5° from the foil plane), and garnet with the $[110]$ direction parallel to the fiber axis (zone axis $[01\bar{1}]$ perpendicular to foil plane). Additional orientations further off-axis than shown in Fig. 3 are also found. The crystallographic orientations of neighboring lamellae of the same phase are similar, indicating that change of orientation within a phase occurs gradually. TEM observations indicate that the interfaces are sharp, suggesting a strong bonding between phases.

3.2. Tensile creep deformation

The creep curves show a primary creep regime where the creep rate decreases continuously. Figure 4 shows a typical creep deformation curve at low stress (190 MPa at 1400°C) where the creep rate decreases to the limit of detection ($\approx 5 \times 10^{-10} \text{ s}^{-1}$), with total plastic strains of about 0.05%. When the applied stress is higher (433 MPa at 1400°C), the system reaches a quasi-steady state deformation up to failure at total strains of approximately 0.2%, Fig. 5.

Whether or not a portion of the creep curve appears linear over a certain time interval depends on the time scale of the creep curve. The quasi-steady-state regime in this work is determined by plots of the strain-rate against the true strain as suggested by Poirier [16]. The creep deformation rate, however, was history dependent. Experiments in which the stress and/or temperature was changed and subsequently returned to the initial stress and temperature levels exhibited strain rates markedly lower than the original strain rates at a given stress or temperature condition (Fig. 6). This indicates that a true stationary-state was not reached and the prefix quasi is used to describe the observed deformation regions. Quasi-steady-state strain characteristics of the directionally solidified ceramics gave additional impetus to include the raw data shown in Figs 4 and 5 for completeness.

The $\text{Al}_2\text{O}_3/\text{Er}_3\text{Al}_5\text{O}_{12}$ system exhibits remarkable creep resistance and requires very high loads to initiate deformation. Figure 7 shows the quasi-steady-state creep rates for the temperature and stress regimes tested. The creep rate is very sensitive to the applied stress, having a power law fit

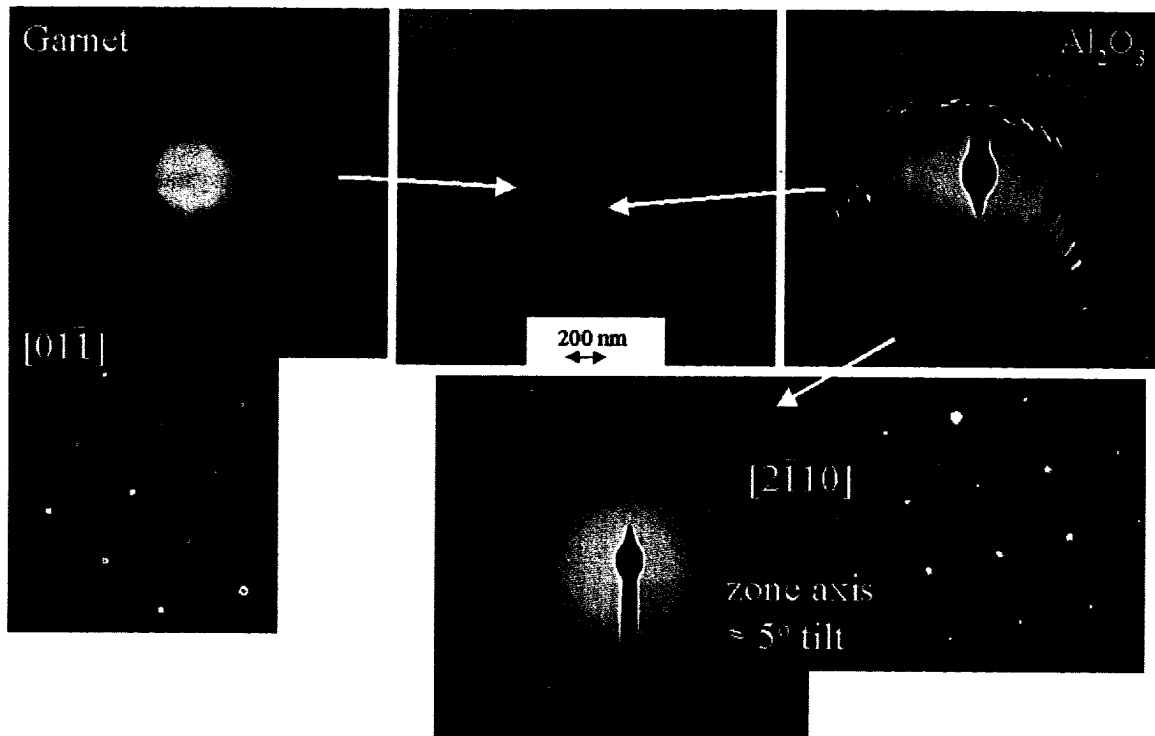


Fig. 3. TEM micrographs of the as-fabricated microstructure (foil prepared in the longitudinal direction, the white regions are alumina and the black regions are garnet). Diffraction patterns are included. In the case of the alumina region the diffraction pattern after tilting to a low index region is also included. The monofilament axis is parallel to the $[110]$ direction in garnet and forms 5° – 10° with the c -axis in alumina.

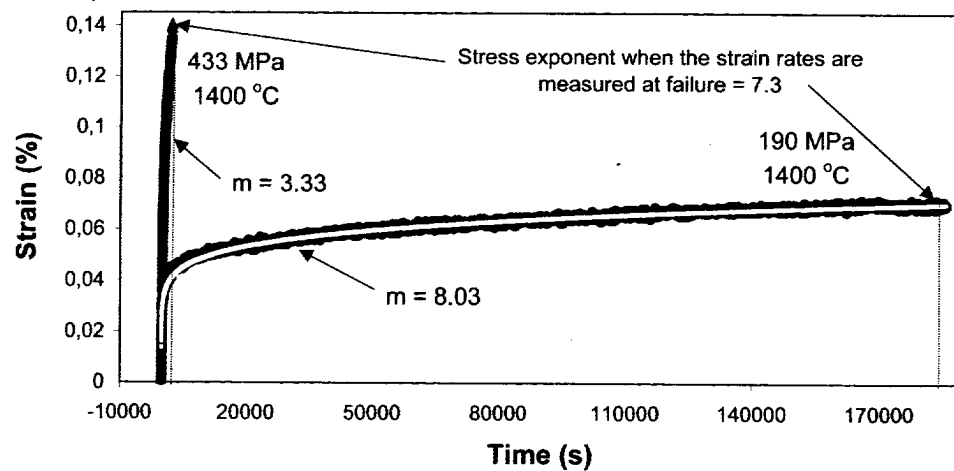


Fig. 4. Creep curve at 1400°C under a stress of 190 MPa. The curve of Fig. 5 is also included to illustrate the calculation of the stress exponent from the creep rates at failure. Because deformation occurs in the primary creep regime, the stress exponent obtained this way is overestimated.

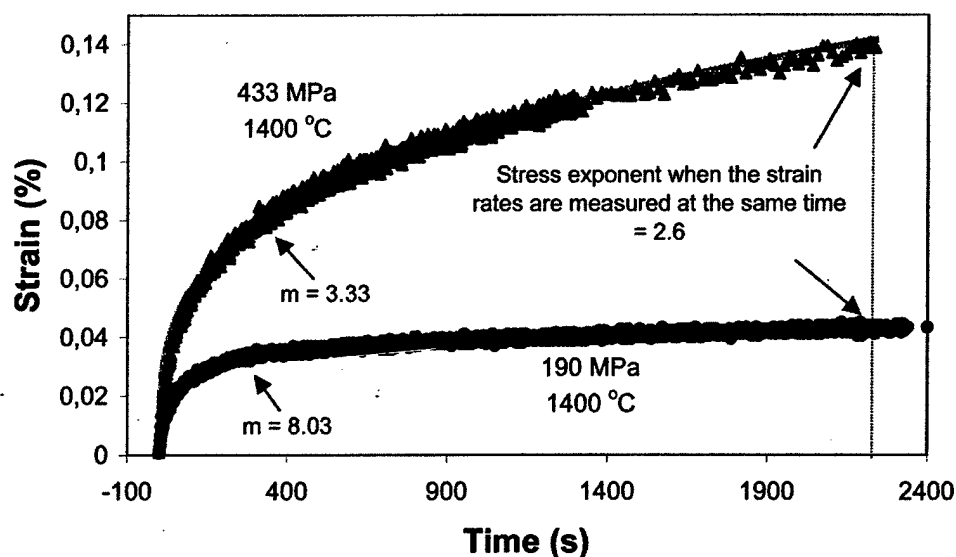


Fig. 5. Creep curve at 1400° C under a stress of 430 MPa. The curve of Fig. 4 is also included to illustrate the calculation of the stress exponent at a given time. This is a more accurate way to calculate the stress dependence of strain rate when deformation occurs in the primary creep regime.

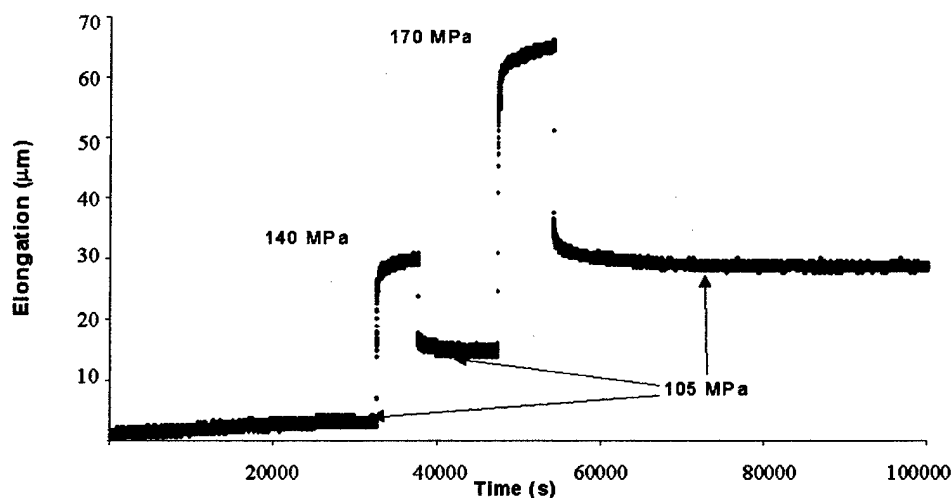


Fig. 6. Creep curve at 1400° C with load increments and decrements. The strain rate at 105 MPa decreases after the first load increments (140 MPa), and creep recovery (contraction of the monofilament) is observed after the 170 MPa load increment. Creep recovery is due to the release of elastic stresses built up in the garnet phase during deformation.

with a high exponent (between 4 to 5). The scatter in the data is largely attributed to the non-uniformity of the fiber diameter. The stress exponent is also determined by incremental application of the load during one single experiment. The incremental load approach gave a similar stress exponent

$n=4.1$, $R^2=0.9999$. In Fig. 7, the data points obtained from a single specimen by incremental loading mode at 1500° C have been included for comparison (dashed line). The activation energy obtained by temperature increments at constant load was 5.1 eV (492 kJ mol^{-1} , $R^2=0.9778$), Fig. 8.

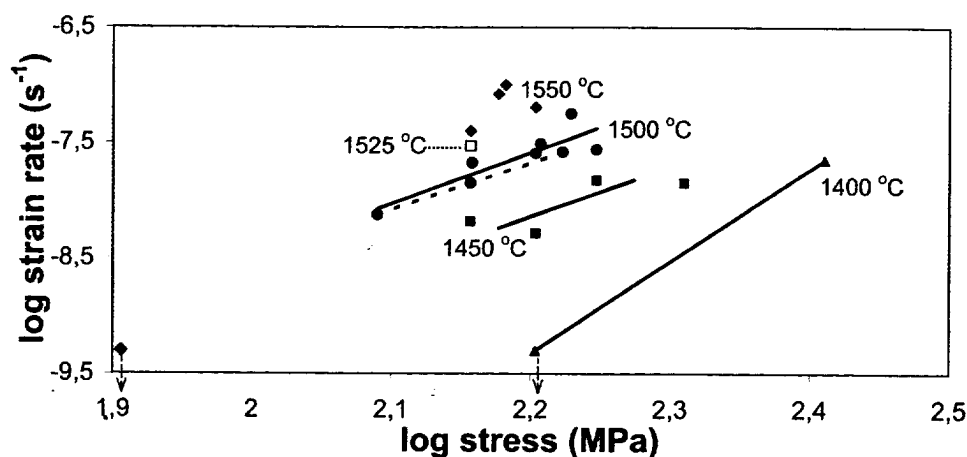


Fig. 7. Plot of the creep rates before failure versus stress (the arrow indicates that a strain rate was not measurable). The data points marked with a dashed line are obtained from the same experiment giving a stress exponent of 4.1 ($R^2=0.999$).

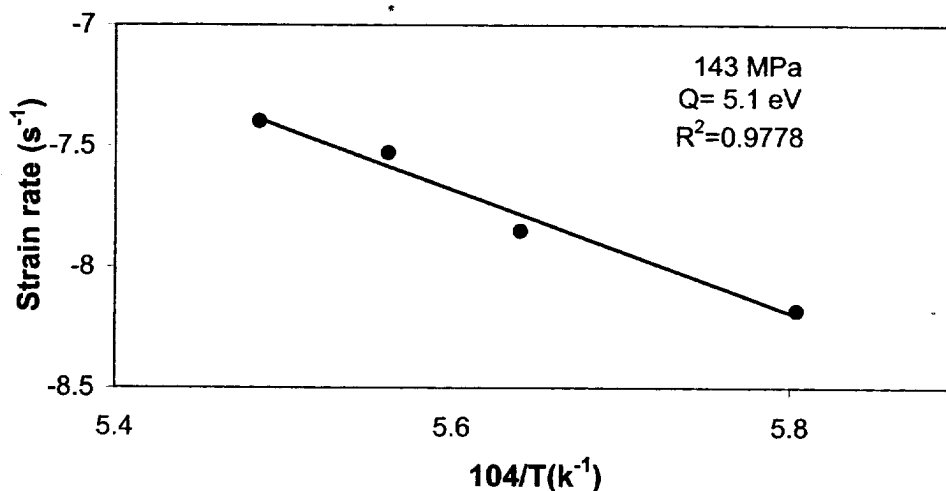


Fig. 8. Plot of the creep rates versus the reciprocal of the temperature for experiments at constant load with temperature increments. The activation energy for creep is compatible with the diffusion data available for different species in alumina and garnet [25, 27].

In Fig. 9, the strain rate at 100 MPa is plotted as a reciprocal of the absolute temperature. The normalized strain characteristic of $\text{Al}_2\text{O}_3/\text{Er}_3\text{Al}_5\text{O}_{12}$ at 100 MPa was calculated using a stress exponent of 4.5. Data from the literature in other oxide ceramics is also included for comparison [6, 8, 17–20]. The creep resistance of the $\text{Al}_2\text{O}_3/\text{Er}_3\text{Al}_5\text{O}_{12}$ system is very high, comparable to c-axis sapphire up to 1550 °C. The extrapolation of the data on sapphire is indicated with a dashed line. The high creep resistance of $\text{Al}_2\text{O}_3/\text{Er}_3\text{Al}_5\text{O}_{12}$ system is even

more striking given that the Al_2O_3 lamella have some degree of misalignment. The creep resistance of Al_2O_3 decreases dramatically with small misalignments as indicated by the data included in Fig. 9. It must be noted that the creep resistance of the $\text{Al}_2\text{O}_3/\text{Er}_3\text{Al}_5\text{O}_{12}$ system is 3 or 4 orders of magnitude better than 15° off c-axis sapphire.² From the

² Data was normalized from 300 MPa to 100 MPa with a stress exponent of 4, typical on Al_2O_3 single crystals [17].

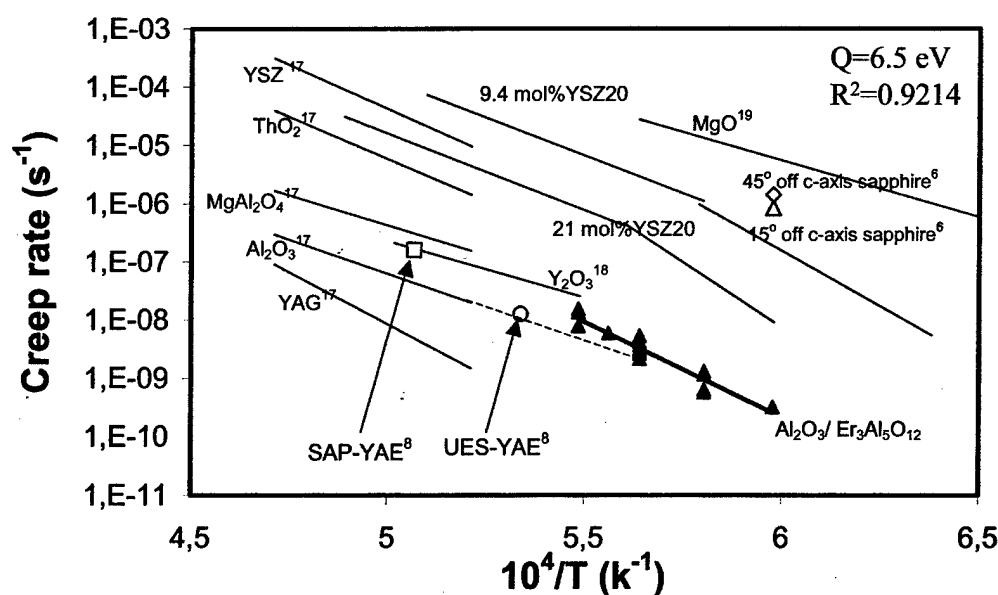


Fig. 9. Comparison of the creep rate versus reciprocal of temperature (normalized at 100 MPa) of the system studied in this work (black triangles) and other structural oxides [6, 17–20]. SAP and UES are commercial alumina-YAG fibers with eutectic composition [8]. The creep resistance of the $\text{Al}_2\text{O}_3/\text{Er}_3\text{Al}_5\text{O}_{12}$ is very high, comparable to c-axis sapphire (the extrapolation of the data on sapphire is indicated with a dashed line).

practical point of view, the $\text{Al}_2\text{O}_3/\text{Er}_3\text{Al}_5\text{O}_{12}$ system is superior to Al_2O_3 as its mechanical properties are not as sensitive as sapphire to small misalignments. The activation energy calculated from this plot is 6.5 eV (626 kJ mol^{-1} , $R^2=0.9214$). The incremental temperature calculation referred to previously (492 kJ mol^{-1} , $R^2=0.9778$) is more reliable because it does not require normalization with stress.

3.3. Microstructure of deformed specimen

Details of a representative fracture surface is shown in Fig. 10. The fracture surfaces are rough indicating that the damage propagation involves crack branching. At higher stress concentrations damage accumulation at the lamella interfaces most likely leads to failure originating at this boundary.

Extensive TEM observations were made in samples which were carefully thinned adjacent to the fractured surface of the specimens that were subjected to uniaxial deformation at temperatures from 1400°C to 1650°C . Very limited dislocation



Fig. 10. SEM micrograph of the fracture surface of a fiber crept at 1400°C . It can be seen how cracks propagate preferentially at the interfaces (arrowed). Damage is also probably nucleated at the interfaces due to the high shear stress associated to the different elastic and plastic properties of alumina and garnet phase.

activity is observed in Al_2O_3 lamella. The garnet phase was dislocation free, even at very high deformation loads (Fig. 11). Coarsening occurred during creep tests at temperatures above 1500°C (Fig.



Fig. 11. TEM micrograph of a region close to the fracture of a sample crept at 1400° C. A few scattered dislocations were found in alumina and none in garnet. Exhaustive TEM examination of crept samples at other temperatures resulted in similar observations.

12). The aspect ratios of the phases are dramatically reduced and the microstructure was equiaxed after thermal treatments of 1.5 h at 1650° C.

3.4. Strain recovery

Creep experiments show a very intriguing history-dependent behavior. After load increment and subsequent reduction of stress, the strain rates are lower than initially experienced at the same load (Fig. 6). If the previous load increment is large enough, one observes a transient regime that may last several hours during which contraction of the sample occurs (see last load decrement in Fig. 6). Specific experiments to confirm and further examine the extent of strain recovery were conducted (recovery creep has been reported in similar systems [21]). For example in an experiment, the initial deformation for 8 minutes at 510 MPa produced a total elongation of approximately 70 μm (0.1% strain). The load was subsequently decreased to a very low stress (15 MPa) at the

same temperature. After 16 h a recovery of approximately 50% of the creep elongation was observed. The strain recovery is clearly not elastic, but rather is associated with the release of constraints built up during creep. This phenomenon is under further study.

4. Discussion

4.1. Effect of load transfer on the creep behavior

The TEM observations indicate that the interfaces are well bonded (Fig. 3). This type of interface is typical of directionally solidified ceramic eutectics [1, 3, 13]. Both components have fine phase spacing and form a highly interconnected microstructure. Due to the isostrain condition imposed by the well-bonded nature of the interfaces and the different plastic and elastic properties of the two materials involved, load transfer occurs between the two phases during deformation. The challenge is then to explain the seemingly complex material response of directionally solidified eutectics and to highlight insights gained for this class of materials. To address this, we will first discuss the mechanical response of the $\text{Al}_2\text{O}_3/\text{Er}_3\text{Al}_5\text{O}_{12}$ eutectic within three different behavior regimes as defined by their observed response to load at elevated temperatures.

The three regions can be described as (Fig. 13):

- I. Both components are elastic. Alumina will carry more load due to its higher elastic modulus. This region is obtained instantaneously in a constant load experiment.
- II. Alumina reaches its plastic yield point and garnet is still deforming elastically. The stress must increase continuously in the garnet phase to attain a particular strain rate. There is then a load transfer from alumina to garnet.
- III. Both phases are deforming plastically. The stress is redistributed to fulfill the isostrain condition.

The load transfer of region II can be easily modeled. The strains of alumina and garnet in this region follow the relations,

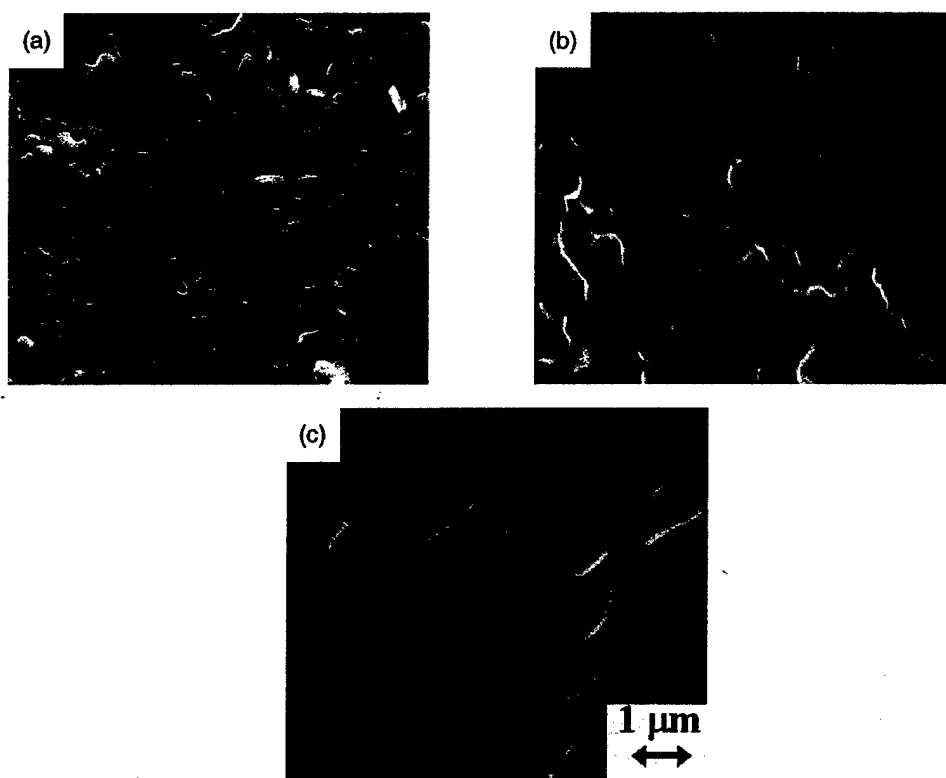


Fig. 12. SEM micrographs showing the microstructure after annealing. (A) 290 hours at 1400° C, (B) 3 hours at 1550° C, and (C) 1.5 hours at 1650° C. Microstructural coarsening is not detected at 1400° C even for very long annealing times. Over 1550° C coarsening of the microstructure is clear. All the micrographs are shown at the same scale.

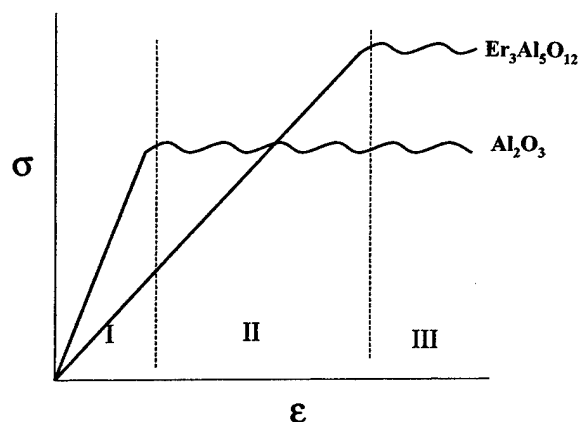


Fig. 13. Hypothetical stress-strain curve indicating the three stages of deformation discussed: Stage I, where both components are elastic, stage II, with alumina deforming plastically and garnet phase elastically, and stage III, where both components are deforming plastically.

$$\dot{\epsilon}_a = A_a \sigma_a^n; \dot{\epsilon}_g = E_g^{-1} \dot{\sigma}_g + A_g \sigma_g^n, \quad (1)$$

where $\dot{\epsilon}$ is the strain rate, σ the stress, E is the elastic modulus, and A the parameter relating the creep rate to the stress. The subscripts "a" and "g" refer to alumina and garnet. A typical power dependence of the strain rate with stress is assumed. In addition to the elastic component of the strain in garnet ($\epsilon_g = E_g^{-1} \sigma_g$), the contribution of a time dependent plastic strain is also included.

The isostrain condition requires the evolution of load transfer with time,

$$\dot{\epsilon}_a = \dot{\epsilon}_g \Rightarrow A_a \sigma_a^n = E_g^{-1} \dot{\sigma}_g + A_g \sigma_g^n, \quad (2)$$

$$\dot{\sigma} = \sigma_a V_a + \sigma_g V_g, \quad (3)$$

where $\dot{\sigma}$ is the average stress, V_a and V_g are the volume fraction of alumina and garnet, respectively.

The stresses in alumina and garnet then follow

the time dependence of $n=1$ based on the assumption that both single crystals deform by diffusional creep:

$$\sigma_g = \frac{\dot{\sigma}}{V_g + V_a \frac{A_g}{A_a}} \left(\frac{\dot{\sigma}}{V_g + V_a \frac{A_g}{A_a}} - \sigma_{g0} \right) \exp \left(-E_g \left(A_a \frac{V_g}{V_a} + A_g \right) t \right), \quad (4)$$

$$\sigma_a = \frac{\dot{\sigma}}{V_a} \left(1 - \frac{1}{1 + \frac{V_a A_g}{V_g A_a}} \right) - \frac{V_g}{V_a} \left(\frac{\dot{\sigma}}{V_g + V_a \frac{A_g}{A_a}} - \sigma_{g0} \right) \exp \left(-E_g \left(A_a \frac{V_g}{V_a} + A_g \right) t \right),$$

where the σ_{g0} is the stress at the beginning of region II in garnet.

Garnet is about two orders of magnitude more creep resistant than alumina at the temperatures of the tests [17], so it is plausible to neglect the effect of plastic deformation of garnet while this phase is still deforming elastically during region II. Equation (4) can then be written as,

$$\sigma_g = \frac{\dot{\sigma}}{V_g} - \left(\frac{\dot{\sigma}}{V_g} - \sigma_{g0} \right) \exp \left(-\frac{A_a V_g E_g}{V_a} t \right) \xrightarrow{t \rightarrow \infty} \frac{\dot{\sigma}}{V_g} \sigma_a \quad (5)$$

$$= \sigma_{a0} \exp \left(-\frac{A_a V_g E_g}{V_a} t \right) \xrightarrow{t \rightarrow \infty} 0,$$

where the σ_{a0} is the stress at the beginning of region II in alumina. There is a stress transfer from alumina to garnet during region II that will depend on their relative elastic and plastic properties.

Two situations may arise depending on the magnitude of external stresses and the minimum stress to produce a measurable strain rate in the garnet phase ($\sigma_{\min \text{ garnet}}$):

(A) If $(\dot{\sigma}/V_g) < \sigma_{\min \text{ garnet}}$, during the load transfer there is a decrease of the strain rate until it

goes under measurable values and plastic deformation will apparently stop.

(B) If $(\dot{\sigma}/V_g) > \sigma_{\min \text{ garnet}}$, both phases will deform plastically after the load transfer. The system could enter a quasi-steady-state regime if the microstructure were stable during deformation.

An estimation of the minimum stress to produce a measurable strain rate in $\text{Er}_3\text{Al}_5\text{O}_{12}$ can be obtained from the YAG single crystal data available in the literature [17]. The stresses necessary to achieve a strain rate of $5 \times 10^{-10} \text{ s}^{-1}$ for YAG are 240 and 130 MPa for temperatures of 1400° C and 1550° C, respectively. Based on the volume fraction of the YAG phase, the corresponding average stresses are 144 and 78 MPa. These stress levels were obtained by extrapolating the available creep data for [110] compression [17]. If the stresses are calculated for an average orientation, using the creep data for [100], [110], and [111] loading directions, only a variation of 5% (depending on temperature) is obtained because there is little anisotropy of the plastic behavior.

The strain-time behavior of region II can be expressed by:

$$\varepsilon_{\text{system}} = \varepsilon_g = \frac{\sigma_g}{E_g} \quad (6)$$

Figure 14 shows a typical transient regime at low stresses where the effect of the load transfer on the creep curve is more evident because the contribution of plasticity on garnet is negligible: 105 MPa at 1400° C. The best fit using equations (5) and (6) is also plotted ($R^2=0.960$) using the elastic modulus of $\text{Y}_3\text{Al}_5\text{O}_{12}$ garnet; 300 GPa [17] with the volume fraction $V_g=0.6$. This is a reasonable assumption since the elastic moduli of single crystal oxides does not differ within a family of crystal structures [22].

The calculated data from Fig. 14 for the initial stress in garnet phase (σ_{g0}) is 62 MPa with $A_a=6.17 \times 10^{-7} \text{ s}^{-1} \text{ GPa}^{-1}$. The values of E_g and σ_{g0} give compatible strains for regions I and II. The initial stress in garnet obtained from the fit is close to the stress redistribution that would be expected after region I, attributable to the differences in elastic modulus of sapphire and garnet ($E_{\text{sapphire}}=450$

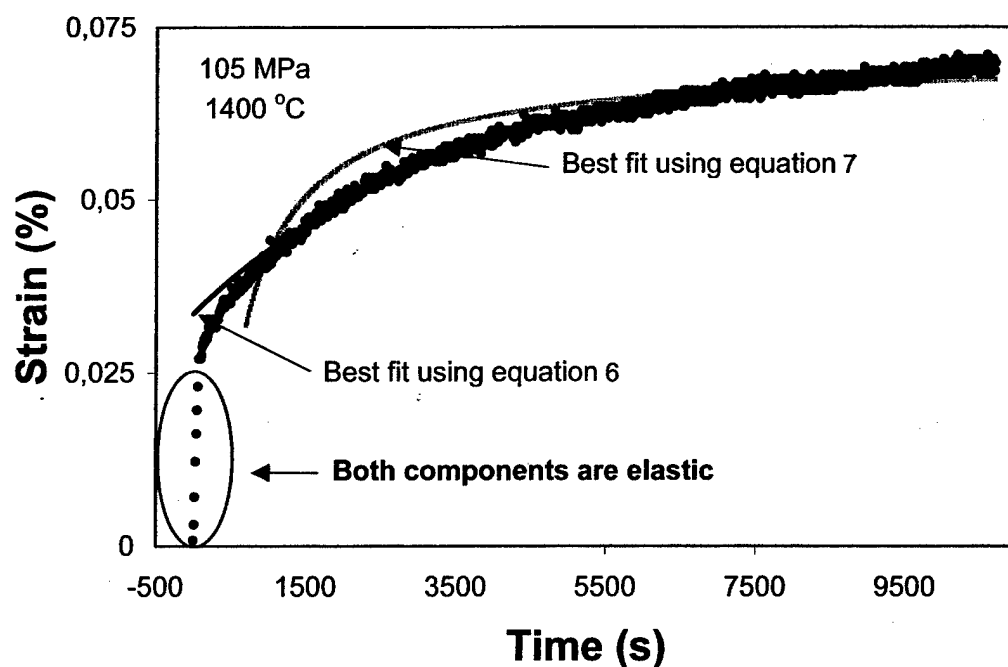


Fig. 14. Typical transient regime at low stresses where the effects of the load transfer on the creep curve are more evident as the contribution of plasticity of the garnet phase is negligible (105 MPa, 1400° C). Note that the best fit using equation (5) ($R^2=0.960$) lies within the scatter of the data for most of the strain. The best fit using equation (7) (assuming $n>1$, $R^2=0.804$) is also included. The good fit of equation (5) supports the hypothesis of load transfer and diffusional creep of alumina.

GPa) [13]. This distribution of stresses corresponds to the beginning of region II. The alumina creep constant (A_a) deduced from the fit gives reasonable values for the creep rates ($6.17 \cdot 10^{-8} \text{ s}^{-1}$ at 100 MPa and 1400° C) compared with the experimental quasi-steady-state creep rates. Yet, these values are lower than those obtained for diffusion controlled creep in polycrystalline alumina [23]. This is not surprising since the deformation of polycrystalline alumina includes a contribution from grain boundary sliding that is not viable as a mode of deformation in the directionally solidified eutectic system. This is the characteristic of the directionally solidified eutectic ceramics with unique interphase interfaces that is dissimilar from the grain boundaries of polycrystalline materials and requires further discussion (Section 4.2).

If the alumina phase is deforming with a stress exponent larger than one in region II, the expected

evolution of strain with time would follow an equation of the form:

$$\varepsilon = \alpha - (\beta + \gamma)^{1/(1-n)}, \quad (7)$$

where α , β , and γ are constants which depend on E_g , σ_{g0} , A_g and V_g .

The best fit obtained with equation (7) gave $n=2.19$ and $R^2=0.804$ (Fig. 14). Under the assumption of $n>1$, the stress exponent obtained is still fairly low. Hence, a better description of the strain-time dependence is obtained assuming that alumina deforms by diffusional creep. The diffusional nature of the deformation in relation to the lack of dislocation activity is further discussed.

Further understanding of the proposed model load transfer model was obtained by stress relaxation experiments. The recovery of creep strain after unloading is caused by the release of elastic stresses built up in the garnet phase during defor-

mation. The elastic stress is expected to cause contraction in the alumina and to recover part of the creep strain after removal of the applied external stress. The load transfer model can also provide an equation for strain recovery by changing the integration limits:

$$\begin{aligned}\dot{\epsilon}_a &= \dot{\epsilon}_g \Rightarrow A_a \sigma_a = E_g^{-1} \dot{\sigma}_g, \sigma_a = \sigma_g, \\ \epsilon &= \epsilon_0 \exp(-A_a E_g t),\end{aligned}\quad (8)$$

where ϵ_0 is the strain that is not recovered instantly. The best fit gives a product of $A_a E_g = 10^{-4} \text{ s}^{-1}$. The calculated value of A_a is $3.33 \times 10^{-7} \text{ GPa s}^{-1}$, which is in good agreement with the value previously calculated for the transients following loading. Due to the complexity of the microstructure, garnet may have undergone permanent deformation in some regions, which could then be responsible for the creep strain that is not recoverable. Some additional recovery may be obtained in longer experiments.

4.2. Comparison with the classical deformation models

The deformation mechanisms, which could be operating in the two-phase system under isostrain deformation conditions, can be classified in two categories: (a) diffusion controlled mechanisms and (b) dislocation controlled mechanisms.

4.2.1. (a) Diffusion mechanisms

Nix [24] derived an expression for the case of creep by bulk diffusion (Nabarro–Herring creep) including the effect of the aspect ratio of the grains:

$$\begin{aligned}\dot{\epsilon}_{\text{diffusion}} &= \frac{21}{d_{\text{effective}}^2} \left\{ \frac{(R_1 R_2)^{-2/3} (R_1^2 + R_2^2)}{1 + R_1^2 + R_2^2} \right\} \\ &\quad \frac{\Omega}{kT} \left\{ D_0 \exp\left(\frac{-Q}{kT}\right) \right\} \sigma, \\ R_1 &= \frac{W_1}{L}; R_2 = \frac{W_2}{L}; d_{\text{eff}} = (W_1 W_2 L)^{1/3},\end{aligned}\quad (9)$$

where Q is the activation energy for diffusion, W_1 , W_2 , and L are the dimensions of the grains in the two directions perpendicular to and in the direction parallel to the applied stress.

In Fig. 15 the creep rates expected from this model at 1500° C are plotted together with the experimental data at the same temperature. Both alumina and garnet are assumed to creep by lattice diffusion, $W_g = 0.46 \text{ } \mu\text{m}$, $W_a = 0.31 \text{ } \mu\text{m}$, and the aspect ratio is 10. There is a lack of data on cation diffusion for garnet (only anion diffusion data is available [25]). Therefore the cation diffusion coefficient was calculated from creep data on polycrystals [26], where creep has been proven to be controlled by bulk diffusion. The same approach was adopted for the diffusion coefficient measurements of alumina [23]. The distribution of stress between the two phases was calculated at each external stress to fulfill the isostrain condition.

The strain rate expected from this model is higher than the experimental ones. This could be due to several different factors:

- 1 *Overestimation of the diffusion data.* The diffusion data calculated from creep experiments in polycrystals has been reported to give high values. For example the oxygen diffusion coefficient calculated from creep data in alumina [23] is over three orders of magnitude higher than the values obtained from direct measurements [27]. If the same discrepancy were assumed to exist between the cation diffusion (the lowest diffusing species) and diffusion data calculated from creep data in garnet [25], the simulated and experimental values would be in much closer agreement (Fig. 15).
- 2 *There is no sliding at the interfaces.* Diffusion creep is strongly coupled with grain boundary sliding, as diffusion creep creates deformation of the grains that must be accommodated. Accommodation by sliding at interfaces is not occurring during deformation in the $\text{Al}_2\text{O}_3/\text{Er}_3\text{Al}_5\text{O}_{12}$ system. This creates a build up of stresses at the interfaces, and increasingly longer/less stress driven diffusion paths are necessary to cause deformation. The creep data from polycrystals used to calculate diffusion coefficients includes a component of the strain due to interfacial sliding that could contribute to the over estimation of the creep rate.
- 3 *The diffusion paths are longer.* The phases are tri-dimensionally interconnected. This intercon-

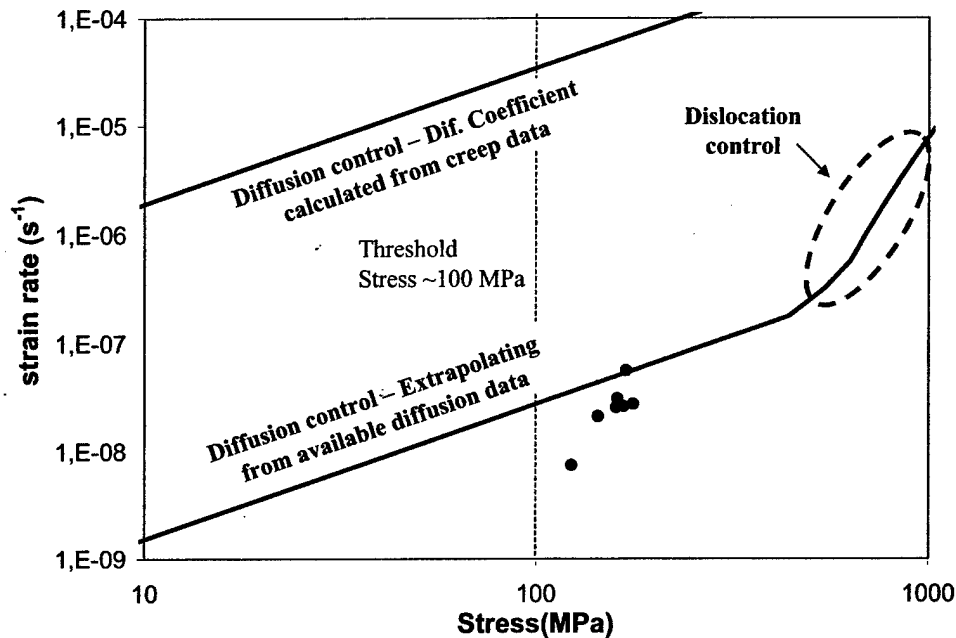


Fig. 15. Plot of the experimental (solid circles) and calculated creep rates at 1500° C considering diffusional creep (using diffusion coefficients obtained from creep on polycrystals and extrapolating the diffusion data available), and dislocation controlled creep. The regions where diffusional and dislocation plasticity dominate are indicated. Diffusion kinetics can explain the experimental creep rates. Dislocation plasticity dominates only at stresses well over the fracture stresses of this system.

nection leads to longer diffusion paths than the ones measured from the two dimensional cross-sections.

The microstructural evolution observed during the tests at temperatures over 1500° C is strong evidence supporting the importance of diffusion at the testing temperatures. The observed coarsening and longitudinal decrease of aspect ratio is driven by the decrease in interfacial energy. However, this coarsening indicates that the strains of the creep experiments could be easily caused by diffusion. Due to this microstructural evolution, detailed study of the creep curves was restricted to temperatures below 1500° C.

The high stress exponent observed could be explained by the existence of a threshold stress and by the non-stationary nature of creep within this system as will be discussed in Section 4.3. The activation energy for creep is compatible with the activation energies of diffusion available for the different species in alumina and garnet that range from 300 to 700 kJ mol⁻¹ [25, 27].

Based on these observations, diffusion is a plausible explanation for the quasi-steady-state creep rates observed. It is consistent with the magnitude of creep, the calculated creep parameters, the microstructural observations, and the loading and unloading transients.

4.2.2. (b) Dislocation mechanisms

The stress necessary to drive a dislocation across the interfaces is at least two orders of magnitude higher than the resolved stresses applied in the tests [14]. The dislocations must then move within one of the two components, thus they must bow within the phase spacing (λ). The stress necessary for this process is [28]:

$$\tau = \frac{Gb}{\lambda}, \quad (10)$$

where G is the shear modulus, and b the Burger's vector. We will consider that $\text{Er}_3\text{Al}_5\text{O}_{12}$ has similar properties to $\text{Y}_3\text{Al}_5\text{O}_{12}$ (elastic shear modulus at 1500° C of 110 GPa, and Burgers vector $\langle 111 \rangle = 1.04$ nm) [17]. For Al_2O_3 , a Burger's vector

of 0.512 nm and an elastic shear modulus at 1500°C of 133 GPa were used [17]. The nominal phase spacing ranges from 0.1 to 1 μm . The stresses necessary to bow the dislocations through the smallest spacing are then 1 GPa for $\text{Er}_3\text{Al}_5\text{O}_{12}$ and 0.7 GPa for Al_2O_3 . This calculation suggests that dislocation glide in $\text{Er}_3\text{Al}_5\text{O}_{12}$ is seriously limited as the stress necessary for dislocation bowing within the phase spacing s is of the same order of magnitude as the applied stress. The stress calculated from equation (10) would be the threshold stress for dislocation-controlled plasticity.

The behavior expected under the assumption that dislocation mechanisms are active can be calculated using literature data on sapphire and YAG [17] single crystals. Sapphire creep data is available for c-axis and 42° off axis orientations [6]. The TEM observations showed that the c-axis of alumina is not perfectly parallel to the specimen axis; a linear interpolation was taken between these two sets of data assuming a misalignment of 10°. In the case of garnet, creep data for [110] compression [17] was used. The isostrain condition was imposed and threshold stresses were calculated from equation (10). The phase spacing of alumina and garnet was taken as 0.31 and 0.46 μm , respectively.

The calculated strain rates for dislocation plasticity are lower than the experimental ones. Figure 15 shows that dislocation plasticity would dominate only at stresses well over the fracture stresses for this system. The extensive TEM studies did not find significant dislocation densities. The isolated dislocations found (Fig. 11), are very different from the typical dislocation networks of crept single crystals. This experimental evidence supports the conclusion that dislocations do not play a significant role in deformation. The low density of dislocations also has been acknowledged in other works in similar systems [8, 29]. Even in systems with a larger phase spacing (approximately between 5 to 20 μm) very little dislocation activity is reported in constant strain rate tensile experiments [30]. The increase in phase spacing will increase the diffusion paths and decrease the stress necessary to bow dislocations.

4.3. Steady state creep or primary creep?

From the arguments put forth in the discussion above, un-accommodated diffusion appears to be the mechanism responsible for creep deformation under the experimental conditions. This mechanism will not yield a true steady state creep behavior because the strain caused by diffusion is not accommodated. Due to the strong bonding of these interfaces, boundary sliding does not occur. The $\text{Al}_2\text{O}_3/\text{Er}_3\text{Al}_5\text{O}_{12}$ system is deforming in a primary regime until damage at the interphase interfaces is created. Steady state creep terminology should only be used then as a phenomenological approach to describe the best creep resistance under certain conditions and to compare with the creep resistance of other materials.

The time dependence of strain in primary creep is usually described by [16],

$$\epsilon = At^{1/m}. \quad (11)$$

Figures 4 and 5 show creep curves for two external stresses together with their best fits using equation (11). The curves fit well with the time dependence of equation (11). The exponent m obtained ranges between 3 to 8. However, if we consider only the final part of the creep curve in Fig. 4 (low strain rates, small stress), a straight line can also give a reasonably good fit. It is then difficult to determine from the final portion of the curve, which fit is better as the strain to failure is small. For example, if the $\text{Al}_2\text{O}_3/\text{Er}_3\text{Al}_5\text{O}_{12}$ system is deforming at $1.1 \times 10^{-8} \text{ s}^{-1}$ after 50 h and fails after 60 h, in these last 10 h, assuming a primary creep behavior with $m=5$, the strain rate would decrease to $1.06 \times 10^{-8} \text{ s}^{-1}$. This decrease in strain rate would be difficult to measure. The continuous decrease in strain rate is better observed in high strain rate experiments (Fig. 5), supporting the idea that the system remains in the primary creep region. Previous work on alumina-YAG also acknowledges this lack of steady-state creep [8]. These authors report a continuous decrease of strain rate down to a minimum, and then an increase of strain rate to failure. The minimum creep rate during the tests is taken as the steady state creep [8].

The determination of the stress dependence of

the quasi-steady state creep rate must be carefully considered. The strain to initiate damage at the interfaces that will lead to failure depends more strongly on the degree of interlocking of the microstructure than on the applied load. A more interpenetrating microstructure requires greater sliding at the interfaces to accommodate diffusion. The applied load controls how fast the system reaches this critical strain for damage, so the time to failure will be shorter as we increase the load. If we fit the final portion of the curve with a straight line for two stresses, we will get an apparent stress exponent higher than the real stress dependence of the transient regime. The relation between these exponents can be calculated. The strain rate follows the equation:

$$\dot{\epsilon} = \frac{A}{m} \sigma^n t^{(1/m)-1}. \quad (12)$$

The strain to failure gives a relation between the times to failure at the two loads

$$\epsilon_{\text{damage}} = \epsilon_1 = \epsilon_2 \Rightarrow \left(\frac{\sigma_1}{\sigma_2} \right)^n = \left(\frac{t_2}{t_1} \right)^{1/m}. \quad (13)$$

The stress exponent from the linear fits prior to failure is:

$$\begin{aligned} n_{\text{apparent}} &= \frac{\log\left(\frac{\dot{\epsilon}_1}{\dot{\epsilon}_2}\right)}{\log\left(\frac{\sigma_1}{\sigma_2}\right)} \\ &= \frac{\log\left(\left(\frac{\sigma_1}{\sigma_2}\right)^n \left(\frac{t_1}{t_2}\right)^{(1/m)-1}\right)}{\log\left(\frac{\sigma_1}{\sigma_2}\right)}. \end{aligned} \quad (14)$$

Using equation (13):

$$n_{\text{apparent}} = mn. \quad (15)$$

A value of $m=5$ will give a stress exponent 5 times the real stress dependence of the microscopic deformation mechanism. The measured stress exponent from the strain rate prior to failure could only be equal to the real stress dependence if the times to failure are the same. This is not the case as the time to failure is much shorter for higher loads.

The experimental situation (Fig. 4) is far from ideal. The time exponent and pre-power constant of strain show considerable scatter. This is not surprising given the complexity of the microstructure. However, the main issues are clear: the evolution of strain with time follows a power law typical of transient creep, and the stress exponent determined from the strain rate prior to failure leads to an overestimation of strain values. In Figs 4 and 5 the values of the stress exponent comparing strain rates prior to failure ($n=7.3$) and comparing strain rates at the same time ($n=2.6$) are calculated.

The transient nature of creep in this system together with the existence of a threshold stress accounts for the high stress exponent measured (reported as high as 18 in the literature [8, 29]). These experimental values are so far from the values expected from the diffusion or dislocation models that they do not by themselves provide sufficient support for either. Additional evidence is needed.

5. Conclusions

The $\text{Al}_2\text{O}_3/\text{Er}_3\text{Al}_5\text{O}_{12}$ (19.5 mol% Er_2O_3) system grown by directional solidification produces a fine microstructure with a high density of well-bonded interfaces. This microstructure imposes an isostrain condition during elastic and plastic deformation. The different elastic and plastic properties of the two phases leads to a unique load transfer situation.

There is load transfer to the garnet phase while this phase is deforming elastically that causes a continuous decrease of creep rate. During this transient regime the garnet phase deforms elastically and alumina deforms plastically. Following the initial region, both phases will be deforming at the same rate which is the global deformation rate of the $\text{Al}_2\text{O}_3/\text{Er}_3\text{Al}_5\text{O}_{12}$ eutectic. The lack of dislocations within the deformed specimens, the coarsening of the microstructure, the activation energies for creep, and the detailed study of the transient creep during loading and unloading conditions, leads to the conclusion that creep deformation of $\text{Al}_2\text{O}_3/\text{Er}_3\text{Al}_5\text{O}_{12}$ eutectic is diffusion controlled. Sliding at the interfaces does not accommodate diffusion and the system deforms in a non-steady-

state regime. Non-steady-state deformation leads to over-estimation of the stress exponents. Damage induced by the stress built up at the interfaces initiates final failure.

The unloading of the $\text{Al}_2\text{O}_3/\text{Er}_3\text{Al}_5\text{O}_{12}$ system following a moderate amount of creep deformation, produces a unique strain recovery. The driving force for the stress recovery is the stress that builds up due to the elastic deformation of garnet phase while alumina phase is deforming plastically.

Acknowledgements

The authors would like to thank Dr G. Morscher for the discussions on recovery creep and transients, Dr J. Goldsby for his help setting up the creep rigs, and Mr Tom Sabo for the technical assistance on the monofilament fabrication. This research was funded by NASA cooperative agreement NCC3-850 and AFOSR Grant #F49620-00-1-0048. MCyT MAT2000-1533-C03-03 funded the research in Spain.

References

- [1] Sayir A, Matson LE. HITEMP, NASA CP-10082, 1991, 1:83.
- [2] Sayir A, Dickerson RM, Yun HM, Heidger S, Matson LE. HITEMP, NASA CP-10146, 1994, 1:74.
- [3] Farmer SC, Sayir A, Dickerson PO. *Mat Res Soc Proc* 1995;365:11.
- [4] Sayir A. Directional solidification of eutectic ceramics. In: Pechenik A, Kalia RK, Vashista P, editors. *Computer aided design of high-temperature materials*. Oxford University Press; 1999. p. 10-7.
- [5] Sayir A, Farmer SC. *Acta Mater* 2000;48:4691.
- [6] Sayir A, Farmer SC. *Mat Res Soc Proc* 1995;365:22.
- [7] Sayir A, Hurst JB, and Jones S. HITEMP, NASA CP-10039, 1989.
- [8] Matson LE, Hecht N. *J Europ Ceram Soc* 1999;19:2487.
- [9] Parthasarathy TA, Mah TH, Matson LE. *J Am Ceram Soc* 1993;76(1):29.
- [10] Pastor JY, Poza P, Llorca J, Ipeña JJ, Merino RI, Orera VM. *Mat Sci Engine A241* 2001;308(1-2):241.
- [11] Pitchford JE, Deleglise F, Berger MH, Bunsel AR, Clegg WJ. *Ceram Eng Sci Proc* 2001;22(3):415.
- [12] Farmer SC, Sayir A. *Engng Fract Mech* 2002;69:1015.
- [13] Sayir A, Farmer SC. Fracture characteristic of single crystal and eutectic fibers. In: Elices M, Llorca J, editors. *Fiber fracture*. Elsevier Science; 2002. p. 10-9.
- [14] Martínez Fernández J, Sayir A. *Ceram Eng Sci Proc* 2001;22(3):421.
- [15] Wu P, Pelton AD. *J of Alloys and Compounds* 1992;179:259.
- [16] Poirier J. *Creep of crystals*. Cambridge University Press, 1985.
- [17] Cormann GS. *Ceram Eng Sci Proc* 1991;12(9-10):1745.
- [18] Garboraud RJ. *Phil Mag, A* 1981;44(3):561.
- [19] Clauser AH, Wilcox BA. *J Am Ceram Soc* 1976;59(3-4):89.
- [20] Gómez García D, Martínez Fernández J, Domínguez Rodríguez A, Castaing J. *J Am Ceram Soc* 1997;80:1668.
- [21] Morscher GN, Farmer S, Sayir A. *Ceram Eng Sci Proc* 1995;16(5):959.
- [22] Nye JF. *Physical properties of crystals*. Oxford Science Publications, 1985.
- [23] Heuer AH, Cannon RM, Tighe NJ. Plastic deformation in fine grain ceramics. In: Burke JJ, Reed NL, Weiss V, editors. *Ultra-fine grain ceramics*. Syracuse University Press; 1970. p. 33-9.
- [24] Nix WD. *Metals Forum* 1981;4(1-2):38.
- [25] Sakaguchi I, Haneda H, Tanaka J. *J Am Ceram Soc* 1996;79(6):1627.
- [26] Parthasarathy TA, Mah TH, Keller K. *J Am Ceram Soc* 1992;75(7):1756.
- [27] Cawley JD, Halloran JW, Cooper AR. *J Am Ceram Soc* 1991;74(9):2086.
- [28] Hirth JP, Lothe J. *Theory of dislocations*. John Wiley and Sons, 1982.
- [29] Deleglise F. Ph.D. Thesis. Centre des Matériaux, Ecole des Mines de Paris, France, 2000.
- [30] Waku Y, Sakuma T. *J Europ Ceram Soc* 2000;20(10):1453.

CREEP RESISTANCE OF THE DIRECTIONALLY SOLIDIFIED CERAMIC EUTECTIC OF $\text{Al}_2\text{O}_3/\text{c-ZrO}_2$: EXPERIMENTS AND MODELS

J. Yi^a, A. S. Argon^{a,*}, A. Sayir^b

^a*Massachusetts Institute of Technology, Cambridge, MA 02139*

^b*NASA-Glenn Research Center, Cleveland OH, 44135*

Abstract

The creep resistance of the directionally solidified ceramic eutectic of $\text{Al}_2\text{O}_3/\text{c-ZrO}_2(\text{Y}_2\text{O}_3)$ was studied in the temperature range of 1200-1520°C both experimentally and by mechanistic dislocation models. The topologically continuous majority component, Al_2O_3 , has a nearly perfect growth texture in the [0001] direction and encapsulates the minority $\text{c-ZrO}_2(\text{Y}_2\text{O}_3)$ component in a variety of morphologies. This encapsulated minority component too has a close to $\langle 112 \rangle$ growth texture, regardless of morphology. The two components are separated by close to coherent and well structured interfaces.

The creep of the eutectic in its growth direction exhibits an initial transient that is attributed to stress relaxation in the c-ZrO_2 component, but otherwise in steady state shows many of the same characteristics of creep in sapphire single crystals with c -axis orientation. The creep strain rate of the eutectic has stress exponents in the range of 4.5-5.0 and a temperature dependence suggesting a rate mechanism

governed by oxygen ion diffusion in the Al_2O_3 . While required TEM evidence is still incomplete, finite element analysis of stress distribution in the two components and a detailed dislocation model of the creep rate indicate that much of the nano-scale encapsulated c-ZrO₂ is too small to deform by creep so that the major contribution to the recorded creep strain is derived from the diffusion-controlled climb of pyramidal edge dislocations in the Al_2O_3 component. The evidence suggests that the climbing dislocations in Al_2O_3 must repeatedly circumvent the c-ZrO₂ domains acting as dispersoids resulting in the stress exponents larger than 3. The creep model is in very good agreement with the experiments.

Key words: directionally solidified ceramic eutectic; creep resistance; $\text{Al}_2\text{O}_3/\text{c-ZrO}_2$ eutectics.

1 Introduction

As Fleischer [1] noted, to reach beyond the capabilities of the present set of high temperature superalloys and some intermetallic compounds that have service limitations at around 1000°C, it is necessary to consider other compounds such as oxides, carbides, borides, etc. to reach service temperatures in the 1400-1600°C range. While these are all intrinsically brittle materials, having low temperature brittleness problems, their high temperature performance is largely governed by their creep resistance and fracture resistance. It is creep resistance that is of principal concern here to us.

For some time single crystal sapphire fiber with [0001] axis orientation has been considered as an ideal material for high temperature application [2]. In

* corresponding authors: argon@mit.edu

that orientation with its principal basal and prismatic systems unstressed, sapphire single crystal fibers have remarkable creep resistance in the 1400-1600 °C temperature range where only the pyramidal slip system is stressed. Early experiments of Firestone and Heuer [3] on [0001] axis-oriented-sapphire in the 1600-1800°C range produced evidence that such sapphire crystals creep entirely by the climb of the $1/3\langle 1\bar{1}01 \rangle$ pyramidal edge dislocations, with no slip line or stereo-TEM evidence of glide of such dislocations on any of the possible pyramidal planes available. That such dislocations are entirely sessile has now been established in very recent MD simulations of the core structures of these dislocations [4,5]. The stress dependence of the creep rates of [0001] oriented sapphire crystals and their governing activation energy of oxygen ion diffusion in Al_2O_3 have all been consistent with a pure climb mode of creep [3]. This is extremely rare in the creep of metals, with the only similar occurrence having been reported by Edelin and Pourier [6] in similarly oriented Mg crystals.

While oriented sapphire single crystal fibers have advantageous characteristics and have been considered with diffusion barrier coatings as reinforcing elements in polycrystalline Al_2O_3 matrixes for composite applications [7,8], the practice has been costly and lacked flexibility. As an alternative to sapphire-fiber-reinforced ceramic composites, a series of directionally solidified ceramic eutectics, consisting largely of an Al_2O_3 component together with compatible stable oxides of ZrO_2 or YAG combine many of the advantages of sapphire fiber with morphological stability at elevated temperatures and relative ease of production. Of these the Al_2O_3 , ZrO_2 system eutectic, with additional 4.2 mol% Y_2O_3 modification to create cubic ZrO_2 , has received considerable attention [9]. This eutectic has demonstrated some attractive characteristics.

In the Laser Heated Float Zone (LHFZ)-produced eutectic in the form of fibers or slender rods the $\text{Al}_2\text{O}_3/\text{c-ZrO}_2$ eutectics possess a sub-micron scale morphology in which the majority Al_2O_3 component maintains a topologically continuous form with a remarkably tight [0001] growth texture [10,11]. The c- ZrO_2 component, in turn, in various morphological shapes ranging from aligned fibers or platelets in either well organized colonies or in less well ordered forms, usually has one narrow dimension in the $0.2\mu\text{m}$ range, and is always fully encapsulated in the Al_2O_3 component. This eutectic has fairly reproducible and reasonably attractive levels of fracture toughness [12] and possesses high quality nearly coherent interfaces [13].

The eutectics contain significant levels of residual stress at room temperature, resulting from thermal misfit between the components. The Al_2O_3 was found to be in a state uniaxial tension parallel to the axis, at a level of 1.0 GPa while the c- ZrO_2 was in some form of multiaxial compression, roughly at the same level [10]. Such residual stresses that decrease in level at elevated temperatures could still be of importance in initial creep response [14] where they, however, should be rapidly relaxed on the onset of steady creep flow.

Here we will be primarily interested in the creep resistance of these $\text{Al}_2\text{O}_3/\text{c-ZrO}_2$ eutectics in the 1200-1520°C range.

2 Experimental Details

2.1 *Material and characterization*

The eutectics of $\text{Al}_2\text{O}_3/\text{c-ZrO}_2(\text{Y}_2\text{O}_3)$ have all been produced by the Laser Heated Float Zone (LHFZ) method at the NASA Glenn Research Center in the laboratory of Sayir. They had cross-sectional dimensions roughly in the range of 1-1.5 mm diameter but showed thickness variations along their 20-22 cm length. They were composed of 67% Al_2O_3 and 33% c-ZrO_2 by volume. Random sectioning of the rods always showed a certain residual component of Y_2O_3 and some YAG at levels that were considered to be insignificant. More significant however was an unavoidable level of porosity along the center line of many samples, often with substantial pore dimensions to constitute supercritical flaws for fracture. These pores always had smooth surfaces indicating they resulted from inadequate wetting during melting and solidification of the initial charge. In a few instances they resulted in fracture during loading of the creep experiments where they were given no further attention other than characterization of the pore sizes and shapes as a feed-back to improve the production process. TEM specimens made from randomly spaced axial and transverse sections were used for electron diffraction to check orientation of components. These, as well as a limited number of X-ray pole figure determinations obtained from surfaces of axial and transverse section of the bars demonstrated that the Al_2O_3 component had a growth texture of $[0001]$ within $2\text{-}3^\circ$ parallel to the bar axis. Wherever prominent three-fold symmetrical colony structures of c-ZrO_2 were observable on transverse sections, there were notable angular differences between the symmetry axes of these colonies

indicating the presence of small angle tilt boundaries in the Al_2O_3 , (often in the range of 10°) with tilt axes parallel to the growth axis. Since such tilt boundaries would not be stressed in samples under tension parallel to the bar axis, they were not considered to be of any importance in the creep behavior.

A few direct lattice imaging observations were also made of the structure of interfaces. Figure 1 shows one such DL image of a typical interface that is incoherent but atomically narrow.

Corresponding determination of the texture of the c- ZrO_2 component, largely based on electron diffraction information, indicated that this component had primarily a $\langle 112 \rangle$ growth texture with fiber symmetry, incorporating random rotations about this axis*. The sketch of Fig. 2 shows pictorially the mutual orientational association of the two components.

2.2 Creep equipment and creep strain measurement

The creep experiments were carried out in tension inside a Centorr vacuum chamber containing a specially designed hot zone of 5cm diameter and 5cm length made up of a split cylindrical configuration of a 1mm thick *Ta* sheet with alternating up-and-down slits to increase the path length of the heating element. The hot zone was surrounded by a series of *Mo* radiation shields. The long specimens threaded through the hot zone and were gripped at their ends by specially produced metallic friction grips, clamping down on the ends of the specimens through annealed soft nickel sheets to avoid local high pinching forces on the rods that could have resulted in fracture. Two relatively massive

* Textures such as $\langle 111 \rangle$ have also been reported by other investigators.

water cooled OFHC *Cu* plates were placed between the two exits of the hot zone and the specimen grips to assure that the gripping conditions were, as much as possible, at low temperature not to exceed about 200°C to avoid slippage in the grips.

An optical grade sapphire window permitted viewing the hot specimen through a narrow axial slit in the heating elements to permit direct measurements of the specimen temperature by means of a two-wave-length pyrometer (from Omega Vanzetti, Sharon, MA.), providing emissivity-independent measurements. In addition to a control thermocouple inside the hot zone, another thermocouple placed close to the specimen without touching it, was used to actually record the steady temperature in the thermal cavity. The temperature measured by this second thermocouple and that measured by the pyrometer on the specimen usually agreed quite well. The hot zone temperature was automatically controlled by the PID control system of the Centorr equipment.

Since the steady state creep extensions of the specimens under stress were generally quite small, to eliminate random flexures and motions of the massive creep frame from influencing the measurements, the displacements of the two ends of the load train immediately outside the vacuum chamber were simultaneously measured by sets of four LVDTs at both the top and bottom ends of the Centorr chamber. The differences between these two measurements then corresponded to the extension of the specimen. Since the temperature of the specimen inside the hot zone was higher by 1200-1300°C above the portions of the sample outside the hot zone, the gauge length was taken as the axial extent of the hot zone. Even under ideal conditions the total creep strain was never too uniquely determinable. To overcome this difficulty all creep strains at steady state were always measured incrementally at a given temperature

under two different applied stresses and often as loading and unloading cycles. This practice of relative measurements of creep strain did not only give more reliable determinations of the strain rates at the two different levels of stress but also demonstrated the nearly complete absence of transients in such incremental changes in steady state creep. A typical response of this type is shown in Fig. 3 for creep at 1520°C at stress levels of 150MPa and 200MPa. The random-appearing irregularities on the creep curves in Fig. 3 were attributed to be of instrumental origin. When determining actual increments of creep strain in any interval of time these variations were operationally smoothed out. The accuracy of strain measurement was around 1.4×10^{-5} .

3 Experimental Results

3.1 Transient effects

Upon initial application of stress to a virgin specimen a strain transient was always observed. One such transient recorded for an experiment at 1200°C under a stress of 300 MPa is shown in Fig. 4. The characteristic time constant of the transient decreased with increasing temperature, e.g. from c.a. 3.4×10^3 sec at 1200°C to 200 sec at 1400°C. The usual explanation of the transient to be due to initial work hardening in the creeping components prior to establishment of a steady state by recovery processes, familiar in creep of homogeneous metals, was discounted here since no prominent transients were found following stress increases at steady state creep. The most likely cause of the transient was the rapid stress relaxation in the coarse c-ZrO₂ component by creep since for the measured texture of that component there is an abun-

dance of the $\langle 110 \rangle \{100\}$ principal slip systems that are well oriented for slip, and the creep resistance of c-ZrO₂ in this temperature range is known to be poor [15]. An upper bound estimate of this effect could be assessed from a FEM study that will be presented in Section 4.3 where it was found that for the complete relaxation of the deviatoric stresses in the entire c-ZrO₂ component the volume average deviatoric stresses as well as mean normal stresses in the Al₂O₃ component, increase roughly by 25-30% which would result in an increment of additional elastic strain in the sample of about 6×10^{-4} . This level is illustrated in Fig. 4 by the horizontal line. The actual amount of stress relaxation in the c-ZrO₂, however, is difficult to determine since a substantial fraction of this component has phase dimensions in the range of 0.2-0.4 μm and is likely to be dislocation-free and incapable of plastically deforming as we discuss in Section 4.0. These, and the difficulties in determining the absolute measures of strain derived from the hot zone portions of the samples requires us to de-emphasize this portion of the creep response.

3.2 *Steady state creep*

As already mentioned in Section 2.2 the main information on steady state creep was obtained from incremental experiments of sudden stress increases and decreases at constant temperature as shown in the typical case of Fig. 3 of creep response. A simple check of the magnitude of the instantaneous stretches or contractions for stress increases or decreases, utilizing the appropriate information on the temperature dependent Young's modulus of Al₂O₃ [16] gave in all cases that the recorded jumps were all about a factor of 2 larger than what could be expected from the sample in the hot zone. Since

this was well within the additional flexures and relaxations in the load train the recorded strain rates were considered to be reliable.

After the final configuration of the hot zone discussed in Section 2.2 was completed, 11 determinations of steady state creep rate were made, all together at 3 temperatures of 1200, 1400, 1520°C at stress levels ranging from 150MPa to 275MPa, derived from incremental experiments similar to those in Fig. 3. These measurements are listed in Table 1 and are plotted in Fig. 5 together with the creep rates at 1400°C due to Sayir, quoted in [17]. The stress exponents of the creep rates at 1400°C and 1520°C, shown in Fig. 5, are 4.16 and 5.38 and are lower than that of Sayir at 6.00. As we will discuss in the creep model in Section 4.3, these exponents are relatively high and need to be explained, as will be done later in Section 4.4.

Table 1 contains also sufficient information for the determination of the activation energy of the governing creep process. The plot of the creep rates at a stress of 200MPa for three temperatures of 1200°C, 1400°C and 1520°C in Fig. 6 gives an activation energy of $Q = 71.1$ kcal/mol for the rate controlling process in steady state creep which we consider to be due to oxygen ion diffusion in Al_2O_3 . This value is to be compared with 105 kcal/mol for temperatures above 1400°C and 26 kcal/mol for temperatures below 1400°C for the same process measured by Oishi and Kingery [25] in pure polycrystalline Al_2O_3 .

4 The Creep Model

4.1 Basic assumptions

The fact that the $c\text{-ZrO}_2$ component of considerably lower creep resistance is encapsulated everywhere by the topologically continuous Al_2O_3 component with a very tight growth texture of $[0001]$ along the axes of the DS eutectic rods indicates that steady state creep must be controlled by the Al_2O_3 component, once any limited compliance increment due to the stress relaxation in $c\text{-ZrO}_2$ is complete. This suggests that the overall creep response must have the same characteristics of steady state creep in sapphire single crystals reported by Firestone and Heuer [3], albeit with certain added complexities derived from the presence of the $c\text{-ZrO}_2$ component. Figure 7 shows the well known phase morphology of a typical $\text{Al}_2\text{O}_3/c\text{-ZrO}_2$ eutectic where the white component is the $c\text{-ZrO}_2$. Very much like the γ' component in superalloy single crystals of CMSX-3 [18], a large fraction of the $c\text{-ZrO}_2$ component has dimensions in the range of $0.2\text{-}0.4\text{ }\mu\text{m}$ and would be too small to have the capability of undergoing plastic flow by independent internal processes of dislocation multiplication by glide or climb, as already remarked above. The $c\text{-ZrO}_2$ components of larger dimensions, as the irregular shaped ones in Fig. 7 should undergo rapid stress relaxation in the $1200\text{-}1520^\circ\text{C}$ temperature range of interest, as the transient creep curve of Fig. 4 suggests. Even so, as we present in Section 4.3, FEM analysis shows that complete shear stress relaxation in the $c\text{-ZrO}_2$ component still leaves the mean normal stress intact which prevents large average stress enhancement in the Al_2O_3 component.

Since the best slip systems of the basal and prismatic type are largely un-

stressed for glide due to the tight texture of the Al_2O_3 component, and since the pyramidal dislocations of $1/3 < \bar{1}101 >$ type are sessile, due to a unique core restructuring process as has been recently demonstrated [4,5], we expect that creep in this component for eutectic fibers in tension, can only be a consequence of climb of the $(1/3) < \bar{1}101 >$ dislocations, whether they exist on the prism planes or the pyramidal planes. This has already been recognized by Firestone and Heuer [3]. Creep derived entirely from climbing of edge dislocations is quite rare in structural metals. The only previously reported similar case is in Mg single crystals stressed in the $[0001]$ direction [6]. Nabarro [19] has presented an idealized model of creep derived from climb of dislocation of a Frank type network where material fluxes are between the actual climbing dislocations with Burgers vectors parallel to the stress axis and those of other types experiencing no climb forces. Firestone and Heuer [3] found reasonable agreement of their results where the stress exponents were in the range of 3 as the Nabarro model predicts. In our case where the stress exponents are in the range of 4.5-6.0 we expect different conditions to hold, requiring considerable modification of the Nabarro framework.

Since basic TEM information is still largely absent to furnish better guidance, in our model we make a number of essential assumptions. We assume that the $(1/3) < \bar{1}101 >$ dislocations pre-exist in the Al_2O_3 component, having been generated during the directional solidification process while the morphology is established, and will multiply by topological convolution processes during this phase in well known ways from sources, and will be available for climb under stress during creep. We expect that the mean free path lengths of climbing dislocations in Al_2O_3 will involve several multiples of the interphase dimensions, i.e. be of the order of microns, requiring the climbing dislocations to repeat-

edly bow and straighten-out as they thread through the small $c\text{-ZrO}_2$ domains that will remain impenetrable to them. Such repetition of transient line shapes will be viewed as the primary source of the creep stress exponents to be larger than 3 [20]. We assume that the climbing pyramidal dislocations can multiply by topological process a'la Bardeen and Herring [21]. As for the climb of these dislocations, we assume that this will be diffusion controlled with adequate jog concentrations present along the dislocations, these we expect to be produced by nodal emission processes from network junctions rather than being of a thermal equilibrium nature which preliminary analyses show to be far too difficult. We assume that the diffusional transport will be between dislocation cores and the large concentrations of incoherent or semi-coherent interfaces. We assume also that the interfaces will be completely opaque to the transmission of dislocations from $c\text{-ZrO}_2$ to Al_2O_3 or vice versa. Analysis indicates that such transition would be subject to extremely large energy barriers, that can not be overcome. We expect that the residual stresses due to initial thermal misfit between the components will be relieved during the transient phases of the creep and provide another contribution to the recorded amounts shown in Fig. 4, but that steady state creep will be governed by the climb forces resulting entirely from the applied stress.

Finally, we expect that as the topologically continuous framework of the Al_2O_3 component creeps and extends while the $c\text{-ZrO}_2$ component largely remains either dormant or is merely stress-relaxed, global back stresses will develop in the Al_2O_3 , gradually slowing down the creep rate [22]. Since the creep ductilities of the eutectics are quite modest, we do not expect this back stress to develop fast enough to be of consequence, and ignore it.

4.2 The creep rate

Consider a round tensile creep bar of an $\text{Al}_2\text{O}_3/\text{c-ZrO}_2$ eutectic as sketched in Fig. 8 where local axes 1,2,3, are chosen in a pyramidal glide system with axis 1 chosen parallel to the $1/3 \langle \bar{1}101 \rangle$ Burgers vector, axis 2 normal to the pyramidal plane making an angle φ with the bar axis, and axis 3 parallel to the line vector of a positive edge dislocation. Under a uniform stress σ_1 a positive edge dislocation will climb in the negative 2 direction with a velocity v_c to contribute to a uniaxial tensile creep strain rate parallel to the 1 direction. This velocity, if it were governed by diffusion controlled climb would be given by [23]:

$$v_c = \frac{2\pi D(\sigma_1 - \sigma_T)b^2}{kT \ln(r_s/r_c)} \quad (1)$$

where $D = D_0 \exp(-Q/RT)$ is the inter-diffusion constant of O ions in Al_2O_3 which is recognized to be the slow diffusing species, σ_T is the triaxial component of the applied stress ($= \sigma_z/3$) that does not promote equilibrium climb, r_s is the distance from the dislocation core to vacancy sinks along the interfaces, r_c the core radius from which point defect emission is considered, b the magnitude of the Burgers vector, D_0 the pre-exponential factor of the diffusion constant, Q the activation energy of O ion diffusion in Al_2O_3 and R and T have their usual meaning. The kinematics of shape change due to climb alone of dislocations has been considered more broadly by Groves and Kelly [24]. In our case a more specialized consideration will be adequate. Thus, considering that there will be three equivalent pyramidal systems that can contribute to the axial strain rate equally, as is explained in the Appendix, the axial creep strain rate $\dot{\epsilon}_z$ along the bar and the accompanying radial contractile strain rates $\dot{\epsilon}_r$ are given respectively as:

$$\dot{\epsilon}_z = (2 - 3\cos^2\phi)\dot{\epsilon}_0 \quad (2a)$$

and

$$\dot{\epsilon}_r = -(1 - \frac{3}{2}\cos^2\phi)\dot{\epsilon}_0 \quad (2b)$$

where

$$\dot{\epsilon}_0 = b\rho_m v_c \quad (3)$$

is the main creep rate in the pyramidal system coordinates without regard to overall volume preservation, which is considered to result in eqns(2a) and (2b) (see Appendix I). Relating the actual climb-producing tensile stress σ_1 to the axial stress σ_z and considering the volume-average effect of the local variation of stress due to the presence of the c-ZrO₂ components by a factor q we have

$$\sigma_1 - \sigma_T = \frac{2}{3}q\sigma_z(1 - \cos^2\phi) \quad (4)$$

If the mobile dislocation density, ρ_m , of climbing dislocations at steady state is governed by mutual interactions in a self adjusting basis [19]; i.e.

$$\rho_m \cong \left(\frac{2\pi\sigma_z}{\mu b}\right)^2 q^2 (1 - \cos^2\phi)^2 \quad (5)$$

we have, by finally combining eqns (2a),(3),(4) and (5) the axial steady state creep rate:

$$\dot{\epsilon}_z = A \left(\frac{D}{b^2}\right) \left(\frac{\sigma_z}{\mu}\right)^3 \left(\frac{\mu\Omega}{kT}\right) \frac{(1 - \cos^2\phi)^3 (2 - 3\cos^2\phi)}{\ln(r_s/r_c)} \quad (6)$$

where

$$A = \frac{2}{3}(2\pi)^3 \frac{q^3}{\beta} \quad (7a)$$

and

$$\beta = \Omega/b^3 = 0.079 \quad (7b)$$

where Ω is the ionic volume of O in the Al_2O_3 lattice and q is a factor which relates the local volume average climb stress to the axial stress σ_z as is determined from a FEM analysis of the stress distribution in the Al_2O_3 component under an applied tensile stress as discussed in Section 4.3 below.

Eqn. (6) gives the creep rate due to the climb of quasi-straight dislocations in a homogeneous stress field. As we discuss in Section 4.4 this is not the case in the $\text{Al}_2\text{O}_3/\text{c-ZrO}_2$ eutectics where the climbing dislocations need to thread through the non-deforming c-ZrO₂ components acting as dispersoids and are required to alternately bow around these components and be released to straighten out, acting effectively as if straight dislocations were moving through a strongly internal varying stress field which will increase the stress exponent in predictable ways and decrease the actual creep rate [20].

In Section 4.5 we will evaluate the creep model and compare it with the experimental results.

4.3 Distribution of stresses in the $\text{Al}_2\text{O}_3/\text{c-ZrO}_2$ eutectics

A very important way in which creep in the eutectics differs from creep in single crystal sapphire is that in the former the stresses are distributed in a complex manner. In addition to residual stresses arising from the different thermal expansions of the two components, the applied stresses result in complex internal local stress distributions due to different elastic properties of the Al_2O_3 and the c-ZrO₂ components. Thus, to develop some necessary understanding of this phenomenon on a broad basis, a linear-elastic FEM analysis was carried out in a 2-D plane strain setting of the eutectic in the ordered re-

gions of Fig. 7. Here the c-ZrO₂ domains in 2-D are taken as elliptical cylinders occupying a volume fraction of 0.33. The chosen representative computational volume is indicated in this figure. We have considered the c-ZrO₂ component to be always fully relaxed of all shear stresses which is accomplished operationally by choosing the Poisson's ratio as 0.4999999. All other chosen material constants are listed in Table 2. In the broader analysis we considered the aspect ratios of ellipsoidal rods, a/b of c-ZrO₂ as 1,3,4 and 5. Of these results we present here only the distributions for $a/b = 3.0$ as most representative. All analyses were limited to the elastic range. In this FEM framework we considered several process simulations: a) an applied tensile stress σ_z alone; b) cooling the morphology from a stress-free condition at 1875°C down to 1400°C to determine residual stresses and; c) cooling as in (b) plus an applied tensile stress of $\sigma_z = 300\text{MPa}$. Of these we discuss here only the case of the internal stress distribution under an applied stress $\sigma_z = 300\text{MPa}$ (Since behavior is linear-elastic, results for all other stress levels can be determined by re-scaling).

In Fig. 10a we show the distribution of the Mises deviatoric stresses for the case of $\sigma_z = 300\text{MPa}$ and $T=1400^\circ\text{C}$, in the Al₂O₃ region. As expected, the states of stress inside the ellipsoidal regions of the c-ZrO₂ are close to constant. Figure 10b gives the more important distribution of the climb stress σ_1 , parallel to the pyramidal dislocation Burgers vector at an angle of $\phi = 57.7^\circ$ as shown in Fig. 8. The volume area-average level of this important climb producing stress was found to be $\sigma_1 = 216.3\text{MPa}$ which gives the factor q to be 0.721. This value appears surprisingly low in view of the assumed complete relaxation of the deviatoric stresses in the c-ZrO₂, until it is recognized that the c-ZrO₂ still supports fully a mean normal stress which limits the stress enhancement in

the Al_2O_3 component.

4.4 *Effect of internal resistance variations*

As stated in Section 4.2 the creep response of the $\text{Al}_2\text{O}_3/\text{c-ZrO}_2$ eutectics differ significantly from the creep behavior in homogeneous sapphire single crystals studied by Firestone and Heuer [3]. First because of the non-uniform stress distribution in the morphology of Al_2O_3 and c-ZrO_2 discussed in Section 4.3 above but even more importantly by the large perturbations that the climbing dislocations encounter threading through the isolated and largely non-deforming c-ZrO_2 domains. Thus, consider the convolutions that a climbing dislocation has to go through as it threads through the gaps of the c-ZrO_2 domains as depicted in Fig. 11. First, the climbing dislocation must squeeze into the gaps between the domains as depicted in Fig. 11a to a critical configuration much like the Orowan bowing process for non-shearable dispersoids. The peak stress that is required for this configuration to be achieved is

$$\sigma = \sigma_i = \frac{2\epsilon}{b\Lambda} = \frac{\mu b}{\Lambda} \quad (8)$$

where ϵ is the dislocation line tension ($= \mu b^2/2$) and Λ is the inter-domain gap. Clearly, here the process is not one of glide but climb where σ is the climb stress. Once the critical configuration is reached and the climbing dislocation surrounds the impenetrable domain and pinches off as shown in Fig. 11b, the separated dislocation has acquired a definite cusp where this shape of the dislocation will undergo accelerated climb due to the advantageous line tension effects. We view these required contortions of the dislocations as if they were the same as positive and negative internal stresses σ_i , retarding and then accelerating climb, very much like the corresponding cases of favorable

and unfavorable internal stresses that a glide dislocation needs to go through between dispwesoids. Such problems were treated in great detail by many investigators, but particularly thoroughly by Li [20], which illustrated that a gliding dislocation (in our case a climbing dislocation) loses more time in the region of adverse internal stress than the time it gains in moving through regions of favorable internal stress. The effect is illustrated in Fig. 12 where 12a shows the sinusoidally varying internal stress σ_i and the prevailing climb stress σ . The most important consequence of such deceleration and acceleration of motion is an increase in the effective stress exponent m of the dislocation velocity, scaled by the ratio of σ_i/σ is shown in Fig. 12b. A secondary effect is a factor $C = \bar{v}/v$ that gives the decrease in the average dislocation velocity relative to the velocity in unhindered climb shown in Fig. 12c, also scaled with the ratio of σ_i/σ . To assess a measure of the effect we note from Fig. 7 that in much of the morphology the inter-domain distance Λ would appear to be between 0.3-1.0 μm . Taking the small dimension to determine the maximum level of this effect, together with $b = 5.12 \times 10^{-10}m$ and $\mu = E/2(1 + \nu) = 73GPa$ [16] at 1400°C we determine $\sigma_i = 125MPa$. This, for an applied stress $\sigma_z = 300MPa$, in the range of interest, that would give a volume average climb stress $\sigma = q\sigma_z(1 - \cos^2\phi)$ of 153MPa, and a ratio $\sigma_i/\sigma \approx 0.815$, Fig 12b indicates that the effective stress exponent of the stress in the velocity expression should increase to nearly $m = 3$ from unity as the maximum effect. Moreover, Fig. 12c gives $C = \bar{v}/v = 0.6$. Clearly, larger distances Λ should result in smaller effective internal stresses while smaller applied stresses should give increased ratios σ_i/σ . The overall net effect will be rather complex to assess. Here, we consider that under the conditions described the net effect on the overall stress exponent of the creep rate will be to elevate it from $n = 3$ for the model presented above to $n = (2.5 + 2) = 4.5$ to $n = (3 + 2) = 5$.

This consideration and the factor C, when incorporated into the creep model of smooth climb given by Eqn (6) will change it finally to

$$\dot{\epsilon} = AC\left(\frac{D}{b^2}\right)\left(\frac{\sigma_z}{\mu}\right)^n\left(\frac{\mu\Omega}{kT}\right)\frac{(1 - \cos^2\phi)^3(2 - 3\cos^2\phi)}{\ln(r_s/r_c)} \quad (9)$$

It is this expression that we will compare with the experimental results in Section 4.5 below.

4.5 Evaluation of the creep model

We now proceed to evaluate our final creep model of Eqn(9) and compare it with experimental results. In the comparison we will evaluate the expression for both 1400°C and 1520°C. We use the following model parameters and material properties.

$$\mu = \frac{E}{2(1+\nu)} = 73\text{GPa at } 1400^\circ\text{C and } 63.4\text{GPa at } 1520^\circ\text{C [16]}$$

$$b = 5.12 \times 10^{-10}\text{m}$$

$$\Omega = 1.06 \times 10^{-29}\text{m}^3 \quad q = 0.721 \text{ as determined in Section 4.3}$$

$$\beta = \Omega/b^3 = 0.079$$

$$A = \frac{2}{3}(2\pi)^3(q^3/\beta) = 7.85 \times 10^2$$

$$\phi = 57.35^\circ$$

$$r_s = 0.5 - 2.0\mu\text{m, as estimated from micrographs (Fig. 7)}$$

$$r_c \approx b$$

$$D = 10^{-14}\text{cm}^2/\text{sec at } 1400^\circ\text{C and } 9 \times 10^{-14}\text{cm}^2/\text{sec at } 1520^\circ\text{C determined from Oishi and Kingery directly for their polycrystalline material [25] for which, parenthetically the activation energy was } Q=110\text{kcal/mol, considerably larger than our value.}$$

finally we take $n=4.5$ as suggested from our analysis in Section 4.4 above, and

$$C = 0.6$$

The calculated steady state creep relations for 1400°C and 1520°C are presented in Fig. 5 as the broken lines in comparison with the experimental data.

Considering the several uncertainties in the model and material parameters the agreement between model and experimental results is pleasing.

5 Discussion

The experimental measurements of steady state creep rates in the $\text{Al}_2\text{O}_3/\text{c-ZrO}_2$ eutectic, while few, have given a good measure of the response of this material in the temperature range of interest. Taking account of the possible interactions of the c-ZrO₂ component with the Al_2O_3 component we have developed a steady state creep model based on climb of pyramidal edge dislocations in Al_2O_3 alone. In our model we propose that the c-ZrO₂ component of relatively large size, in the micron range will most likely undergo nearly complete stress relaxation in the 1400°C range, resulting in an initial transient creep with relatively short time constant of roughly 200 seconds [2]. On the other hand the sub-micron size domains of the c-ZrO₂ will most likely be too small to undergo independent deformation processes by crystal plasticity and will remain non-deformable to impede the climb motion of the pyramidal system dislocations in the Al_2O_3 much like dispersoids. The observed creep rate stress exponents in the range of 4-5 are indicative of this behavior. In this sense it would appear that the eutectic through its unique morphology should be more creep resistant than sapphire of [0001] axis orientation. To explore this comparison we interpret our creep model for application to sapphire in

which the climb motion of the dislocations are expected to be quasi-smooth. Such a modification would give a steady state creep expression of

$$\dot{\epsilon}_{sap} = A' \left(\frac{D'}{b^2} \right) \left(\frac{\sigma_z}{\mu} \right)^3 \left(\frac{\mu \Omega}{kT} \right) \frac{(1 - \cos^2 \phi)^3 (2 - 3 \cos^2 \phi)}{\ln(r_s/r_c)} \quad (10)$$

where $A' = \frac{2}{3}(2\pi)^3/\beta = 2.09 \times 10^3$ (for $q=1.0$)

and D' , the diffusion constant, must be chosen for sapphire single crystals not having the benefit of diffusion short circuits along interfaces. From Oishi and Kingery [25] we obtain $D' = 3.5 \times 10^{-17} \text{ cm}^2/\text{sec}$ at 1400°C , or a factor of 3.5×10^{-3} lower than for polycrystalline material or for our eutectic with a large volume concentration of interfaces. For these alterations, but for all other factors remaining the same we determine a steady state creep expression for sapphire crystals of $[0001]$ orientation at 1400°C which is shown as the dashed line in Fig. 5, confirming our expectation of a lower creep resistance in comparison with the $\text{Al}_2\text{O}_3/\text{c-ZrO}_2$ eutectic.

The creep model we presented is based on the existing evidence of the measured creep rates, their stress and temperature dependence and on the findings of the earlier work of Firestone and Heuer [3] on single crystal sapphire. However, the work leaves many unanswered questions. Foremost among these are the details of the continuance of the all-important fluxes of climbing dislocations, their origins, their form of maintenance and the fine structure of cores of dislocations such as details of jogs where the actual climb steps occur by O ion vacancy emission. Preliminary energetic considerations of dislocation emission from ledges on the ubiquitous interfaces or from misfit dislocations along interfaces have indicated very large energy barriers under the prevailing local stresses. However, other forms of heterogeneous nucleation of dislocations from interfaces must still be considered. Other possibilities for inelastic

behavior such as Coble creep were discounted because of the apparent general absence of transverse boundaries in the topologically continuous Al_2O_3 component and the generally linear stress dependence of creep flow by this mechanism, which if present, appears to be swamped by dislocation climb flow. Some of these possible mechanisms as well as the missing details of the maintenance of climb fluxes could come from TEM studies which are now in progress.

Acknowledgements

This research has been supported by the AFOSR under grant F49620-99-0276. Support for equipment development and for some other research expenses was also derived from the Quentin Berg Professorship Fund of the Department of Mechanical Engineering, as well as other Departmental funds.

References

- [1] Fleischer, R.L., High strength, high temperature intermetallic compounds, *J. Mater. Sci.*, 1987, **22**, 2281-2288
- [2] Sayir, A. and Farmer, S. C., The effect of microstructure on mechanical properties of directionally solidified $\text{Al}_2\text{O}_3/\text{ZrO}_2(\text{Y}_2\text{O}_3)$ eutectic, *Acta Mater.*, 2000, **48**, 4691-4697
- [3] Firestone, R.F. and Heuer, A.H., Creep deformation of 0° degree sapphire, *J. Amer. Ceram. Soc.*, 1976, **59**, 24-29
- [4] Chiang, J., Bodur, C.T. and Argon, A.S., Pyramidal edge dislocation cores in sapphire, *Phil. Mag. Letters*, submitted for publication

- [5] Bodur, C.T., Chiang, J. and Argon, A.S., Molecular dynamics simulations of basal and pyramidal system edge dislocation cores in sapphire and their role in creep of ceramic eutectics, *J. European Ceram. Soc.* , submitted for publication
- [6] Edelin, G. and Poirier, J.P., A study of dislocation climb by means of diffusional creep experiments in Magnesium. I. Deformation mechanism, (in French) *Phil. Mag.* , 1973, **28**, 1203-1210
- [7] Morgan, P.-E.-D. and Marshall, D.B., Ceramic composites of monazite and alumina, *J. Amer. Ceram. Soc.* , 1995, **78**, 1553-1563
- [8] Lev, L.C. and Argon, A.S., Oxide-fiber/oxide-matrix composites, *Mater. Sci. & Engrg.* , 1995, **A195**, 251-261
- [9] Sayir, A., "Directional solidification of eutectic ceramics", unpublished report: NASA Glenn Research Center, private communication.
- [10] Fraser, C.S., Dickey, E.C. and Sayir, A. Crystallographic texture and orientation variants in $\text{Al}_2\text{O}_3/\text{Y}_3\text{Al}_5\text{O}_{12}$ directionally solidified eutectic crystals, *J. Cryst. Growth* , 2001, **233**, 187-195
- [11] Yi, J. and Argon A.S., X-ray diffraction determination of texture in the Al_2O_3 component of $\text{Al}_2\text{O}_3/\text{c-ZrO}_2$ eutectics, to be published.
- [12] Pastor, J.Y. Poza, P., Llorca, J., Pena, J.I., Merino, R.I. and Orera, V.M., Mechanical properties of directionally solidified $\text{Al}_2\text{O}_3/\text{ZrO}_2(\text{Y}_2\text{O}_3)$ eutectics, *Mater. Sci. & Engrg.* 2001, **A308**, 241-249
- [13] Mazerolles, L., Michol, D. and Portier, R., Interfaces in oriented $\text{Al}_2\text{O}_3/\text{ZrO}_2(\text{Y}_2\text{O}_3)$ eutectics, *J. Amer. Ceram. Soc.* , 1986, **69**, 252-255.
- [14] Dickey, E.C., Frazer, C.S., Watkins, T.R. and Hubbard, C.R., Residual stresses in high temperature ceramic eutectics, *J. European Ceram. Soc.* , 1999, **19**, (Nos 13-14), 2503-2509

- [15] Messerschmidt, U., Baufeld, B. and Baither, D., Plastic deformation of cubic zirconia single crystals, *Key-Engineering Materials* , 1998, **153-154**, 143-182
- [16] Wolfenden, A., Measurement and analysis of elastic and anelastic properties of alumina and silicon carbide, *J. Mater. Sci.* , 1997, **32**, 2275-2282
- [17] Argon, A.S., Yi, J. and Sayir, A. Creep resistance of directionally solidified ceramic eutectics of $\text{Al}_2\text{O}_3/\text{c-ZrO}_2$ with sub-micron columnar morphologies, *Mater. Sci. Engrg.* , 2001, **A319-321**, 838-842
- [18] Pollock, T.M. and Argon, A.S., Creep resistance of CMSX-3 nickel base superalloy single crystals, *Acta Metall.* , 1992, **40**, 1-30
- [19] Nabarro, F.R.N., Steady state diffusional creep, *Phil. Mag.* , 1967, **16**, 231-238
- [20] Li, J.C.M., Kinetics and dynamics in dislocation plasticity, In: "Dislocation Dynamics", edited by Rosenfield, A.R., Hahn, G.T., Bement, Jr. A.L. and Jaffee, R.I., McGraw-Hill: New York pp.87-116, 1968
- [21] Bardeen, J. and Herring, C., Diffusion in alloys and the Kirkendall effect, In: "Imperfections in Nearly Perfect Crystals", edited by Shockley, W., Hollomon, J.H., Maurer, R. and Seitz, F., J. Wiley & Sons, NY, pp.261-288, 1952
- [22] Brown, L.M. and Stobbs, W.M., Modeling structural changes in deformed dispersion strengthened crsytals, In:"Constitutive Equations in Plasticity", edited by Argon, A.S., M.I.T. Press, Cambridge, MA, pp.387-429, 1975
- [23] Friedel, J., in "Dislocations", Addison-Wesley, Reading, MA, p. 104, 1964
- [24] Groves, G.W. and Kelly, A., Change of shape due to dislocation climb, *Phil. Mag.* , 1969, **19**, 977-986
- [25] Oishi, Y. and Kingery, W.D., Self-diffusion of oxygen in single crystal and polycrystalline aluminum oxide, *J. Chem. Phys.* , 1960, **33**, 480-486.

Table 1

Recorded Steady State Strain Rates

Stress (MPa)	Strain Rate $\dot{\epsilon}$ (sample #)[$\dot{\epsilon}$ average rate] (sec^{-1})
1200°C	
200	1.97×10^{-10} (142-18)
1400°C	
200	3.6×10^{-9} (187-29)
225	2.26×10^{-9} (187-27-2); 8.16×10^{-9} (187-27-1) [5.21×10^{-9}]
250	5.53×10^{-9} (187-29)
275	9.95×10^{-9} (187-27-2); 1.10×10^{-8} (187-27-1) [1.048×10^{-8}]
1520°C	
150	1.57×10^{-9} (142-16); 4.40×10^{-9} (142-16) [2.98×10^{-9}]
200	1.20×10^{-8} (142-16); 1.60×10^{-8} (142-16) [1.40×10^{-8}]

Table 2

Material Properties for Linear Elastic FEM Analysis

	Al_2O_3	c-ZrO ₂
Young's Modulus	200GPa at 1400°C	0.05MPa at 1400°C
Possion's ratio	0.3	0.4999999
Yield Stress (GPa)	5.0GPa [†]	5.0GPa [†]
Thermal Expansion	9.1×10^{-6} (a) 9.9×10^{-6} (c)	$12.9 \cdot 10^{-6}$

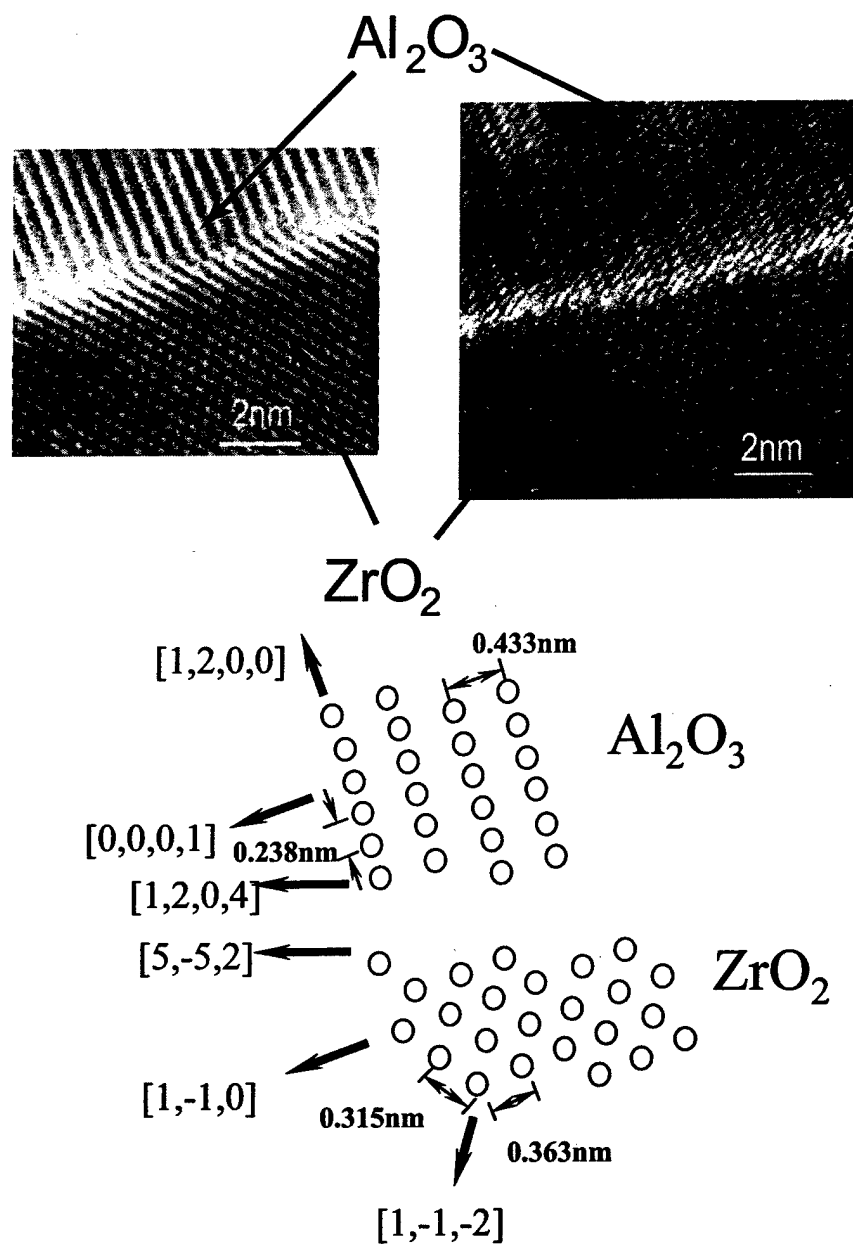


Fig. 1. A direct lattice image of a typical interface between Al_2O_3 and c- ZrO_2 in an $\text{Al}_2\text{O}_3/\text{c-ZrO}_2$ eutectic

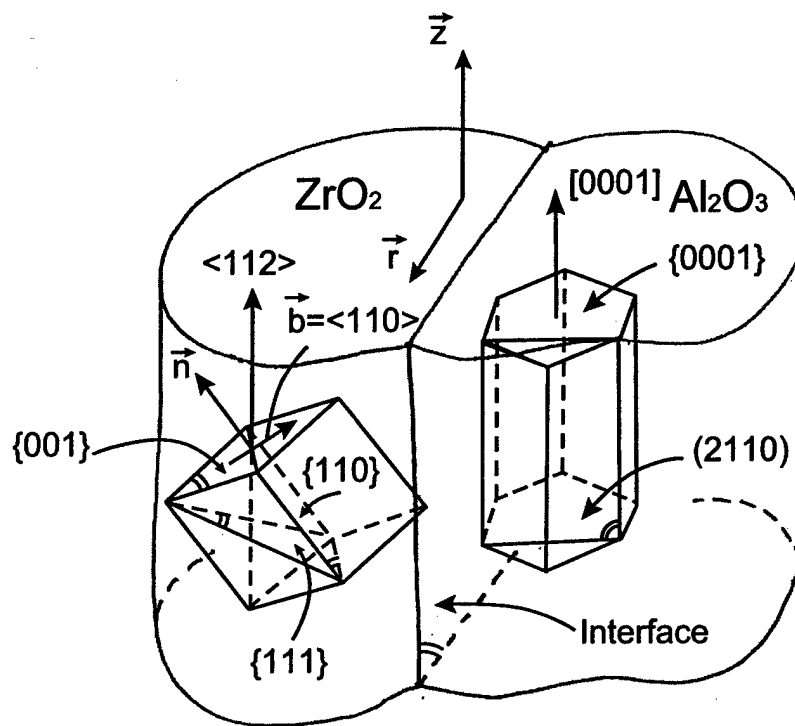


Fig. 2. Sketch showing the textural arrangement of the Al_2O_3 component with a preferred $[0001]$ axis and c- ZrO_2 with a preferred $\langle 112 \rangle$ axis found by electron diffraction analysis. Other textures for c- ZrO_2 have also been reported.

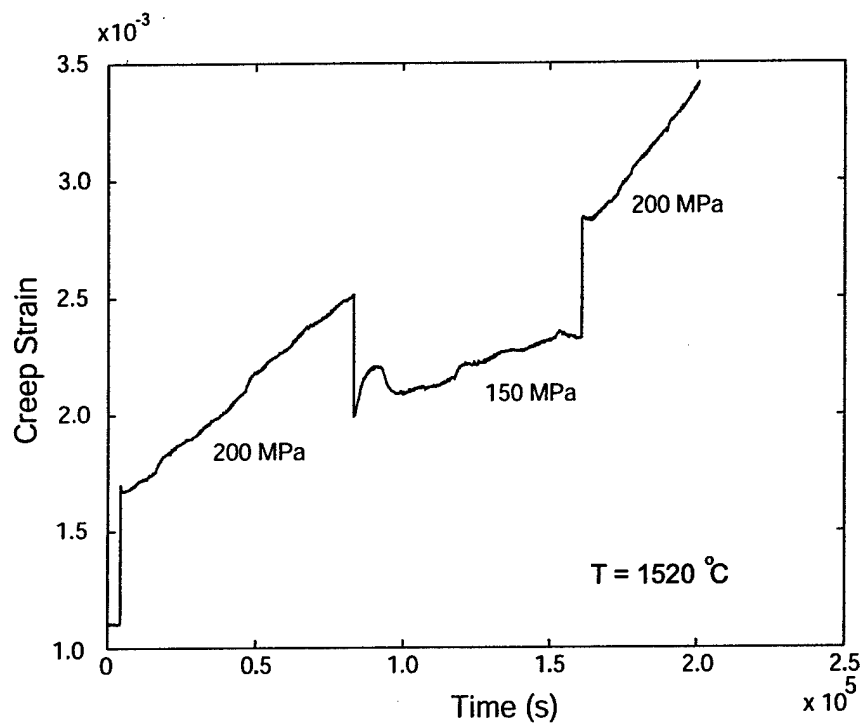


Fig. 3. A typical strain time plot for steady state creep at two different stress levels in an $\text{Al}_2\text{O}_3/\text{c-ZrO}_2$ eutectic rod at 1520°C

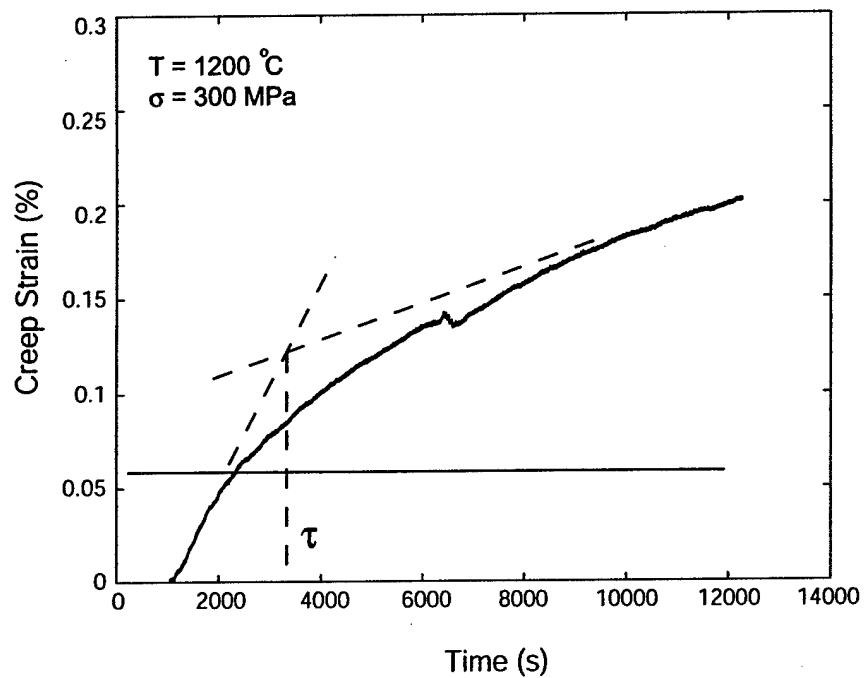


Fig. 4. A typical creep strain transient in an $\text{Al}_2\text{O}_3/\text{c-ZrO}_2$ eutectic under a stress of 200 MPa at a temperature of 1200°C . The horizontal line gives an estimate of creep strain increment due to stress relaxation in the coarse fraction of c-ZrO₂.

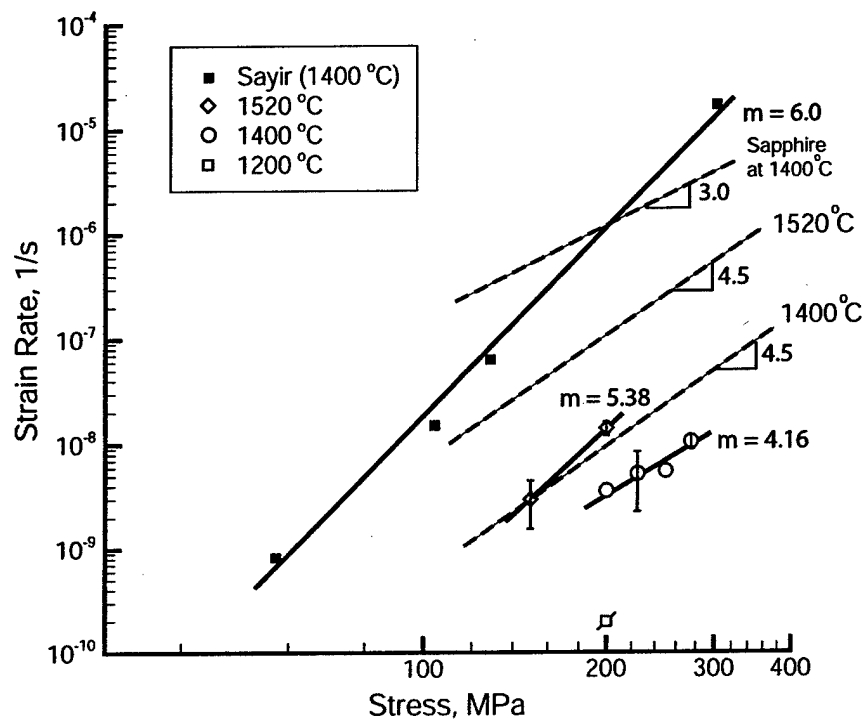


Fig. 5. Plots of steady state creep rates as a function of stress for temperatures of 1200, 1400 and 1520°C compared with measurements reported by Sayir and Farmer [2]. Broken lines represent predictions of creep model for $\text{Al}_2\text{O}_3/\text{c-ZrO}_2$ at 1400°C and 1520°C, together with model prediction for sapphire at 1400°C

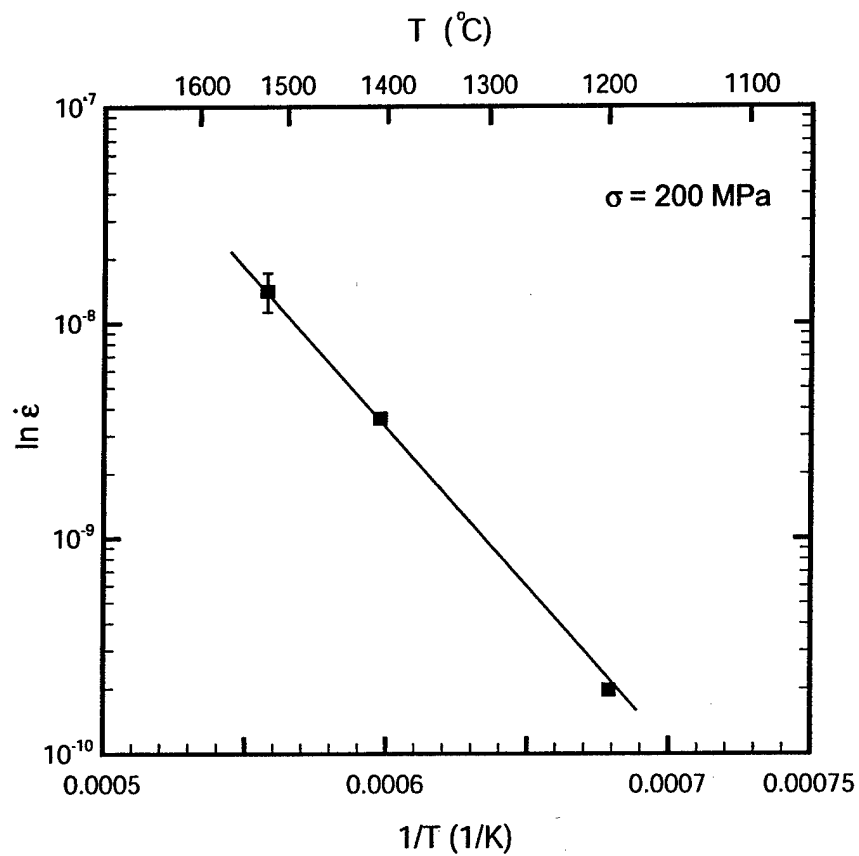


Fig. 6. Determination of activation energy of steady state creep from temperature dependence of steady state creep rate.

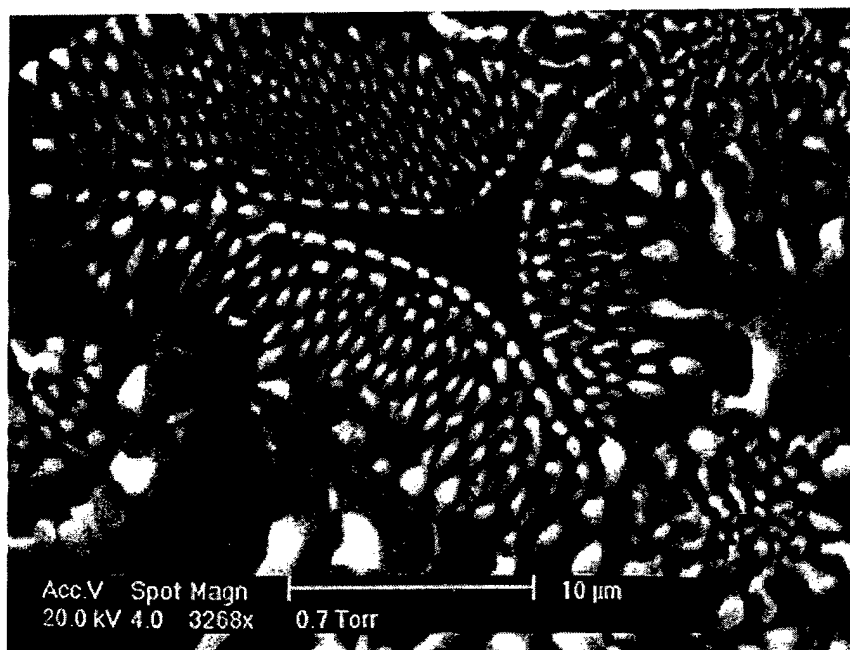


Fig. 7. An SEM micrograph of a typical morphology of the Al₂O₃/c-ZrO₂ eutectic, as revealed in a transverse section. The black component is Al₂O₃. Much of the c-ZrO₂ component (the white regions) is of low sub-micron size and is expected not to deform by any form of crystal plasticity.

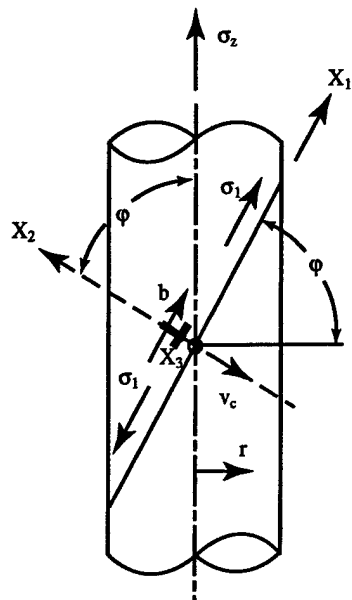


Fig. 8. Sketch of a round bar of a $\text{Al}_2\text{O}_3/\text{c-ZrO}_2$ eutectic with z axis parallel to the $[0001]$ direction of the Al_2O_3 . The plane at angle ϕ outlines a pyramidal glide plane. A local tensile stress σ_1 will make a positive edge dislocation climb in the negative X_2 direction.

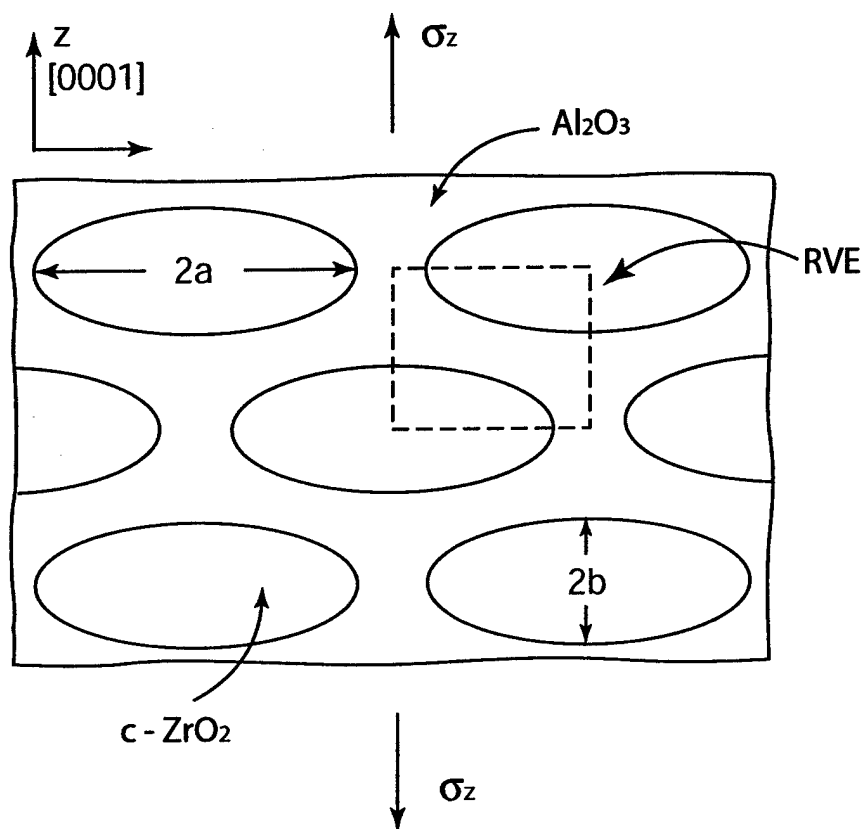


Fig. 9. Sketches of an idealization of the $c\text{-ZrO}_2$ domains as ellipsoidal cylinders in the topologically continuous Al_2O_3 component, for the purpose of a FEM study of the internal stress distribution in the Al_2O_3 when a tensile stress σ_z is applied.

S, Mises
(Ave. Crit.: 75%)

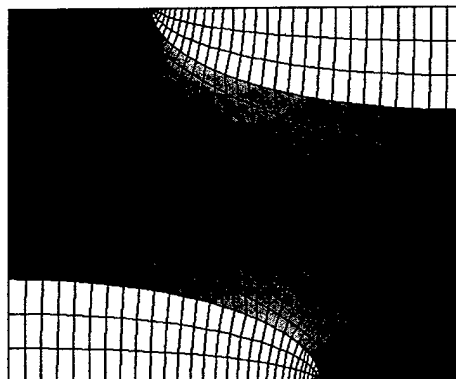
	+6.668e+02
	+6.113e+02
	+5.557e+02
	+5.001e+02
	+4.446e+02
	+3.890e+02
	+3.334e+02
	+2.778e+02
	+2.223e+02
	+1.667e+02
	+1.111e+02
	+5.557e+01
	+2.147e-04



(a)

Resolved Climbing Stress
(Ave. Crit.: 75%)

	+3.849e+02
	+3.558e+02
	+3.267e+02
	+2.976e+02
	+2.685e+02
	+2.394e+02
	+2.103e+02
	+1.812e+02
	+1.521e+02
	+1.231e+02
	+9.395e+01
	+6.486e+01
	+3.576e+01



(b)

Fig. 10. Stress distribution results of the FEM study; a) deviatoric (Mises) stresses in the two components of the eutectic; b) the distribution of the climb stress σ_1 in the Al_2O_3 .

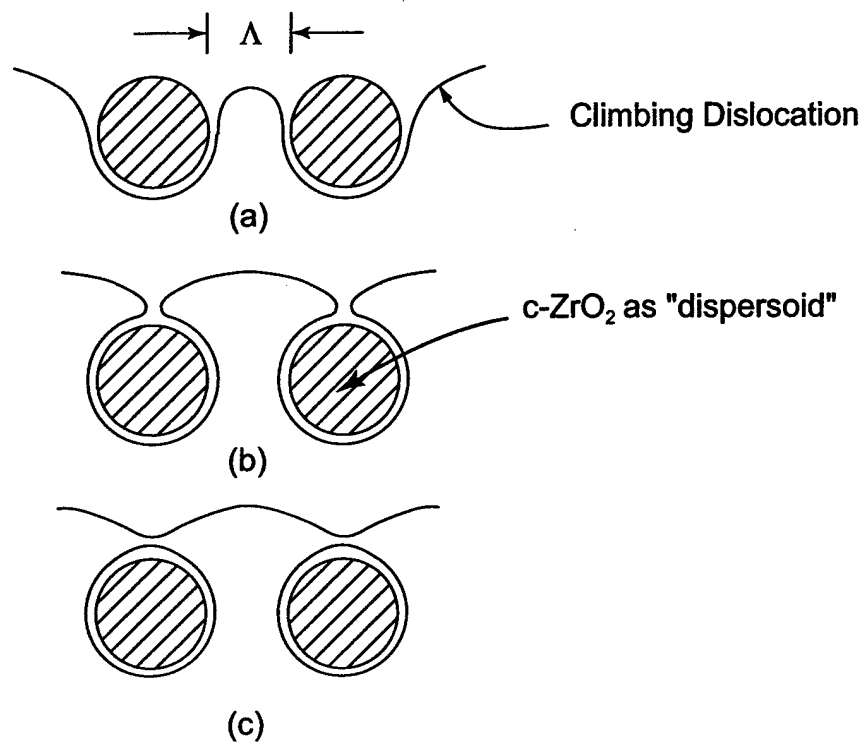


Fig. 11. Sketch depicting the required contortions that a climbing edge dislocation need to suffer in bowing through the gaps between the c-ZrO₂ domains that we consider to be impenetrable: a) critical climb configuration to bow through the gap between two c-ZrO₂ dispersoids at a spacing Λ ; b) at the point when the climbing dislocation is just about to pinch off; c) the cusped dislocation line straightening out under the application of line tension.

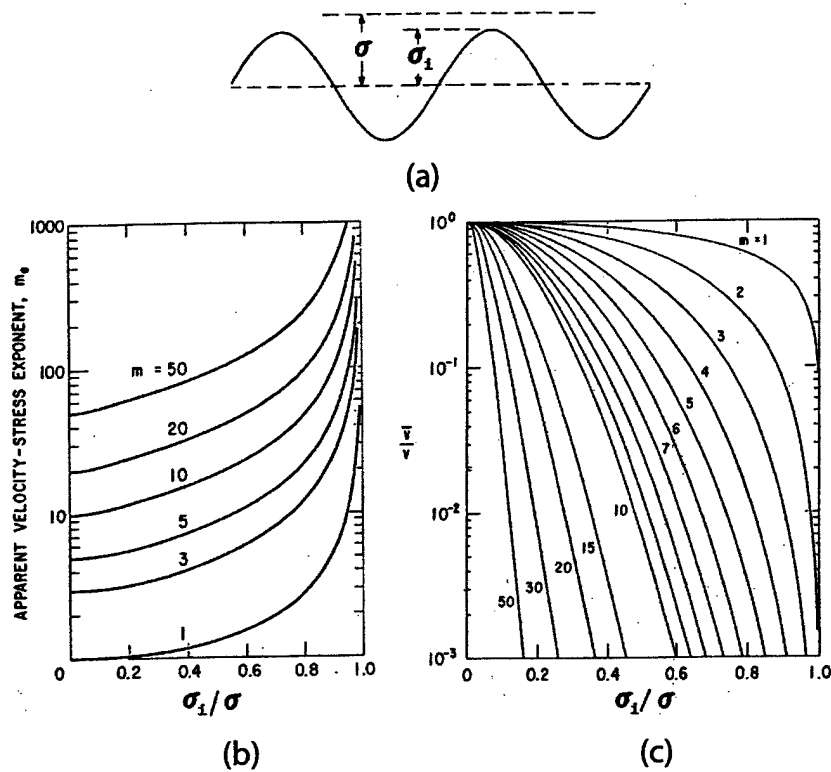


Fig. 12. Consequence of the repeated bowing out and straightening of the climbing dislocation considered as a set of internal resistance σ_i ; alternately retarding and speeding up the climbing dislocation: a) retardation and speeding up considered as unfavorable and favorable internal stresses σ_i in the presence of a climb stress σ ; b) effect of σ_i/σ on the overall stress exponent m of the dislocation velocity; c) effect of σ_i/σ on the attenuation factor C on the average climb velocity. (figures reproduced from Li [20], courtesy of J. Wiley & Sons)

A The kinematics of creep strain rate by climb

As presented in Section 4.2, if a single set of parallel edge dislocations of density ρ were to climb with a velocity v_c , a strain rate $\dot{\epsilon}_0 = b\rho v_c$ would result in the direction perpendicular to the plane of the climbing dislocations.

Referring now to Fig. 8, consider the coordinate axis set 1,2,3 of a pyramidal glide system in a round bar of Al_2O_3 where the 1 axis is parallel to the Burgers vector of the pyramidal edge dislocations and the 1,3 pyramidal plane makes an angle ϕ with respect to the bar axis z . Under a tensile stress σ_1 then, a density ρ of dislocations climbing in the 2 direction (positive edge dislocations in the negative 2 direction and negative edge dislocations in the positive 2 direction) a creep rate $\dot{\epsilon}_0$ in the 1 direction would result. However, such climb requires extension of extra half planes which requires material fluxes to arrive to the dislocation from all directions and dispersal of vacancies into all directions, resulting in contractile strain rates $\dot{\epsilon}_{1c}, \dot{\epsilon}_{2c}, \dot{\epsilon}_{3c}$. For preservation of volume, it would be necessary that

$$\dot{\epsilon}_0 + \dot{\epsilon}_{1c} + \dot{\epsilon}_{2c} + \dot{\epsilon}_{3c} = 0 \quad (\text{A.1})$$

and since by symmetry

$$\dot{\epsilon}_{1c} = \dot{\epsilon}_{2c} = \dot{\epsilon}_{3c} \quad (\text{A.2})$$

we have net strain rates

$$\dot{\epsilon}_1 = \frac{2}{3}\dot{\epsilon}_0 \quad (\text{A.3a})$$

and

$$\dot{\epsilon}_2 = \dot{\epsilon}_3 = -\frac{1}{3}\dot{\epsilon}_0 \quad (\text{A.3b})$$

Resolving these strain rates into the axes r , and z of the creep bar we have

$$\dot{\epsilon}_z = \left(\frac{2}{3} - \cos^2\phi\right)\dot{\epsilon}_0 \quad (\text{A.4a})$$

$$\therefore \dot{\epsilon}_r = -\left(\frac{1}{3} - \frac{1}{2}\cos^2\phi\right)\dot{\epsilon}_0 \quad (\text{A.4b})$$

Since there are three sets of pyramidal dislocations, all with equal capacity to contribute to axial strain rate, we take the total axial strain rate to be

$$\dot{\epsilon}_z = (2 - 3\cos^2\phi)\dot{\epsilon}_0 \quad (\text{A.5a})$$

and

$$\dot{\epsilon}_r = -\left(1 - \frac{3}{2}\cos^2\phi\right)\dot{\epsilon}_0 \quad (\text{A.5b})$$

where the dislocation velocity in $\dot{\epsilon}_0$ is still related to tensile stresses parallel to the Burgers vectors of the pyramidal dislocations. Resolving these tensile stresses to the axial tensile stress σ_z , then gives the climb-causing tensile stresses

$$\sigma_1 = q\sigma_z(1 - \cos^2\phi) \quad (\text{A.6})$$

where the factor q , which needs to be determined from a FEM boundary value problem, refers to the volume average of the climb producing stress in the Al_2O_3 component between the c-ZrO₂ components. This development is discussed in Section 4.3.

MECHANICAL PROPERTIES OF DIRECTIONALLY SOLIDIFIED

Al_2O_3 - Al_2TiO_5 CERAMIC

Ali Sayir

NASA Glenn Research Center, Cleveland, Ohio - USA

Carmen Baudín

Instituto de Cerámica y Vidrio CSIC – Madrid - SPAIN

Marie-Helene Berger

Ecole des Mines de Paris – FRANCE

Paula Heimann

Ohio Aerospace Institute (OAI) Cleveland, Ohio - USA

The mechanical properties of two-phase eutectics can be superior to that of either constituent alone due to the strong constraining effects of the interlocking microstructure. The present work focuses on the solidification characteristics and mechanical properties of Al_2O_3 - Al_2TiO_5 system. The challenge for the development of Al_2O_3 - Al_2TiO_5 is to improve the mechanical strength and toughness concurrently with a high resistance to thermal decomposition. The solidification at the invariant eutectic point and Al_2O_3 rich region of the off-eutectic compositions was studied. The solidification characteristic and its relation to produce an in-situ composite material will be discussed at some length. Critical to this effort is the correlation of mechanical properties with eutectic growth data. The strength is strongly related to the starting volume fraction of the minor phase. High strength in the order of 340 MPa is associated with high Al_2O_3 content. Bend tests showed a large displacement for all compositions studied. The tortuous fracture surfaces resulting from these tests were also strongly encouraging. HRTEM analysis revealed that two different phases of Al_2TiO_5 were present. The lattice constant of the Al_2TiO_5 phases were markedly different from the sintered materials. The spatial arrangement of the new α -, and β - Al_2TiO_5 phases around the reinforcing Al_2O_3 dendrites and microcracking were responsible for the improved toughness.

Dopant Studies in the $\text{BaCe}_{0.9-x}\text{Zr}_x\text{Y}_{0.1}\text{O}_{3-\delta}$ High Temperature Protonic Conductor

Zhimin Zhong^{1,2,*}, Ali Sayir^{1,2}, Fred Dynys¹, Paula Heimann^{1,3}

1 NASA Glenn Research Center, Cleveland, OH, USA

2 Case Western Reserve University, Cleveland, OH, USA

3 Ohio Aerospace Institute, Cleveland, OH, USA

Protonic separation membranes for the hydrogen industry require thermo-chemical stability and high conductance. The perovskite $\text{BaCe}_{0.9}\text{Y}_{0.1}\text{O}_{3-\delta}$ exhibits excellent proton conduction at high temperatures, but shows poor thermo-chemical stability. Substituting Zr for Ce, $\text{BaZr}_{0.9}\text{Y}_{0.1}\text{O}_{3-\delta}$, improves the thermo-chemical stability but significantly reduces proton conduction. The objective of this work was to study the optimization of protonic conductance and thermo-chemical by changing the ratio of Ce to Zr in $\text{BaCe}_{0.9-x}\text{Zr}_x\text{Y}_{0.1}\text{O}_{3-\delta}$. To elucidate the dopant effect, co-precipitation method has been developed to produce single phase perovskites of composition $\text{BaCe}_{0.9-x}\text{Zr}_x\text{Y}_{0.1}\text{O}_{3-\delta}$ ($0 \leq x \leq 0.9$).—The co-precipitation method has been optimized to yield high purity and homogeneous powders with a particle size of 100-200 nm in diameter. The sintering characteristics were studied in temperature range of 900-1400 °C and characterized using XRD and SEM. The effect of Zr substitution on sintering behavior, protonic conductance and thermo-chemical stability will be reported.



Pergamon

Available online at www.sciencedirect.com

SCIENCE @ DIRECT®

Acta Materialia XX (2003) XXX–XXX

www.actamat-journals.com

High temperature creep deformation of directionally solidified $\text{Al}_2\text{O}_3/\text{Er}_3\text{Al}_5\text{O}_{12}$

J. Martinez Fernandez ^{abc,*}, A. Sayir ^{ab}, S.C. Farmer ^a^a NASA Glenn Research Center, 21000 Brookpark Road, Cleveland, OH 44135, USA^b Case Western Reserve University, Cleveland, OH 44135, USA^c Departamento de Física de la Materia Condensada, Universidad de Sevilla, Seville, Spain

Received 12 September 2002; received in revised form 13 November 2002; accepted 30 November 2002

Abstract

The microstructure of directionally solidified $\text{Al}_2\text{O}_3/\text{Er}_3\text{Al}_5\text{O}_{12}$ (19.5 mol% Er_2O_3) is analyzed and high temperature creep deformation studied using fibers in tension between 1400° C and 1550° C. The directionally solidified $\text{Al}_2\text{O}_3/\text{Er}_3\text{Al}_5\text{O}_{12}$ system is an in situ composite and has a fine eutectic- microstructure with sub-micron phase spacing. The microstructure is elongated in the direction of growth. Transmission electron microscopy observations revealed well-bonded interfaces and scatter within the crystallographic alignment of the constituent phases. The creep resistance of the system was very high, comparable to c-axis sapphire, and failure initiated at the lamella interfaces. The influence of the different elastic and plastic behaviors of the eutectic components on creep is examined. A critical discussion on the origin of the high stress dependence of the creep rate, the existence of steady state creep, and the relevant microscopic deformation mechanisms is presented.

© 2003 Acta Materialia Inc. Published by Elsevier Science Ltd. All rights reserved.

Keywords: Creep; High temperature; Eutectic; Strain recovery

1. Introduction

The eutectic architecture of a continuous reinforcing phase within a continuous higher volume phase or matrix can be considered as a naturally occurring in situ composite. Directionally solidified eutectic ceramics show superior creep resistance and attractive high temperature strength reten-

tion [1–13] but a clear explanation of the origin for the superior mechanical properties is not available.

A systematic study has been initiated at NASA Glenn Research Center aimed at identifying the sources of high levels of creep resistance in directionally solidified in situ composites. Directional solidification at compositions near the eutectic composition produces very fine microstructures, whereas solidification at off-eutectic compositions alters both the size and volume fraction of each phase. Directional solidification over a selected composition range of the phase field produced microstructures ranging from the 100 nm scale at the eutectic composition to 50 μm at strongly

* Corresponding author. Tel.: +34-954-556-956; fax: +34-954-612-097.

E-mail address: martinez@us.es (J. Martinez Fernandez).

hypo-eutectic compositions (cellular microstructure) [6, 7, 14]. The nature of the interphase-interfaces [1, 3, 13] is not expected to change during solidification at different volume fraction of the phases, or at eutectic or hypoeutectic compositions. The focus of this article is on the deformation characteristic of the $\text{Al}_2\text{O}_3/\text{Er}_3\text{Al}_5\text{O}_{12}$ system near the eutectic region and the effect of volume fraction (lamella dimensions) at hypoeutectic compositions will be presented in a future article.

The $\text{Al}_2\text{O}_3/\text{Er}_3\text{Al}_5\text{O}_{12}$ composition was selected to examine intrinsic characteristics of the directionally solidified $\text{Al}_2\text{O}_3/\text{garnet}$ systems. There are no previous deformation studies on the $\text{Al}_2\text{O}_3/\text{Er}_3\text{Al}_5\text{O}_{12}$ system. Data on the $\text{Al}_2\text{O}_3/\text{Y}_3\text{Al}_5\text{O}_{12}$ system is available [1, 2, 8, 12] and provides a basis for comparison with different $\text{Al}_2\text{O}_3/\text{rare-earth garnet}$ systems. The approach for the use of monofilaments has been adopted to permit a uniaxial tension test that provides data regarding the intrinsic potential of the $\text{Al}_2\text{O}_3/\text{Er}_3\text{Al}_5\text{O}_{12}$ system.

2. Experimental procedure

$\text{Al}_2\text{O}_3/\text{Er}_3\text{Al}_5\text{O}_{12}$ fibers (19.5 mol% Er_2O_3) were grown by the laser heated float zone method in air as described in previous publications [5, 6]. The source rods were prepared by extrusion without pre-sintering. To initiate directional solidification, a seed of single crystal (0001) Al_2O_3 was used. The pulling rate was the same for all the fibers (38 cm/h). The monofilament diameter ranged from 140 to 160 μm (typical diameter oscillation of approximately 10 microns along the fiber) with lengths up to 40 cm.

Tensile creep deformation was studied using dead-weight loads and cold grips at elevated temperatures. Most of the deformation experiments were run in air placing the central part of the fiber in a MoSi_2 furnace (CM. Inc., Bloomfield, NJ, USA) with a 2.5 cm hot zone. The monofilament was protected with a high purity polycrystalline alumina or sapphire tube to eliminate any interaction with the heating elements and to thus minimize fiber contamination. Experiments in vacuum

were run using a tantalum furnace (Oxy-gon Industries Inc, Epsom, NH, USA) with a 7 cm hot zone. The use of a vacuum environment eliminates the strain reading noise caused by oscillations of the room temperature and by the flow of hot air. This is very critical for the accurate study of loading transients and creep recovery. The test temperatures ranged from 1400° C to 1550° C. The applied stresses ranged from 80 to 500 MPa. The elongation was measured with a linear variable differential transducer (LVDT).

The microstructures of as-fabricated and deformed monofilaments, mounted in epoxy resin and polished, were studied by scanning electron microscopy (SEM). The small diameter monofilament geometry was particularly effective in that it cools rapidly. Quenching better retains the high temperature microstructure. Specimens were thinned to electron transparency and studied using transmission electron microscopy (TEM). Special care was taken when preparing TEM foils from crept samples. A precision ion thinner was used and the electron transparent regions were obtained at distances less than 2 mm from the fracture surface.

3. Results

3.1. As-fabricated microstructure

A representative cross-section of directionally solidified $\text{Al}_2\text{O}_3/\text{Er}_3\text{Al}_5\text{O}_{12}$ ceramic is shown in Fig. 1. The microstructure consists of alternating lamellae of Al_2O_3 (black contrast) and $\text{Er}_3\text{Al}_5\text{O}_{12}$ (white contrast). The $\text{Er}_3\text{Al}_5\text{O}_{12}$ volume fraction calculated from the area fraction on SEM micrographs is $60.4 \pm 8.6\%$, the scatter being due to variation between sectional cuts of the fiber. The microstructure consists of eutectic regions and erbium-rich precipitates indicating that the selected composition (the eutectic composition on the phase diagram [15]) lies slightly outside the cooperative growth region of this system for the processing conditions used. The average lamellae widths for Al_2O_3 and $\text{Er}_3\text{Al}_5\text{O}_{12}$ phases were $0.31 \pm 0.23 \mu\text{m}$ and $0.46 \pm 0.35 \mu\text{m}$, respectively. Figure 2 shows a representative longitudinal section. The cells are

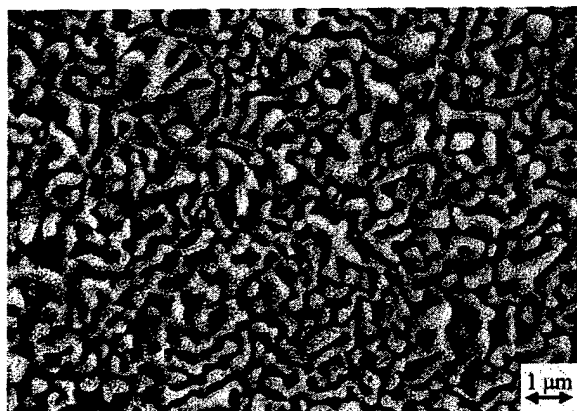


Fig. 1. SEM micrograph of directionally solidified $\text{Al}_2\text{O}_3/\text{Er}_3\text{Al}_5\text{O}_{12}$ cross-section showing the complexity of the fine interlocking microstructure. The white regions are garnet and the black regions are alumina.



Fig. 2. SEM micrographs of directionally solidified $\text{Al}_2\text{O}_3/\text{Er}_3\text{Al}_5\text{O}_{12}$ longitudinal section showing that the microstructure is elongated in the direction of growth. The tri-dimensional continuity of the phases is clear from Figs 1 and 2.

elongated in the direction of growth with aspect ratios between 5 to 25. In many areas, however, it was difficult to assign an aspect ratio due to the tri-dimensional continuity of the phases.

There is scatter in the crystallographic orientation between Al_2O_3 and $\text{Er}_3\text{Al}_5\text{O}_{12}$ erbium aluminum garnet.¹ In Fig. 3 some frequently found orientations are shown: c-axis in the alumina

lamella is forming 5° – 10° with the fiber axis (zone axis $[2\bar{1}10]$ at 5° from the foil plane), and garnet with the $[110]$ direction parallel to the fiber axis (zone axis $[01\bar{1}]$ perpendicular to foil plane). Additional orientations further off-axis than shown in Fig. 3 are also found. The crystallographic orientations of neighboring lamellae of the same phase are similar, indicating that change of orientation within a phase occurs gradually. TEM observations indicate that the interfaces are sharp, suggesting a strong bonding between phases.

3.2. Tensile creep deformation

The creep curves show a primary creep regime where the creep rate decreases continuously. Figure 4 shows a typical creep deformation curve at low stress (190 MPa at 1400°C) where the creep rate decreases to the limit of detection ($\approx 5 \times 10^{-10} \text{ s}^{-1}$), with total plastic strains of about 0.05%. When the applied stress is higher (433 MPa at 1400°C), the system reaches a quasi-steady state deformation up to failure at total strains of approximately 0.2%, Fig. 5.

Whether or not a portion of the creep curve appears linear over a certain time interval depends on the time scale of the creep curve. The quasi-steady-state regime in this work is determined by plots of the strain-rate against the true strain as suggested by Poirier [16]. The creep deformation rate, however, was history dependent. Experiments in which the stress and/or temperature was changed and subsequently returned to the initial stress and temperature levels exhibited strain rates markedly lower than the original strain rates at a given stress or temperature condition (Fig. 6). This indicates that a true stationary-state was not reached and the prefix quasi is used to describe the observed deformation regions. Quasi-steady-state strain characteristics of the directionally solidified ceramics gave additional impetus to include the raw data shown in Figs 4 and 5 for completeness.

The $\text{Al}_2\text{O}_3/\text{Er}_3\text{Al}_5\text{O}_{12}$ system exhibits remarkable creep resistance and requires very high loads to initiate deformation. Figure 7 shows the quasi-steady-state creep rates for the temperature and stress regimes tested. The creep rate is very sensitive to the applied stress, having a power law fit

¹ Garnet will be used from now on to refer to erbium aluminum garnet phase.

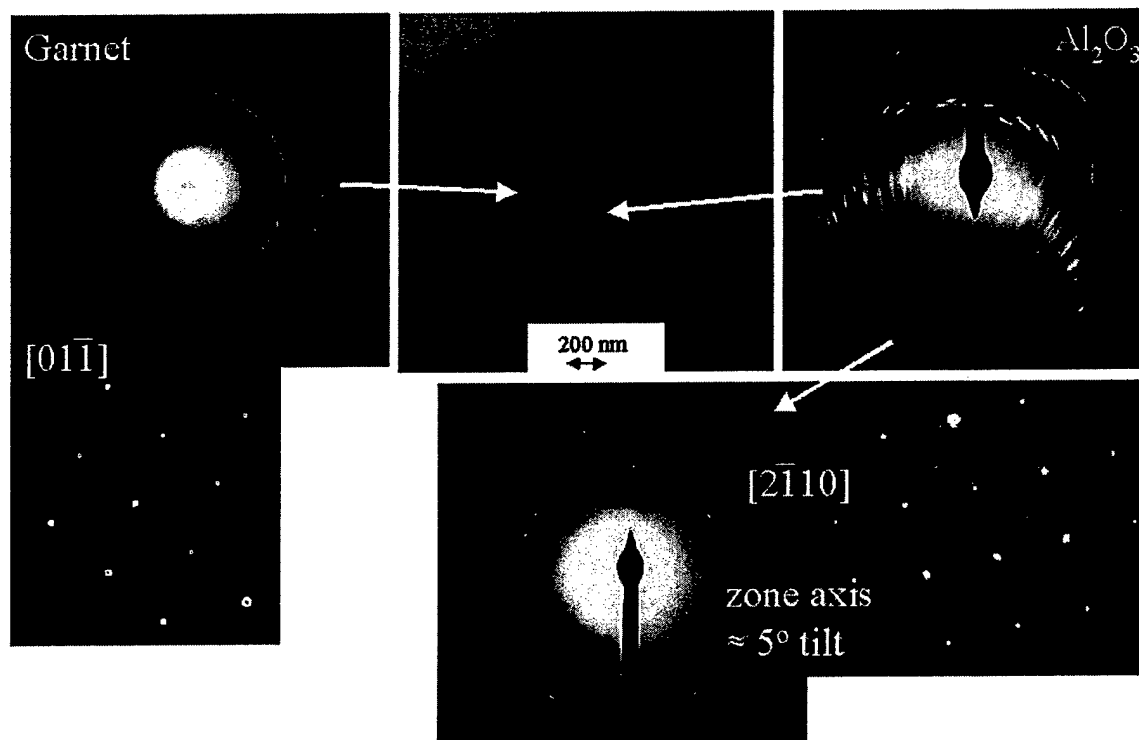


Fig. 3. TEM micrographs of the as-fabricated microstructure (foil prepared in the longitudinal direction, the white regions are alumina and the black regions are garnet). Diffraction patterns are included. In the case of the alumina region the diffraction pattern after tilting to a low index region is also included. The monofilament axis is parallel to the $[110]$ direction in garnet and forms 5° – 10° with the c -axis in alumina.

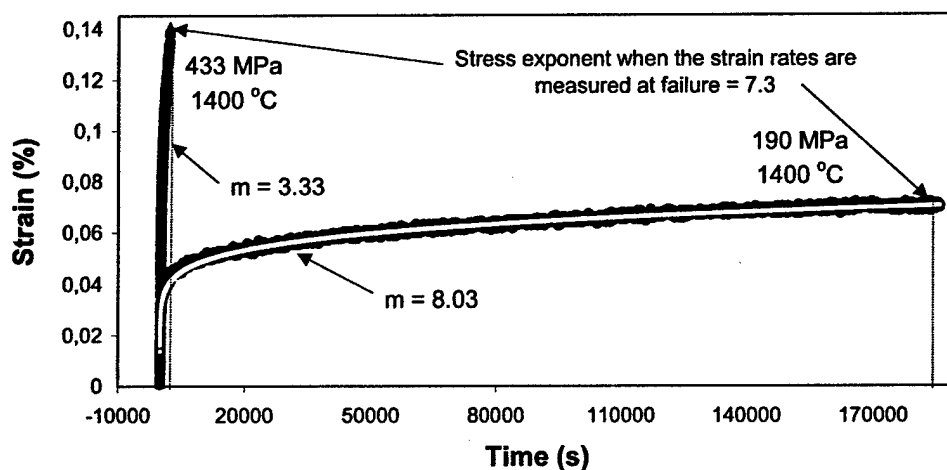


Fig. 4. Creep curve at 1400°C under a stress of 190 MPa. The curve of Fig. 5 is also included to illustrate the calculation of the stress exponent from the creep rates at failure. Because deformation occurs in the primary creep regime, the stress exponent obtained this way is overestimated.

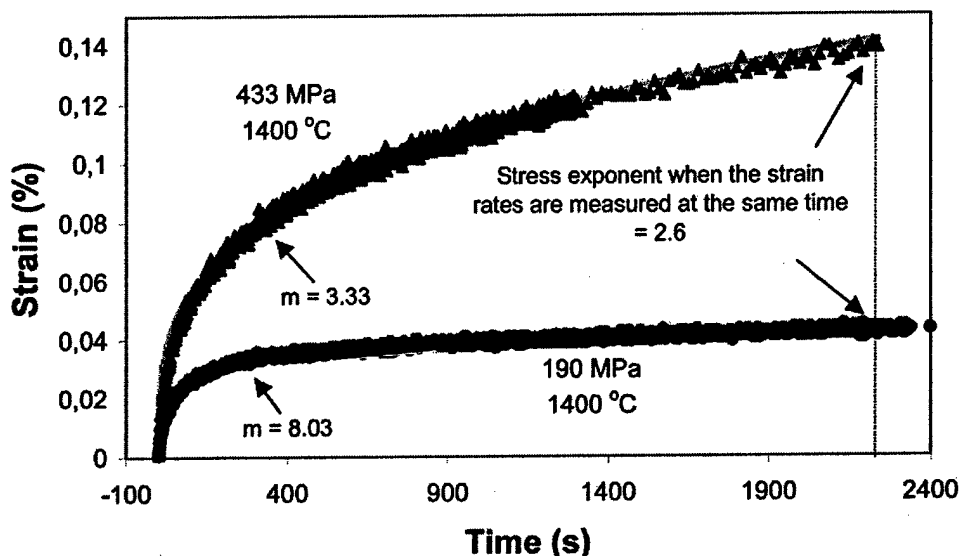


Fig. 5. Creep curve at 1400° C under a stress of 430 MPa. The curve of Fig. 4 is also included to illustrate the calculation of the stress exponent at a given time. This is a more accurate way to calculate the stress dependence of strain rate when deformation occurs in the primary creep regime.

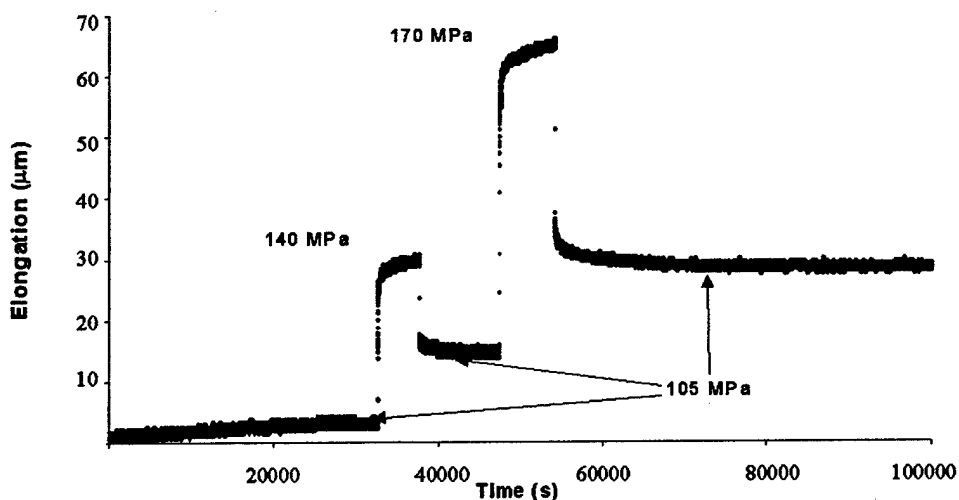


Fig. 6. Creep curve at 1400° C with load increments and decrements. The strain rate at 105 MPa decreases after the first load increments (140 MPa), and creep recovery (contraction of the monofilament) is observed after the 170 MPa load increment. Creep recovery is due to the release of elastic stresses built up in the garnet phase during deformation.

with a high exponent (between 4 to 5). The scatter in the data is largely attributed to the non-uniformity of the fiber diameter. The stress exponent is also determined by incremental application of the load during one single experiment. The incremental load approach gave a similar stress exponent

$n=4.1$, $R^2=0.9999$. In Fig. 7, the data points obtained from a single specimen by incremental loading mode at 1500° C have been included for comparison (dashed line). The activation energy obtained by temperature increments at constant load was 5.1 eV (492 kJ mol^{-1} , $R^2=0.9778$), Fig. 8.

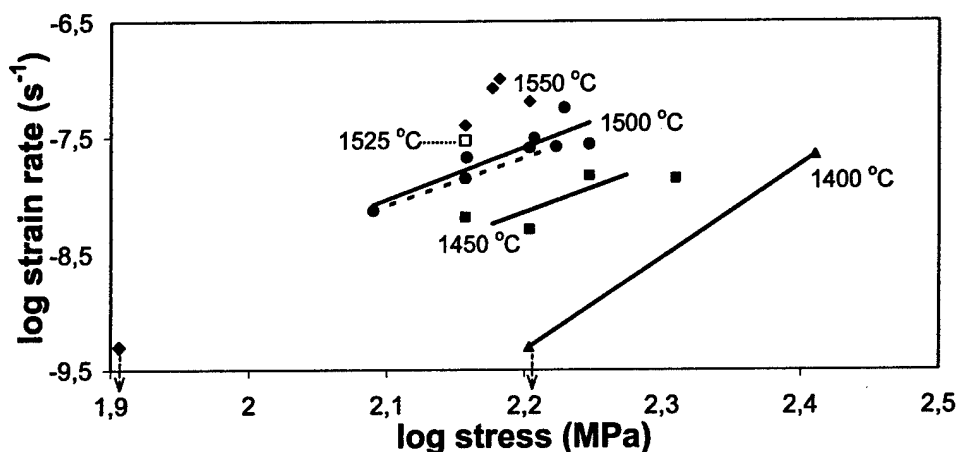


Fig. 7. Plot of the creep rates before failure versus stress (the arrow indicates that a strain rate was not measurable). The data points marked with a dashed line are obtained from the same experiment giving a stress exponent of 4.1 ($R^2=0.999$).

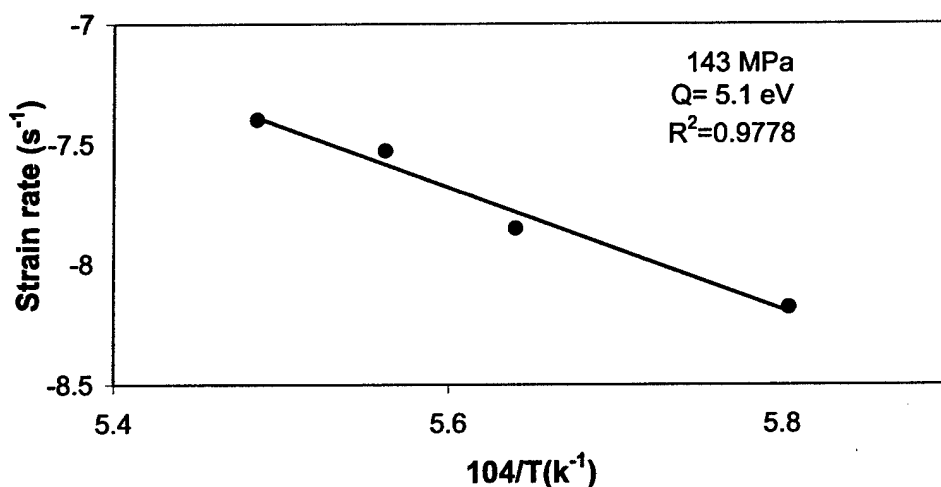


Fig. 8. Plot of the creep rates versus the reciprocal of the temperature for experiments at constant load with temperature increments. The activation energy for creep is compatible with the diffusion data available for different species in alumina and garnet [25, 27].

In Fig. 9, the strain rate at 100 MPa is plotted as a reciprocal of the absolute temperature. The normalized strain characteristic of $\text{Al}_2\text{O}_3/\text{Er}_3\text{Al}_5\text{O}_{12}$ at 100 MPa was calculated using a stress exponent of 4.5. Data from the literature in other oxide ceramics is also included for comparison [6, 8, 17–20]. The creep resistance of the $\text{Al}_2\text{O}_3/\text{Er}_3\text{Al}_5\text{O}_{12}$ system is very high, comparable to c-axis sapphire up to 1550 °C. The extrapolation of the data on sapphire is indicated with a dashed line. The high creep resistance of $\text{Al}_2\text{O}_3/\text{Er}_3\text{Al}_5\text{O}_{12}$ system is even

more striking given that the Al_2O_3 lamella have some degree of misalignment. The creep resistance of Al_2O_3 decreases dramatically with small misalignments as indicated by the data included in Fig. 9. It must be noted that the creep resistance of the $\text{Al}_2\text{O}_3/\text{Er}_3\text{Al}_5\text{O}_{12}$ system is 3 or 4 orders of magnitude better than 15° off c-axis sapphire.² From the

² Data was normalized from 300 MPa to 100 MPa with a stress exponent of 4, typical on Al_2O_3 single crystals [17].

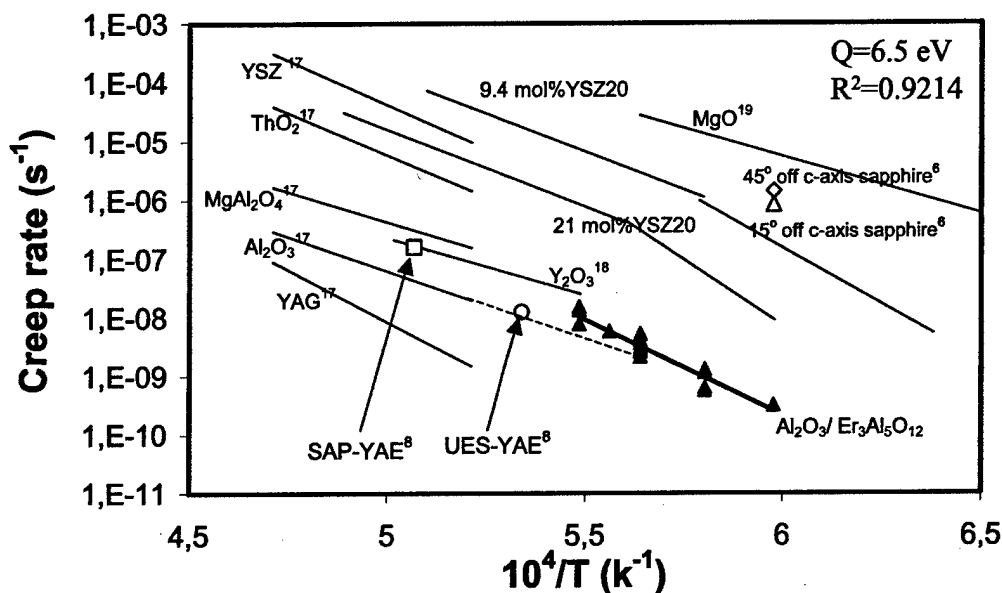


Fig. 9. Comparison of the creep rate versus reciprocal of temperature (normalized at 100 MPa) of the system studied in this work (black triangles) and other structural oxides [6, 17–20]. SAP and UES are commercial alumina-YAG fibers with eutectic composition [8]. The creep resistance of the $\text{Al}_2\text{O}_3/\text{Er}_3\text{Al}_5\text{O}_{12}$ is very high, comparable to c-axis sapphire (the extrapolation of the data on sapphire is indicated with a dashed line).

practical point of view, the $\text{Al}_2\text{O}_3/\text{Er}_3\text{Al}_5\text{O}_{12}$ system is superior to Al_2O_3 as its mechanical properties are not as sensitive as sapphire to small misalignments. The activation energy calculated from this plot is 6.5 eV (626 kJ mol^{-1} , $R^2=0.9214$). The incremental temperature calculation referred to previously (492 kJ mol^{-1} , $R^2=0.9778$) is more reliable because it does not require normalization with stress.

3.3. Microstructure of deformed specimen

Details of a representative fracture surface is shown in Fig. 10. The fracture surfaces are rough indicating that the damage propagation involves crack branching. At higher stress concentrations damage accumulation at the lamella interfaces most likely leads to failure originating at this boundary.

Extensive TEM observations were made in samples which were carefully thinned adjacent to the fractured surface of the specimens that were subjected to uniaxial deformation at temperatures from 1400°C to 1650°C . Very limited dislocation



Fig. 10. SEM micrograph of the fracture surface of a fiber crept at 1400°C . It can be seen how cracks propagate preferentially at the interfaces (arrowed). Damage is also probably nucleated at the interfaces due to the high shear stress associated to the different elastic and plastic properties of alumina and garnet phase.

activity is observed in Al_2O_3 lamella. The garnet phase was dislocation free, even at very high deformation loads (Fig. 11). Coarsening occurred during creep tests at temperatures above 1500°C (Fig.

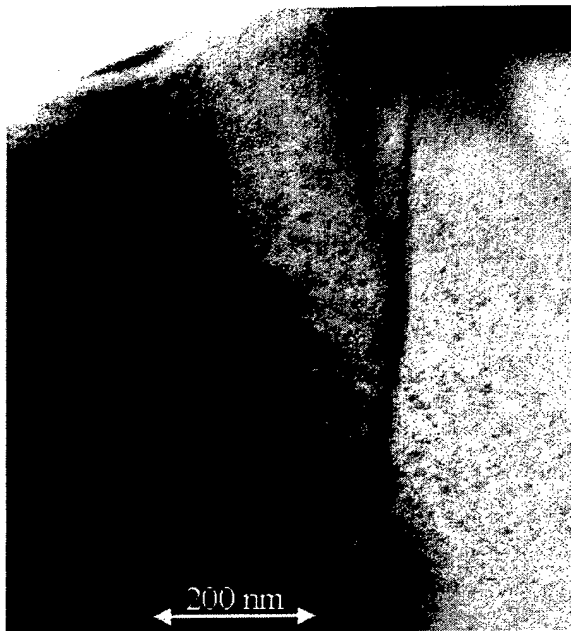


Fig. 11. TEM micrograph of a region close to the fracture of a sample crept at 1400° C. A few scattered dislocations were found in alumina and none in garnet. Exhaustive TEM examination of crept samples at other temperatures resulted in similar observations.

12). The aspect ratios of the phases are dramatically reduced and the microstructure was equiaxed after thermal treatments of 1.5 h at 1650° C.

3.4. Strain recovery

Creep experiments show a very intriguing history-dependent behavior. After load increment and subsequent reduction of stress, the strain rates are lower than initially experienced at the same load (Fig. 6). If the previous load increment is large enough, one observes a transient regime that may last several hours during which contraction of the sample occurs (see last load decrement in Fig. 6). Specific experiments to confirm and further examine the extent of strain recovery were conducted (recovery creep has been reported in similar systems [21]). For example in an experiment, the initial deformation for 8 minutes at 510 MPa produced a total elongation of approximately 70 μm (0.1% strain). The load was subsequently decreased to a very low stress (15 MPa) at the

same temperature. After 16 h a recovery of approximately 50% of the creep elongation was observed. The strain recovery is clearly not elastic, but rather is associated with the release of constraints built up during creep. This phenomenon is under further study.

4. Discussion

4.1. Effect of load transfer on the creep behavior

The TEM observations indicate that the interfaces are well bonded (Fig. 3). This type of interface is typical of directionally solidified ceramic eutectics [1, 3, 13]. Both components have fine phase spacing and form a highly interconnected microstructure. Due to the isostrain condition imposed by the well-bonded nature of the interfaces and the different plastic and elastic properties of the two materials involved, load transfer occurs between the two phases during deformation. The challenge is then to explain the seemingly complex material response of directionally solidified eutectics and to highlight insights gained for this class of materials. To address this, we will first discuss the mechanical response of the $\text{Al}_2\text{O}_3/\text{Er}_3\text{Al}_5\text{O}_{12}$ eutectic within three different behavior regimes as defined by their observed response to load at elevated temperatures.

The three regions can be described as (Fig. 13):

- I. Both components are elastic. Alumina will carry more load due to its higher elastic modulus. This region is obtained instantaneously in a constant load experiment.
- II. Alumina reaches its plastic yield point and garnet is still deforming elastically. The stress must increase continuously in the garnet phase to attain a particular strain rate. There is then a load transfer from alumina to garnet.
- III. Both phases are deforming plastically. The stress is redistributed to fulfill the isostrain condition.

The load transfer of region II can be easily modeled. The strains of alumina and garnet in this region follow the relations,

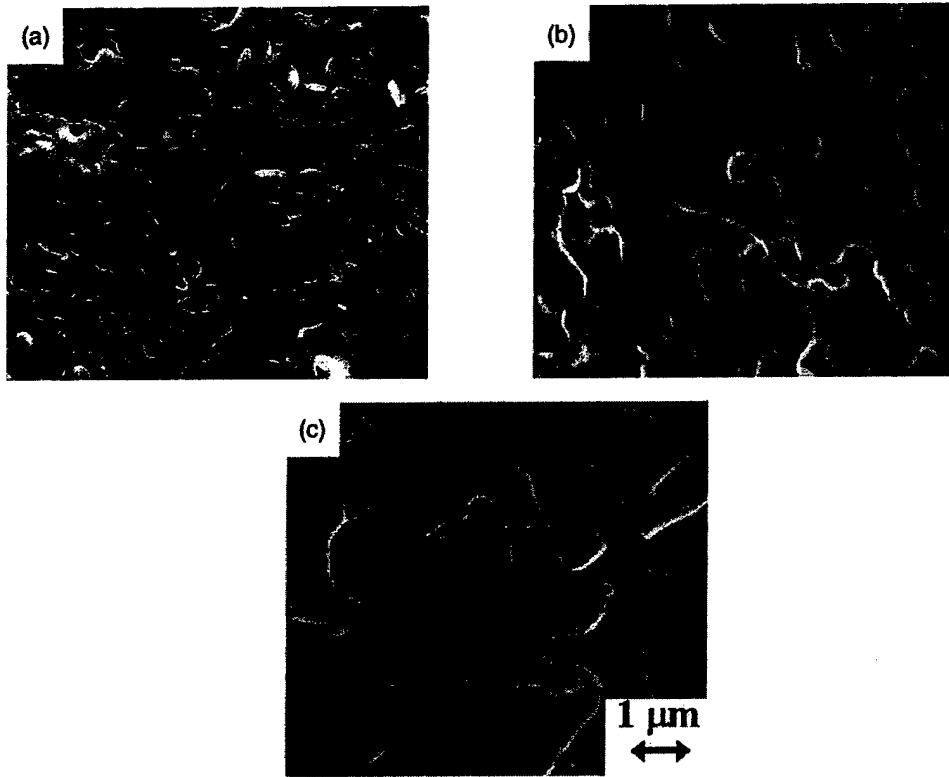


Fig. 12. SEM micrographs showing the microstructure after annealing. (A) 290 hours at 1400° C, (B) 3 hours at 1550° C, and (C) 1.5 hours at 1650° C. Microstructural coarsening is not detected at 1400° C even for very long annealing times. Over 1550° C coarsening of the microstructure is clear. All the micrographs are shown at the same scale.

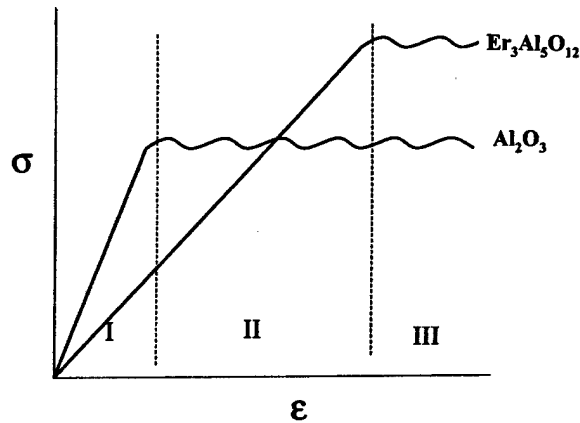


Fig. 13. Hypothetical stress-strain curve indicating the three stages of deformation discussed: Stage I, where both components are elastic, stage II, with alumina deforming plastically and garnet phase elastically, and stage III, where both components are deforming plastically.

$$\dot{\epsilon}_a = A_a \sigma_a^n; \dot{\epsilon}_g = E_g^{-1} \dot{\sigma}_g + A_g \sigma_g^n, \quad (1)$$

where $\dot{\epsilon}$ is the strain rate, σ the stress, E is the elastic modulus, and A the parameter relating the creep rate to the stress. The subscripts "a" and "g" refer to alumina and garnet. A typical power dependence of the strain rate with stress is assumed. In addition to the elastic component of the strain in garnet ($\epsilon_g = E_g^{-1} \sigma_g$), the contribution of a time dependent plastic strain is also included.

The isostrain condition requires the evolution of load transfer with time,

$$\dot{\epsilon}_a = \dot{\epsilon}_g \Rightarrow A_a \sigma_a^n = E_g^{-1} \dot{\sigma}_g + A_g \sigma_g^n, \quad (2)$$

$$\dot{\sigma} = \sigma_a V_a + \sigma_g V_g, \quad (3)$$

where $\dot{\sigma}$ is the average stress, V_a and V_g are the volume fraction of alumina and garnet, respectively.

The stresses in alumina and garnet then follow

the time dependence of $n=1$ based on the assumption that both single crystals deform by diffusional creep:

$$\sigma_g = \frac{\dot{\sigma}}{V_g + V_a \frac{A_g}{A_a}} \left(\frac{\dot{\sigma}}{V_g + V_a \frac{A_g}{A_a}} - \sigma_{g0} \right) \exp \left(-E_g \left(A_a \frac{V_g}{V_a} + A_g \right) t \right), \quad (4)$$

$$\sigma_a = \frac{\dot{\sigma}}{V_a} \left(1 - \frac{1}{1 + \frac{V_a A_g}{V_g A_a}} \right) - \frac{V_g}{V_a} \left(\frac{\dot{\sigma}}{V_g + V_a \frac{A_g}{A_a}} - \sigma_{g0} \right) \exp \left(-E_g \left(A_a \frac{V_g}{V_a} + A_g \right) t \right),$$

where the σ_{g0} is the stress at the beginning of region II in garnet.

Garnet is about two orders of magnitude more creep resistant than alumina at the temperatures of the tests [17], so it is plausible to neglect the effect of plastic deformation of garnet while this phase is still deforming elastically during region II. Equation (4) can then be written as,

$$\sigma_g = \frac{\dot{\sigma}}{V_g} - \left(\frac{\dot{\sigma}}{V_g} - \sigma_{g0} \right) \exp \left(\frac{-A_a V_g E_g t}{V_a} \right) \xrightarrow{t \rightarrow \infty} \frac{\dot{\sigma}}{V_g}, \sigma_a \quad (5)$$

$$= \sigma_{a0} \exp \left(\frac{-A_a V_g E_g t}{V_a} \right) \xrightarrow{t \rightarrow \infty} 0,$$

where the σ_{a0} is the stress at the beginning of region II in alumina. There is a stress transfer from alumina to garnet during region II that will depend on their relative elastic and plastic properties.

Two situations may arise depending on the magnitude of external stresses and the minimum stress to produce a measurable strain rate in the garnet phase ($\sigma_{\min \text{ garnet}}$):

(A) If $(\dot{\sigma}/V_g) < \sigma_{\min \text{ garnet}}$, during the load transfer there is a decrease of the strain rate until it

goes under measurable values and plastic deformation will apparently stop.

(B) If $(\dot{\sigma}/V_g) > \sigma_{\min \text{ garnet}}$, both phases will deform plastically after the load transfer. The system could enter a quasi-steady-state regime if the microstructure were stable during deformation.

An estimation of the minimum stress to produce a measurable strain rate in $\text{Er}_3\text{Al}_5\text{O}_{12}$ can be obtained from the YAG single crystal data available in the literature [17]. The stresses necessary to achieve a strain rate of $5 \times 10^{-10} \text{ s}^{-1}$ for YAG are 240 and 130 MPa for temperatures of 1400° C and 1550° C, respectively. Based on the volume fraction of the YAG phase, the corresponding average stresses are 144 and 78 MPa. These stress levels were obtained by extrapolating the available creep data for [110] compression [17]. If the stresses are calculated for an average orientation, using the creep data for [100], [110], and [111] loading directions, only a variation of 5% (depending on temperature) is obtained because there is little anisotropy of the plastic behavior.

The strain-time behavior of region II can be expressed by:

$$\varepsilon_{\text{system}} = \varepsilon_g = \frac{\sigma_g}{E_g}. \quad (6)$$

Figure 14 shows a typical transient regime at low stresses where the effect of the load transfer on the creep curve is more evident because the contribution of plasticity on garnet is negligible: 105 MPa at 1400° C. The best fit using equations (5) and (6) is also plotted ($R^2=0.960$) using the elastic modulus of $\text{Y}_3\text{Al}_5\text{O}_{12}$ garnet; 300 GPa [17] with the volume fraction $V_g=0.6$. This is a reasonable assumption since the elastic moduli of single crystal oxides does not differ within a family of crystal structures [22].

The calculated data from Fig. 14 for the initial stress in garnet phase (σ_{g0}) is 62 MPa with $A_g=6.17 \times 10^{-7} \text{ s}^{-1} \text{ GPa}^{-1}$. The values of E_g and σ_{g0} give compatible strains for regions I and II. The initial stress in garnet obtained from the fit is close to the stress redistribution that would be expected after region I, attributable to the differences in elastic modulus of sapphire and garnet ($E_{\text{sapphire}}=450$

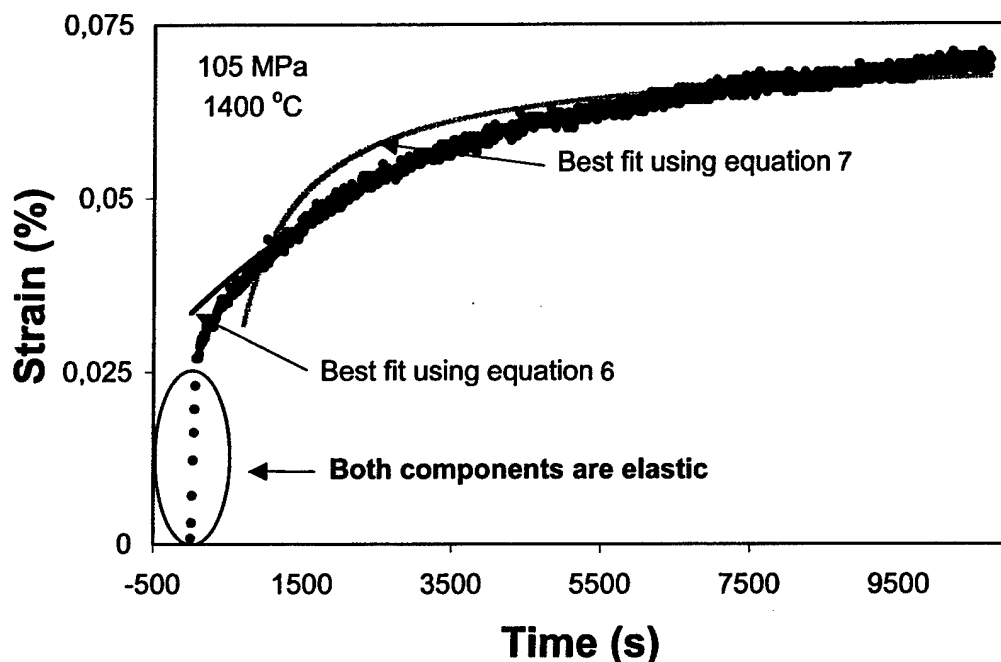


Fig. 14. Typical transient regime at low stresses where the effects of the load transfer on the creep curve are more evident as the contribution of plasticity of the garnet phase is negligible (105 MPa, 1400° C). Note that the best fit using equation (5) ($R^2=0.960$) lies within the scatter of the data for most of the strain. The best fit using equation (7) (assuming $n>1$, $R^2=0.804$) is also included. The good fit of equation (5) supports the hypothesis of load transfer and diffusional creep of alumina.

GPa) [13]. This distribution of stresses corresponds to the beginning of region II. The alumina creep constant (A_a) deduced from the fit gives reasonable values for the creep rates ($6.17 \cdot 10^{-8} \text{ s}^{-1}$ at 100 MPa and 1400° C) compared with the experimental quasi-steady-state creep rates. Yet, these values are lower than those obtained for diffusion controlled creep in polycrystalline alumina [23]. This is not surprising since the deformation of polycrystalline alumina includes a contribution from grain boundary sliding that is not viable as a mode of deformation in the directionally solidified eutectic system. This is the characteristic of the directionally solidified eutectic ceramics with unique interphase interfaces that is dissimilar from the grain boundaries of polycrystalline materials and requires further discussion (Section 4.2).

If the alumina phase is deforming with a stress exponent larger than one in region II, the expected

evolution of strain with time would follow an equation of the form:

$$\varepsilon = \alpha - (\beta + \gamma t)^{1/(1-n)}, \quad (7)$$

where α , β , and γ are constants which depend on E_g , σ_{g0} , A_g and V_g .

The best fit obtained with equation (7) gave $n=2.19$ and $R^2=0.804$ (Fig. 14). Under the assumption of $n>1$, the stress exponent obtained is still fairly low. Hence, a better description of the strain-time dependence is obtained assuming that alumina deforms by diffusional creep. The diffusional nature of the deformation in relation to the lack of dislocation activity is further discussed.

Further understanding of the proposed model load transfer model was obtained by stress relaxation experiments. The recovery of creep strain after unloading is caused by the release of elastic stresses built up in the garnet phase during defor-

mation. The elastic stress is expected to cause contraction in the alumina and to recover part of the creep strain after removal of the applied external stress. The load transfer model can also provide an equation for strain recovery by changing the integration limits:

$$\begin{aligned}\dot{\epsilon}_a &= \dot{\epsilon}_g \Rightarrow A_a \sigma_a = E_g^{-1} \dot{\sigma}_g, \sigma_a = \sigma_g, \\ \epsilon &= \epsilon_0 \exp(-A_a E_g t),\end{aligned}\quad (8)$$

where ϵ_0 is the strain that is not recovered instantly. The best fit gives a product of $A_a E_g = 10^{-4} \text{ s}^{-1}$. The calculated value of A_a is $3.33 \times 10^{-7} \text{ GPa s}^{-1}$, which is in good agreement with the value previously calculated for the transients following loading. Due to the complexity of the microstructure, garnet may have undergone permanent deformation in some regions, which could then be responsible for the creep strain that is not recoverable. Some additional recovery may be obtained in longer experiments.

4.2. Comparison with the classical deformation models

The deformation mechanisms, which could be operating in the two-phase system under isostrain deformation conditions, can be classified in two categories: (a) diffusion controlled mechanisms and (b) dislocation controlled mechanisms.

4.2.1. (a) Diffusion mechanisms

Nix [24] derived an expression for the case of creep by bulk diffusion (Nabarro–Herring creep) including the effect of the aspect ratio of the grains:

$$\begin{aligned}\dot{\epsilon}_{\text{diffusion}} &= \frac{21}{d_{\text{effective}}^2} \left\{ \frac{(R_1 R_2)^{-2/3} (R_1^2 + R_2^2)}{1 + R_1^2 + R_2^2} \right\} \\ &\quad \frac{\Omega}{kT} \left\{ D_0 \exp\left(\frac{-Q}{kT}\right) \right\} \sigma, \\ R_1 &= \frac{W_1}{L}, R_2 = \frac{W_2}{L}, d_{\text{eff}} = (W_1 W_2 L)^{1/3},\end{aligned}\quad (9)$$

where Q is the activation energy for diffusion, W_1 , W_2 , and L are the dimensions of the grains in the two directions perpendicular to and in the direction parallel to the applied stress.

In Fig. 15 the creep rates expected from this model at 1500° C are plotted together with the experimental data at the same temperature. Both alumina and garnet are assumed to creep by lattice diffusion, $W_g = 0.46 \text{ } \mu\text{m}$, $W_a = 0.31 \text{ } \mu\text{m}$, and the aspect ratio is 10. There is a lack of data on cation diffusion for garnet (only anion diffusion data is available [25]). Therefore the cation diffusion coefficient was calculated from creep data on polycrystals [26], where creep has been proven to be controlled by bulk diffusion. The same approach was adopted for the diffusion coefficient measurements of alumina [23]. The distribution of stress between the two phases was calculated at each external stress to fulfill the isostrain condition.

The strain rate expected from this model is higher than the experimental ones. This could be due to several different factors:

- 1 *Overestimation of the diffusion data.* The diffusion data calculated from creep experiments in polycrystals has been reported to give high values. For example the oxygen diffusion coefficient calculated from creep data in alumina [23] is over three orders of magnitude higher than the values obtained from direct measurements [27]. If the same discrepancy were assumed to exist between the cation diffusion (the lowest diffusing species) and diffusion data calculated from creep data in garnet [25], the simulated and experimental values would be in much closer agreement (Fig. 15).
- 2 *There is no sliding at the interfaces.* Diffusion creep is strongly coupled with grain boundary sliding, as diffusion creep creates deformation of the grains that must be accommodated. Accommodation by sliding at interfaces is not occurring during deformation in the $\text{Al}_2\text{O}_3/\text{Er}_3\text{Al}_5\text{O}_{12}$ system. This creates a build up of stresses at the interfaces, and increasingly longer/less stress driven diffusion paths are necessary to cause deformation. The creep data from polycrystals used to calculate diffusion coefficients includes a component of the strain due to interfacial sliding that could contribute to the over estimation of the creep rate.
- 3 *The diffusion paths are longer.* The phases are tri-dimensionally interconnected. This intercon-

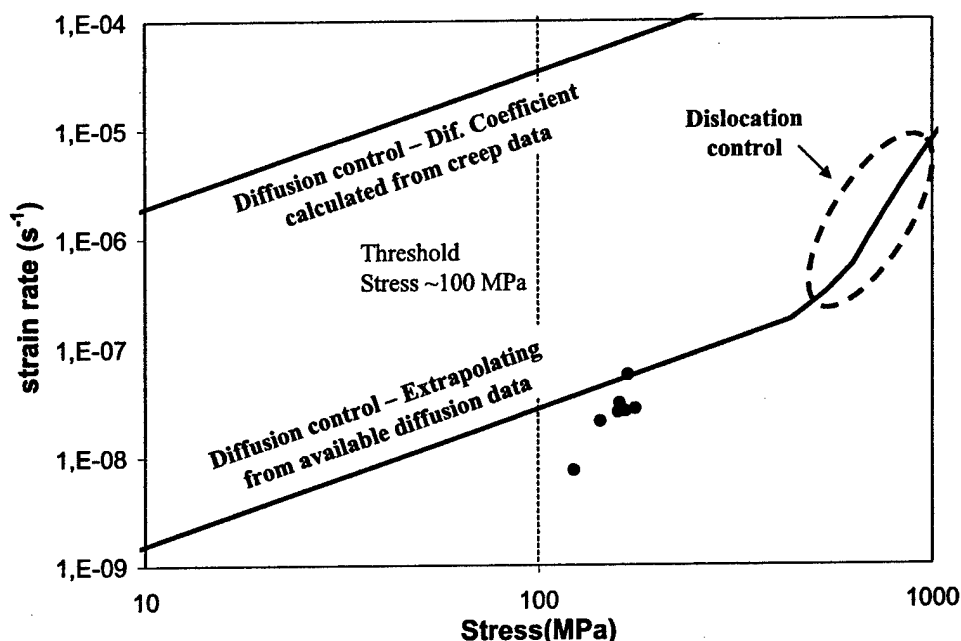


Fig. 15. Plot of the experimental (solid circles) and calculated creep rates at 1500° C considering diffusional creep (using diffusion coefficients obtained from creep on polycrystals and extrapolating the diffusion data available), and dislocation controlled creep. The regions where diffusional and dislocation plasticity dominate are indicated. Diffusion kinetics can explain the experimental creep rates. Dislocation plasticity dominates only at stresses well over the fracture stresses of this system.

nection leads to longer diffusion paths than the ones measured from the two dimensional cross-sections.

The microstructural evolution observed during the tests at temperatures over 1500° C is strong evidence supporting the importance of diffusion at the testing temperatures. The observed coarsening and longitudinal decrease of aspect ratio is driven by the decrease in interfacial energy. However, this coarsening indicates that the strains of the creep experiments could be easily caused by diffusion. Due to this microstructural evolution, detailed study of the creep curves was restricted to temperatures below 1500° C.

The high stress exponent observed could be explained by the existence of a threshold stress and by the non-stationary nature of creep within this system as will be discussed in Section 4.3. The activation energy for creep is compatible with the activation energies of diffusion available for the different species in alumina and garnet that range from 300 to 700 kJ mol⁻¹ [25, 27].

Based on these observations, diffusion is a plausible explanation for the quasi-steady-state creep rates observed. It is consistent with the magnitude of creep, the calculated creep parameters, the microstructural observations, and the loading and unloading transients.

4.2.2. (b) Dislocation mechanisms

The stress necessary to drive a dislocation across the interfaces is at least two orders of magnitude higher than the resolved stresses applied in the tests [14]. The dislocations must then move within one of the two components, thus they must bow within the phase spacing (λ). The stress necessary for this process is [28]:

$$\tau = \frac{Gb}{\lambda}, \quad (10)$$

where G is the shear modulus, and b the Burger's vector. We will consider that $\text{Er}_3\text{Al}_5\text{O}_{12}$ has similar properties to $\text{Y}_3\text{Al}_5\text{O}_{12}$ (elastic shear modulus at 1500° C of 110 GPa, and Burgers vector $\langle 111 \rangle = 1.04$ nm) [17]. For Al_2O_3 , a Burger's vector

of 0.512 nm and an elastic shear modulus at 1500°C of 133 GPa were used [17]. The nominal phase spacing ranges from 0.1 to 1 μm . The stresses necessary to bow the dislocations through the smallest spacing are then 1 GPa for $\text{Er}_3\text{Al}_5\text{O}_{12}$ and 0.7 GPa for Al_2O_3 . This calculation suggests that dislocation glide in $\text{Er}_3\text{Al}_5\text{O}_{12}$ is seriously limited as the stress necessary for dislocation bowing within the phase spacing s is of the same order of magnitude as the applied stress. The stress calculated from equation (10) would be the threshold stress for dislocation-controlled plasticity.

The behavior expected under the assumption that dislocation mechanisms are active can be calculated using literature data on sapphire and YAG [17] single crystals. Sapphire creep data is available for c-axis and 42° off axis orientations [6]. The TEM observations showed that the c-axis of alumina is not perfectly parallel to the specimen axis; a linear interpolation was taken between these two sets of data assuming a misalignment of 10°. In the case of garnet, creep data for [110] compression [17] was used. The isostrain condition was imposed and threshold stresses were calculated from equation (10). The phase spacing of alumina and garnet was taken as 0.31 and 0.46 μm , respectively.

The calculated strain rates for dislocation plasticity are lower than the experimental ones. Figure 15 shows that dislocation plasticity would dominate only at stresses well over the fracture stresses for this system. The extensive TEM studies did not find significant dislocation densities. The isolated dislocations found (Fig. 11), are very different from the typical dislocation networks of crept single crystals. This experimental evidence supports the conclusion that dislocations do not play a significant role in deformation. The low density of dislocations also has been acknowledged in other works in similar systems [8, 29]. Even in systems with a larger phase spacing (approximately between 5 to 20 μm) very little dislocation activity is reported in constant strain rate tensile experiments [30]. The increase in phase spacing will increase the diffusion paths and decrease the stress necessary to bow dislocations.

4.3. Steady state creep or primary creep?

From the arguments put forth in the discussion above, un-accommodated diffusion appears to be the mechanism responsible for creep deformation under the experimental conditions. This mechanism will not yield a true steady state creep behavior because the strain caused by diffusion is not accommodated. Due to the strong bonding of these interfaces, boundary sliding does not occur. The $\text{Al}_2\text{O}_3/\text{Er}_3\text{Al}_5\text{O}_{12}$ system is deforming in a primary regime until damage at the interphase interfaces is created. Steady state creep terminology should only be used then as a phenomenological approach to describe the best creep resistance under certain conditions and to compare with the creep resistance of other materials.

The time dependence of strain in primary creep is usually described by [16],

$$\epsilon = At^{1/m}. \quad (11)$$

Figures 4 and 5 show creep curves for two external stresses together with their best fits using equation (11). The curves fit well with the time dependence of equation (11). The exponent m obtained ranges between 3 to 8. However, if we consider only the final part of the creep curve in Fig. 4 (low strain rates, small stress), a straight line can also give a reasonably good fit. It is then difficult to determine from the final portion of the curve, which fit is better as the strain to failure is small. For example, if the $\text{Al}_2\text{O}_3/\text{Er}_3\text{Al}_5\text{O}_{12}$ system is deforming at $1.1 \times 10^{-8} \text{ s}^{-1}$ after 50 h and fails after 60 h, in these last 10 h, assuming a primary creep behavior with $m=5$, the strain rate would decrease to $1.06 \times 10^{-8} \text{ s}^{-1}$. This decrease in strain rate would be difficult to measure. The continuous decrease in strain rate is better observed in high strain rate experiments (Fig. 5), supporting the idea that the system remains in the primary creep region. Previous work on alumina-YAG also acknowledges this lack of steady-state creep [8]. These authors report a continuous decrease of strain rate down to a minimum, and then an increase of strain rate to failure. The minimum creep rate during the tests is taken as the steady state creep [8].

The determination of the stress dependence of

the quasi-steady state creep rate must be carefully considered. The strain to initiate damage at the interfaces that will lead to failure depends more strongly on the degree of interlocking of the microstructure than on the applied load. A more interpenetrating microstructure requires greater sliding at the interfaces to accommodate diffusion. The applied load controls how fast the system reaches this critical strain for damage, so the time to failure will be shorter as we increase the load. If we fit the final portion of the curve with a straight line for two stresses, we will get an apparent stress exponent higher than the real stress dependence of the transient regime. The relation between these exponents can be calculated. The strain rate follows the equation:

$$\dot{\epsilon} = \frac{A}{m} \sigma^n t^{(1/m)-1}. \quad (12)$$

The strain to failure gives a relation between the times to failure at the two loads

$$\epsilon_{\text{damage}} = \epsilon_1 = \epsilon_2 \Rightarrow \left(\frac{\sigma_1}{\sigma_2} \right)^n = \left(\frac{t_2}{t_1} \right)^{1/m}. \quad (13)$$

The stress exponent from the linear fits prior to failure is:

$$\begin{aligned} n_{\text{apparent}} &= \frac{\log\left(\frac{\dot{\epsilon}_1}{\dot{\epsilon}_2}\right)}{\log\left(\frac{\sigma_1}{\sigma_2}\right)} \\ &= \frac{\log\left(\left(\frac{\sigma_1}{\sigma_2}\right)^n \left(\frac{t_1}{t_2}\right)^{(1/m)-1}\right)}{\log\left(\frac{\sigma_1}{\sigma_2}\right)}. \end{aligned} \quad (14)$$

Using equation (13):

$$n_{\text{apparent}} = mn. \quad (15)$$

A value of $m=5$ will give a stress exponent 5 times the real stress dependence of the microscopic deformation mechanism. The measured stress exponent from the strain rate prior to failure could only be equal to the real stress dependence if the times to failure are the same. This is not the case as the time to failure is much shorter for higher loads.

The experimental situation (Fig. 4) is far from ideal. The time exponent and pre-power constant of strain show considerable scatter. This is not surprising given the complexity of the microstructure. However, the main issues are clear: the evolution of strain with time follows a power law typical of transient creep, and the stress exponent determined from the strain rate prior to failure leads to an overestimation of strain values. In Figs 4 and 5 the values of the stress exponent comparing strain rates prior to failure ($n=7.3$) and comparing strain rates at the same time ($n=2.6$) are calculated.

The transient nature of creep in this system together with the existence of a threshold stress accounts for the high stress exponent measured (reported as high as 18 in the literature [8, 29]). These experimental values are so far from the values expected from the diffusion or dislocation models that they do not by themselves provide sufficient support for either. Additional evidence is needed.

5. Conclusions

The $\text{Al}_2\text{O}_3/\text{Er}_3\text{Al}_5\text{O}_{12}$ (19.5 mol% Er_2O_3) system grown by directional solidification produces a fine microstructure with a high density of well-bonded interfaces. This microstructure imposes an isostrain condition during elastic and plastic deformation. The different elastic and plastic properties of the two phases leads to a unique load transfer situation.

There is load transfer to the garnet phase while this phase is deforming elastically that causes a continuous decrease of creep rate. During this transient regime the garnet phase deforms elastically and alumina deforms plastically. Following the initial region, both phases will be deforming at the same rate which is the global deformation rate of the $\text{Al}_2\text{O}_3/\text{Er}_3\text{Al}_5\text{O}_{12}$ eutectic. The lack of dislocations within the deformed specimens, the coarsening of the microstructure, the activation energies for creep, and the detailed study of the transient creep during loading and unloading conditions, leads to the conclusion that creep deformation of $\text{Al}_2\text{O}_3/\text{Er}_3\text{Al}_5\text{O}_{12}$ eutectic is diffusion controlled. Sliding at the interfaces does not accommodate diffusion and the system deforms in a non-steady-

state regime. Non-steady-state deformation leads to over-estimation of the stress exponents. Damage induced by the stress built up at the interfaces initiates final failure.

The unloading of the $\text{Al}_2\text{O}_3/\text{Er}_3\text{Al}_5\text{O}_{12}$ system following a moderate amount of creep deformation, produces a unique strain recovery. The driving force for the stress recovery is the stress that builds up due to the elastic deformation of garnet phase while alumina phase is deforming plastically.

Acknowledgements

The authors would like to thank Dr G. Morscher for the discussions on recovery creep and transients, Dr J. Goldsby for his help setting up the creep rigs, and Mr Tom Sabo for the technical assistance on the monofilament fabrication. This research was funded by NASA cooperative agreement NCC3-850 and AFOSR Grant #F49620-00-1-0048. MCyT MAT2000-1533-C03-03 funded the research in Spain.

References

- [1] Sayir A, Matson LE. HITEMP, NASA CP-10082, 1991, 1:83.
- [2] Sayir A, Dickerson RM, Yun HM, Heidger S, Matson LE. HITEMP, NASA CP-10146, 1994, 1:74.
- [3] Farmer SC, Sayir A, Dickerson PO. *Mat Res Soc Proc* 1995;365:11.
- [4] Sayir A. Directional solidification of eutectic ceramics. In: Pechenik A, Kalia RK, Vashista P, editors. *Computer aided design of high-temperature materials*. Oxford University Press; 1999. p. 10-7.
- [5] Sayir A, Farmer SC. *Acta Mater* 2000;48:4691.
- [6] Sayir A, Farmer SC. *Mat Res Soc Proc* 1995;365:22.
- [7] Sayir A, Hurst JB, and Jones S. HITEMP, NASA CP-10039, 1989.
- [8] Matson LE, Hecht N. *J Europ Ceram Soc* 1999;19:2487.
- [9] Parthasarathy TA, Mah TH, Matson LE. *J Am Ceram Soc* 1993;76(1):29.
- [10] Pastor JY, Poza P, Llorca J, Ipeña JJ, Merino RI, Orera VM. *Mat Sci Engine A241* 2001;308(1-2):241.
- [11] Pitchford JE, Deleglise F, Berger MH, Bunsel AR, Clegg WJ. *Ceram Eng Sci Proc* 2001;22(3):415.
- [12] Farmer SC, Sayir A. *Engng Fract Mech* 2002;69:1015.
- [13] Sayir A, Farmer SC. Fracture characteristic of single crystal and eutectic fibers. In: Ellices M, Llorca J, editors. *Fiber fracture*. Elsevier Science; 2002. p. 10-9.
- [14] Martínez Fernández J, Sayir A. *Ceram Eng Sci Proc* 2001;22(3):421.
- [15] Wu P, Pelton AD. *J of Alloys and Compounds* 1992;179:259.
- [16] Poirier J. *Creep of crystals*. Cambridge University Press, 1985.
- [17] Corman GS. *Ceram Eng Sci Proc* 1991;12(9-10):1745.
- [18] Garboraud RJ. *Phil Mag, A* 1981;44(3):561.
- [19] Clauer AH, Wilcox BA. *J Am Ceram Soc* 1976;59(3-4):89.
- [20] Gómez García D, Martínez Fernández J, Domínguez Rodríguez A, Castaing J. *J Am Ceram Soc* 1997;80:1668.
- [21] Morscher GN, Farmer S, Sayir A. *Ceram Eng Sci Proc* 1995;16(5):959.
- [22] Nye JF. *Physical properties of crystals*. Oxford Science Publications, 1985.
- [23] Heuer AH, Cannon RM, Tighe NJ. Plastic deformation in fine grain ceramics. In: Burke JJ, Reed NL, Weiss V, editors. *Ultra-fine grain ceramics*. Syracuse University Press; 1970. p. 33-9.
- [24] Nix WD. *Metals Forum* 1981;4(1-2):38.
- [25] Sakaguchi I, Haneda H, Tanaka J. *J Am Ceram Soc* 1996;79(6):1627.
- [26] Parthasarathy TA, Mah TH, Keller K. *J Am Ceram Soc* 1992;75(7):1756.
- [27] Cawley JD, Halloran JW, Cooper AR. *J Am Ceram Soc* 1991;74(9):2086.
- [28] Hirth JP, Lothe J. *Theory of dislocations*. John Wiley and Sons, 1982.
- [29] Deleglise F. Ph.D. Thesis. Centre des Materiaux, Ecole des Mines de Paris, France, 2000.
- [30] Waku Y, Sakuma T. *J Europ Ceram Soc* 2000;20(10):1453.



PERGAMON

Engineering Fracture Mechanics 69 (2002) 1015–1024

www.elsevier.com/locate/engfracmech

Engineering Fracture Mechanics

Tensile strength and microstructure of $\text{Al}_2\text{O}_3\text{--ZrO}_2$ hypo-eutectic fibers

S.C. Farmer ^{*}, A. Sayir ¹

^{*} *Nasa Glenn Research Center, 21000 Brookpark Road, MIS 106-5, Cleveland, OH 44135, USA*

Abstract

$\text{Al}_2\text{O}_3\text{--ZrO}_2(\text{Y}_2\text{O}_3)$ eutectic materials possess good fracture strengths and creep resistance. Increased Al_2O_3 content is one means to further improve creep resistance. The objective of this study is to examine fracture strength of Al_2O_3 -rich (hypo-eutectic) compositions at varying Y_2O_3 contents. Fibers 160–220 μm in diameter with 68 m/o Al_2O_3 and 1.1–7.6 m/o Y_2O_3 (30.5 to 16 m/o ZrO_2) were directionally solidified at 0.11 mm/s using the laser-heated float-zone process. Defect populations increased in size and severity with higher Y_2O_3 contents. However, fibers maintained 1 GPa fracture strength in the presence of numerous pores and shrinkage cavities, which extend with crack-like morphology along the fiber axis. Published by Elsevier Science Ltd.

Keywords: Strength; Modulus; Al_2O_3 ; ZrO_2 ; Eutectic

1. Introduction

$\text{Al}_2\text{O}_3\text{--ZrO}_2$ eutectic strengths have been studied since the 1970's [1–13]. Directionally solidified oxide eutectics exhibit improved resistance to slow crack growth and excellent strength retention at high temperatures up to 1400 °C [11]. Materials studied typically contain Y_2O_3 to metastably retain the high temperature cubic and tetragonal polymorphs at room temperature. The $\text{ZrO}_2\text{--Y}_2\text{O}_3$ phase diagram [14] is given in Fig. 1. In practice, a ZrO_2 (10 m/o Y_2O_3) solid solution addition is sufficient to fully stabilize the cubic polymorph to room temperature. At lower Y_2O_3 content, ~ 3.5 m/o, the tetragonal polymorph is retained. The local transformation of the metastable tetragonal polymorph to the stable monoclinic form in the presence of a propagating crack provides a toughening effect that has been extensively studied. If no Y_2O_3 is added to the $\text{Al}_2\text{O}_3\text{--ZrO}_2$ eutectic, microcracking occurs on cooling from solidification temperatures due to the relatively large volume change (3–5%) which accompanies transformation of tetragonal ZrO_2 to monoclinic ZrO_2 .

Deformation studies of $\text{Al}_2\text{O}_3\text{--ZrO}_2(\text{Y}_2\text{O}_3)$ eutectics have been conducted on fibers of (60.8 m/o Al_2O_3 , 39.2 m/o ZrO_2 (9.5 m/o Y_2O_3)) materials [11]. $\text{Al}_2\text{O}_3\text{--ZrO}_2(\text{Y}_2\text{O}_3)$ eutectic material exhibit a minimum creep

^{*} Corresponding author. Fax: +1-216-433-5544.

E-mail address: serene.c.farmer@grc.nasa.gov (S.C. Farmer).

¹ Employed by: Case Western Reserve University, Cleveland, OH 44106, USA.

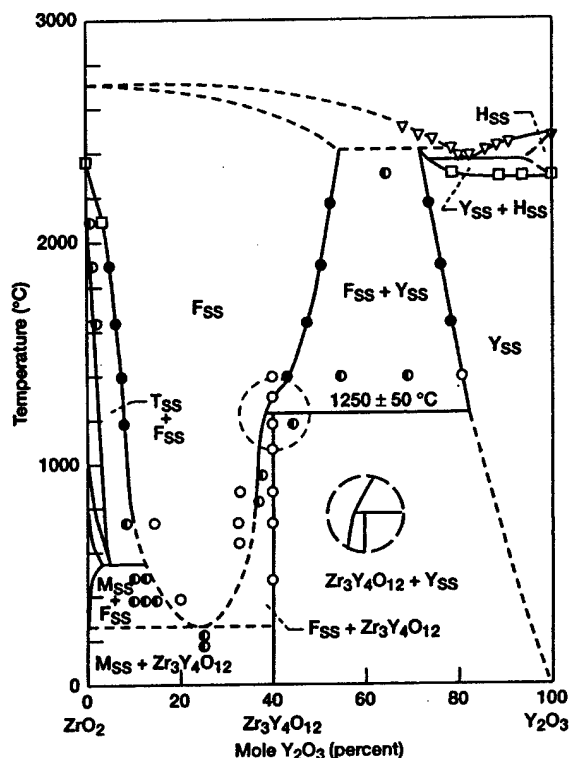


Fig. 1. Phase diagram for the system $\text{ZrO}_2\text{--Y}_2\text{O}_3$ (Ref. [14]). Solid solution phase fields for monoclinic (M_{ss}), tetragonal (T_{ss}) and cubic (F_{ss}) zirconia polytypes and the hexagonal (H_{ss}) and cubic (Y_{ss}) polytypes of yttria are shown.

rate of 10^{-9} s^{-1} under 50 MPa and 10^{-5} under 300 MPa load at 1400 °C. These values are better than the creep value expected for off-axis sapphire but substantially below c -axis Al_2O_3 creep values. Increasing the amount of Al_2O_3 , the more creep resistant phase, is one means to improve the high temperature creep resistance of $\text{Al}_2\text{O}_3\text{--ZrO}_2(\text{Y}_2\text{O}_3)$ eutectic materials. Mechanical properties are expected to be affected not only by the vol.% of Al_2O_3 but also by the ZrO_2 polymorph. The creep resistance of c - ZrO_2 at 1400 °C exhibits a twofold increase in flow stress with increase in solute content due to solid solution hardening [15]. Partially stabilized ZrO_2 (cubic plus tetragonal polymorphs) crept under similar conditions shows potent high temperature precipitation hardening [16]. The contributions of the phases, interphase interfaces and their spatial arrangement on the creep resistance is under investigation.

Substantial variations from the eutectic alumina to zirconia ratio can be tolerated without a loss in room temperature strength [2]. The purpose of this study is to examine the effect of increasing Y_2O_3 addition on the room temperature tensile strength of an $\text{Al}_2\text{O}_3\text{--ZrO}_2$ material containing excess Al_2O_3 . Results on mechanical properties and microstructures of these materials will be used to define compositions for creep testing in future work. $\text{Al}_2\text{O}_3\text{--ZrO}_2$ is of fundamental interest for creep studies as it combines a creep resistant material, Al_2O_3 , with a very low creep resistance material, ZrO_2 .

2. Experimental procedure

All materials were prepared from mixed powder composition of the base oxides. The powders are milled with binder and extruded to form a green rod. After drying, rods serve as source materials for fiber growth

using the laser-heating float-zone (LHFZ) facilities at NASA Glenn. The LHFZ systems scan a focused coherent CO₂-laser beam across a feed rod tip to produce a small molten zone. A *c*-axis Al₂O₃ fiber is used to seed growth. All materials were grown at a constant pull rate, 0.11 mm/s. This growth rate was selected as it produces a fully lamellar structure in 62 m/o Al₂O₃, 38 m/o ZrO₂ eutectic compositions. At this rate, fibers can be stably grown in LHFZ over a small range of temperatures, $\Delta T = 10\text{--}40^\circ\text{C}$, about the eutectic temperature. Growth temperatures at the lower limit were selected for this study. The materials fabricated had 68 m/o Al₂O₃ and Y₂O₃ contents of 0, 1.1, 3.2, 5.1 and 7.6 m/o Y₂O₃ with ZrO₂ as the remainder.

The tensile strength of LHFZ fibers was evaluated at room temperature using standard test procedures. Fibers 70 mm in length were mounted onto plastic tabs using epoxy. 5 mm pieces of a commercial fiber were affixed to the test fiber to serve as flags in measurement of the strain using a Zimmer 1071A optical extensometer. Flags were set at a 25 mm gage length and plotted results were used to indicate strain to failure and to calculate modulus. Data was taken using a table top Instron 4500/Series-IX with a sampling rate of 50 points/s. The crosshead speed was 0.02 mm/s and all tests were conducted at room temperature. Fiber diameters were measured using an optical microscope equipped with a Boeckeler marker measurement system. Microstructure and the few primary fracture origins which were retained, were examined using scanning electron microscopes.

3. Results and discussion

3.1. Modulus and fracture strength

The range of compositions studied was selected so that materials with distributions of both tetragonal ZrO₂ and cubic ZrO₂ could be examined [17]. The 68 m/o Al₂O₃ 32 m/o ZrO₂ composition is calculated to have ~77 vol.% Al₂O₃, a 10 vol.% increase relative to the 62 m/o Al₂O₃ (~67 vol.%) eutectic composition [18]. Adding Y₂O₃ affects both the ZrO₂ polymorph(s) and the phase content. Y₂O₃ is soluble in Al₂O₃ at the ppm level. Therefore the 1.1 m/o Y₂O₃ ternary corresponds to a 3.5 m/o ZrO₂(Y₂O₃) solid solution and is expected to be tetragonal. The 3.2 m/o Y₂O₃ materials, a 10 m/o ZrO₂(Y₂O₃) solid solution, are expected to be fully cubic ZrO₂. The 5.1 m/o Y₂O₃ composition lies adjacent to the boundary of the Al₂O₃ + ZrO₂ + Y₃Al₅O₁₂ ternary phase field [17] and some Y₃Al₅O₁₂ formation will occur. The 7.6 m/o Y₂O₃ composition lies well within the ternary field. Additionally, *x* moles of Y₂O₃ yield a 2*x* mole increase in ZrO₂ solid solution. So even with no Y₃Al₅O₁₂ formation, the vol.% of Al₂O₃ continuously decreases from its maximum value of 77%.

An example of a force vs. displacement curve obtained in this study is shown in Fig. 2. In a typical test, the diameter of the specimen retained after fracture is used to calculate the cross-sectional area and the fracture strength (GPa). The relative displacement of the two flags that define the test specimen gage length is used to calculate relative strain. Due to variation of the fiber diameter within the gage length, an average effective area was determined for plotting stress vs. strain. The elastic modulus is then estimated by curve fitting the slope of the stress-strain plot. To calculate an effective area, a series of optical photographs were taken over the gage length and digitized. Effective cross-sectional area, *A*, is then

$$A = \pi(A_p^2)/(4L_0^2) \quad (1)$$

where *A_p* is the projected area measured from the optical photographs and *L₀* is the gage length. Following this procedure the calculated elastic modulus for the five compositions is shown in Table 1.

The range in moduli, 270–370 GPa, is large and can be explained, at least in part, by considering the phase content and defects of the sample materials. The volume fraction of phases for the 1.1 m/o Y₂O₃ fiber is ~72% Al₂O₃ and ~28% ZrO₂. There is a large difference in elastic moduli between Al₂O₃ and ZrO₂.

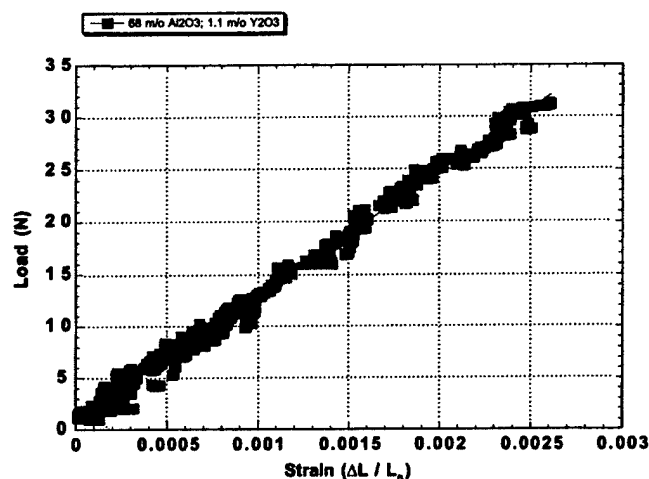
Fig. 2. Graph of load vs. strain data for fiber containing 1.1 m/o Y_2O_3 .

Table 1

Elastic modulus for 68 m/o Al_2O_3 materials with increasing Y_2O_3 additions estimated from the slope of stress–strain data plots

	No Y_2O_3	1.1 m/o Y_2O_3	3.2 m/o Y_2O_3	5.1 m/o Y_2O_3	7.6 m/o Y_2O_3
Elastic modulus (GPa)	270	370	320	290	310

Modulus values of 233 GPa $ZrO_2(Y_2O_3)$ for 5 and 14 m/o Y_2O_3 content crystals was determined by acoustic pulse-echo overlap technique [19] and 456 GPa for c -axis Al_2O_3 [20]. Using these values, the rule of mixture modulus for a parallel configuration is ~ 390 GPa. This is in reasonably good agreement with the 370 GPa value calculated for the 1.1 m/o Y_2O_3 fiber.

The material containing the maximum vol.% Al_2O_3 , 77 v/o, but no Y_2O_3 addition has the lowest elastic modulus. The low elastic modulus reflects the extensive microcracking that occurs on transformation of tetragonal ZrO_2 to the larger volume monoclinic polymorph. At 1.1 m/o Y_2O_3 , the ZrO_2 lamellae are stabilized against transformation on cooling and growth defects for this material are minimal. This material exhibited both the highest elastic modulus, 370, and best strength. As Y_2O_3 content is further increased, the vol.% of Al_2O_3 relative to the lower modulus ZrO_2 and $Y_3Al_5O_{12}$ phases decreases. In addition to decreasing the vol.% of Al_2O_3 relative to ZrO_2 , the Y_2O_3 has an undesirable effect on growth front conditions. The Y_2O_3 causes substantial constitutional supercooling of the melt, which impacts growth front morphology. In the 3.2 m/o Y_2O_3 and higher compositions, this leads to formation of crack-like shrinkage cavities, which further contribute to the decline in modulus.

Factors expected to effect eutectic strength are lamellar spacing, width of intercolony boundary regions and associated phases, voids and growth defects. The scale of these microstructural features extends over an order of magnitude. Interlamellar spacings are very fine, ~ 0.3 to ~ 0.2 μm while pores and shrinkage cavities are several microns in size in the highest Y_2O_3 content materials. The tensile strength data are given in the form of Weibull probability plots, Figs. 3 and 4. The single parameter Weibull probability, $\ln(\ln(1/\text{survival probability}))$, is plotted vs. $\ln(\text{fracture stress})$. Fig. 3 shows the test results for fibers with 68 m/o Al_2O_3 and 0–3.2 m/o Y_2O_3 . Mean strengths range from 0.74 for no Y_2O_3 additional to a maximum of 1.3 for the 1.1 m/o Y_2O_3 addition. Fracture strength of the strongest 1.1 m/o Y_2O_3 fibers is 1.9 GPa. Strengths decline with additional Y_2O_3 . The differences in the means of Fig. 3, although small, is significant at the 90 % confidence level. Significance was calculated using the Student t -test.

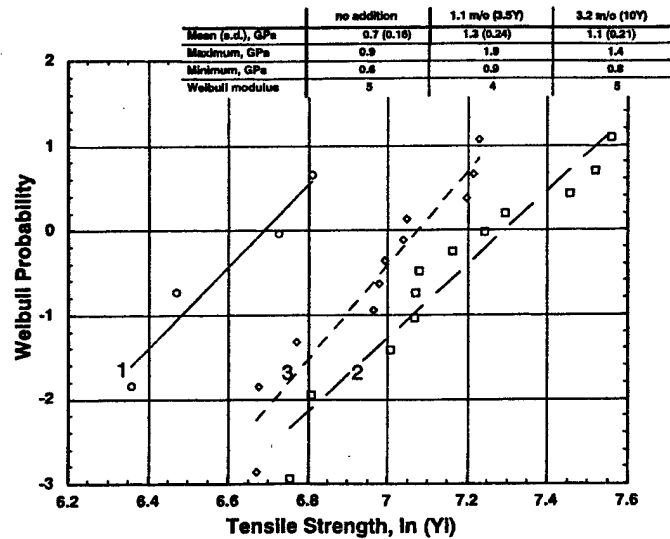


Fig. 3. Weibull probability plot of tensile strength for (1) 0 m/o, (2) 1.1 m/o and (3) 3.2 m/o Y_2O_3 compositions.

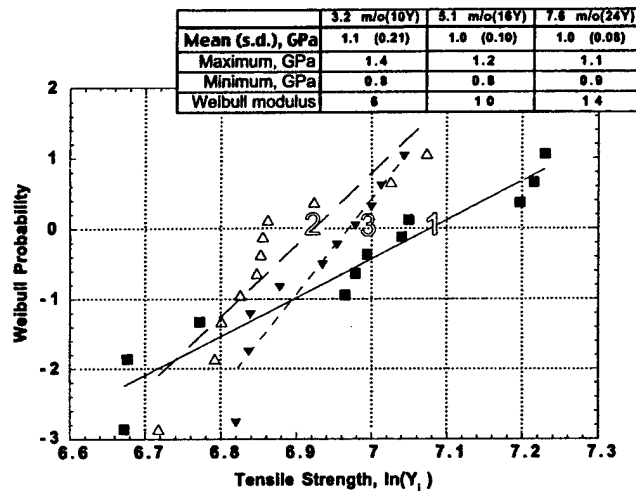


Fig. 4. Weibull probability plot of tensile strength for (1) 3.2 m/o, (2) 5.1 m/o and (3) 7.6 m/o Y_2O_3 compositions.

Strengths remain at ~ 1 GPa strength for 3.2–7.6 m/o Y_2O_3 materials, Fig. 4. Differences in the means for these compositions were not statistically significant at the 90% confidence level. Fiber containing 3.2 and 5.1 m/o Y_2O_3 were tested over a large diameter range (160–320 μm). Small diameters had the highest strength and large diameters the lowest as would be expected. For compositions with the highest Y_2O_3 contents (5.1 and 7.6 m/o Y_2O_3), there is a large increase in Weibull modulus. The highest Y_2O_3 fibers contain a population of large pores and shrinkage voids within the wide colony boundaries. The defects result from the solidification process as will be discussed in the following paragraphs. Even with an apparently large flaw population contributing to failure over a narrower range of strengths, the mean strength value remains ~ 1 GPa.

3.2. Effect of composition on microstructure

Microstructure of the five compositions will now be discussed in greater detail. Fracture strength as was mentioned above is correlated with processing conditions and hence the fracture characteristics of the fibers and their defects will be discussed from a processing perspective. At the 40 mm/h pull rate, fibers with no Y_2O_3 solidify with a lamellar microstructure. A distinct change in morphology occurs with added Y_2O_3 . The microstructure of the Al_2O_3 – ZrO_2 fibers of eutectic composition (62 m/o Al_2O_3 , 38 m/o ZrO_2 , 0 m/o Y_2O_3) are fully lamellar and solidifies without colony formation, Fig. 5a. The lamellar structure extends in regular fashion throughout the fiber cross-section. The hypoeutectic material (68 m/o Al_2O_3 , 32 m/o ZrO_2) of this study was also lamellar but less regular, Fig. 5b. Bands of coarser structure occur at intervals. This banding reflects the curvature at the growth front and delineates thermal isotherms. The excess Al_2O_3 is accommodated within these bands of coarser structure. No growth of primary Al_2O_3 was observed. Pores and crack-like features occur at the junction between bands. The microcracking associated with transformation to monoclinic ZrO_2 is not readily observed at this scale of observation. However, the low strength values, 0.6–0.9 GPa, and low elastic modulus are consistent with microcracking damage.

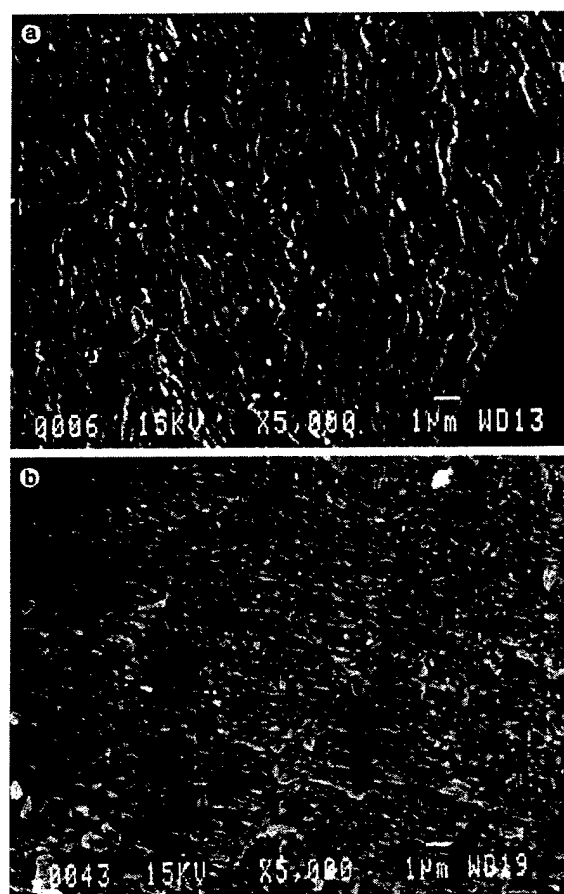


Fig. 5. (a) Fine lamellar microstructure of eutectic material, 62 m/o Al_2O_3 –38 m/o ZrO_2 and (b) banded lamellar microstructure of alumina rich material, 68 m/o Al_2O_3 –32 m/o ZrO_2 .

In materials containing Y_2O_3 , the melt becomes constitutionally supercooled and a planar growth front is not maintained during solidification. Colony growth results. The tendency for Y_2O_3 additions to undercool the melt have been previously reported in work of Borodin et al. [7]. Under conditions of large undercooling, the leading phase, Al_2O_3 , facets on the r -planes, $\{1-102\}$ and a transition from lamellar to a ZrO_2 rod morphology occurs. This represents a major change in the morphology (lamellae to rod) and distribution (axially aligned to inclined $\sim 55^\circ$ to the fiber axis) of the ZrO_2 phases. The fracture strength increases from 0.7 to greater than 1.0 GPa. The increase in strength is more strongly influenced by partial stabilization of the ZrO_2 than by the change in phase morphology and inclination as strengths greater than 1 GPa has been typical for variety of microstructures in both hypo- and hypereutectic Al_2O_3 - ZrO_2 (Y_2O_3) compositions.

Faceted colony growth is common to all Y_2O_3 compositions of this study. However the manner in which excess Al_2O_3 is accommodated differs. In the 1.1 m/o Y_2O_3 composition, excess Al_2O_3 is accommodated in Al_2O_3 -rich colony boundary regions and by formation of Al_2O_3 -rich facets on the fiber exterior in small diameter fibers. In large diameter fibers, solidification of a small number of primary Al_2O_3 dendrites occurs. Some distortion of the fibers is associated with the emergence and disappearance of Al_2O_3 facets. The formation of facets disrupts the balance of surface tensions at the liquid–solid–vapor triple junction. The molten zone shifts abruptly away from a central position and the fiber twists. Regions with one or two facets are separated by regions without facets. Fibers in which primary fracture surfaces were preserved fail from the center of the largest facet where the major facet is intersected by a smaller surface facet, Fig. 6. Larger diameter fibers, 200–300 μm , did not tend to facet. Instead, primary Al_2O_3 dendrites were common.

It is notable that the faceted and twisted fibers of the 1.1 m/o Y_2O_3 material, which experience a complex stress state on loading (tension and shear), proved to possess the highest strengths. The 1.1 m/o Y_2O_3 fibers are lamellar in the region near the fiber exterior with faceted colonies occurring only in the central portion of the fiber. There is minimal intercolony boundary width. Pores and ZrO_2 particles are located in the intercolony regions, Fig. 6b. There are no shrinkage voids. Fracture occurs in the Al_2O_3 phase relatively unaffected by ZrO_2 lamellae or rods. Some deflection does occur within the colony boundaries. Aside from the exterior alumina facets, these materials exhibit the smallest and least numerous growth defects and hence the greatest fracture strength.

At Y_2O_3 contents >1.1 mol%, no tendency for external alumina macro-facet development was observed. Materials however are highly supercooled and primary Al_2O_3 dendrites nucleate and grow in advance of the cooperative growth front. Al_2O_3 dendrites are arrowed in Fig. 7. The primary Al_2O_3 nucleates in a peripheral region near the fiber outer diameter where the temperature gradient is greatest. Therefore, dendrites are distributed in an annulus near the fiber periphery. At larger melt constitutional supercooling, the central portion of the faceted colonies extends a far greater distance into the melt. The intercolony regions, which are last to solidify, increase in thickness and contain irregular-shaped ZrO_2 particles. The intercolony boundary width increases in thickness. The size of ZrO_2 particles increases, Y_2O_3 -rich particles (presumably $Y_3Al_5O_{12}$) are present and in the 7.6 m/o Y_2O_3 material, solidify as an axially aligned continuous phase 3–10 μm in length within the intercolony region (Fig. 8). Pores increase in number and size and in 5.1 and 7.6 m/o Y_2O_3 compositions, shrinkage cavities are readily apparent.

Shrinkage cavities extend parallel to the fiber axis and are often referred to as shrinkage cracks due to their crack-like morphology. Shrinkage cavities develop as the increasing lag of the colony boundary regions from the advancing growth front sets up a condition where there is insufficient molten liquid flow to these last regions to solidify. The volumetric shrinkage on cooling then causes cavity formation. Yet, the effect of these defects are minimal. The shrinkage cavities are aligned roughly along the tensile axis and did not lead to a significant decrease in fiber tensile strength. It is noted however that the fibers with the shrinkage cavities also had larger irregularly shaped ZrO_2 particles and sharp edged pores. The number, severity, and perhaps interaction of these defects contribute to the higher Weibull modulus values and lower mean strengths.

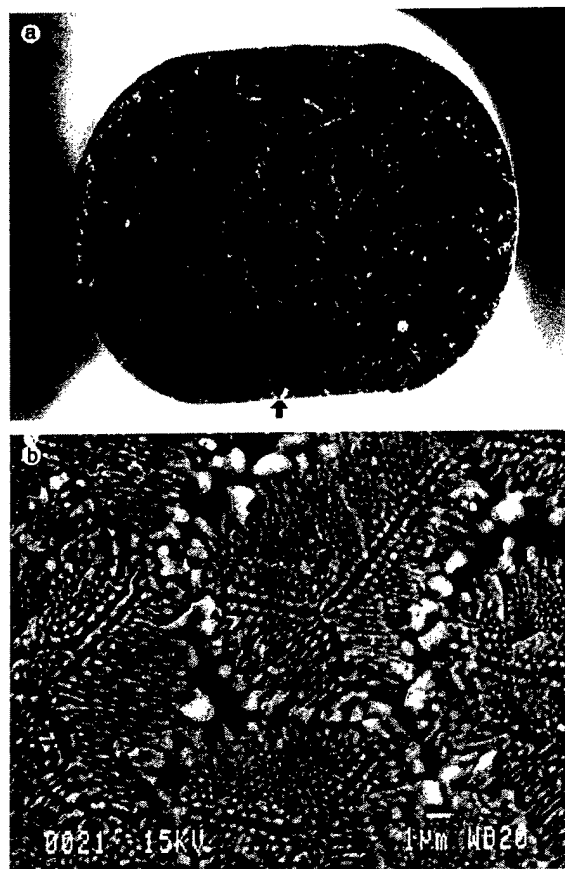


Fig. 6. (a) Primary fracture surface in 1.1 m/o Y_2O_3 material: Fracture initiates from surface at intersection of large facet (arrowed) with smaller surface facet and (b) primary fracture surface in central fiber region. Fracture occurs within Al_2O_3 with minimal deflection.

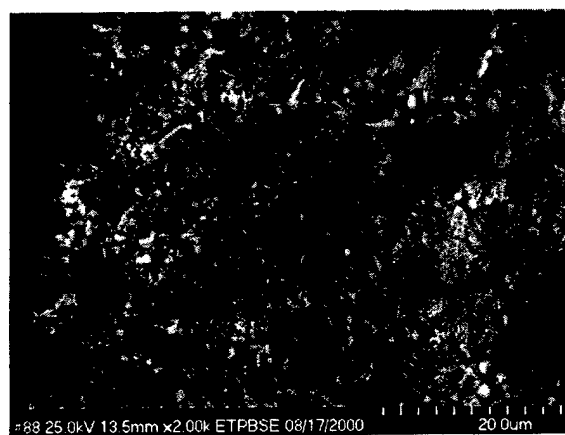


Fig. 7. Al_2O_3 dendrites occur near fiber perimeter identified by visible cleavage steps.



Fig. 8. 7.6 m/o Y_2O_3 material. $Y_3Al_5O_{12}$ solidifies within intercolony regions along with smaller (lighter contrast) ZrO_2 particles.

The fibers grown adjacent to or within the ternary phase field, compositions of 3.5, 5.1 and 7.6 m/o Y_2O_3 content, shows large amount of $Y_3Al_5O_{12}$ phase within the colony boundaries, specifically concentrated at the triple junctions between colonies Fig. 8. The composition in the series of area occupied by the colony boundary formation increase with increasing Y_2O_3 content as does the ZrO_2 particle size. The differences in fracture strength levels for these three compositions were not statistically significant. The primary fracture origins could not be unambiguously located because of the disintegration during the tensile testing. The differences observed in microstructure are incremental. Colony size decreases and intercolony area increases as Y_2O_3 increases. The amount of $Y_3Al_5O_{12}$ increases and the size and severity of pores and cavities increases.

It is surprising given the defect population that the mean fiber strength remains about 1 GPa. From our results, we infer that strength is most likely controlled by the lower toughness continuous Al_2O_3 phase. The coefficients of thermal expansion for Al_2O_3 and ZrO_2 differ substantially. Upon cooling, the Al_2O_3 phase is in tension and the ZrO_2 in compression. Average values have been determined by Pastor et al. [21]. At the large discontinuities between Al_2O_3 and ZrO_2 , such as shrinkage cavities, these residual forces are relaxed. These cavities which are aligned along the tensile axis are not strength controlling. Smaller pores contained wholly within the Al_2O_3 phase and large ZrO_2 particles located in the colony boundary regions are believed to act as critical defects. Although the presence of the discontinuous ZrO_2 and $Y_3Al_5O_{12}$ phase may impart increased toughness and greater defect tolerance, the residual tensile stresses in the lower toughness Al_2O_3 phase are thought to determine the fracture strength of these materials.

4. Conclusions

The study examined fracture strength of directionally solidified 68 m/o Al_2O_3 hypoeutectic compositions at varying Y_2O_3 contents. The Y_2O_3 content had a pronounced effect on the microstructure and fracture characteristics. Both the degree of supercooling caused by Y_2O_3 additions and the degree of solute rejection to the colony boundary regions were profound. This effect was underestimated in the design of this study. Hypoeutectic materials with Al_2O_3 contents intermediate between 68 m/o and the 62 m/o Al_2O_3 eutectic composition and with minimal Y_2O_3 contents will be pursued in further studies.

The Al_2O_3 – ZrO_2 (Y_2O_3) materials were highly tolerant of growth defects maintaining an average strength of 1 GPa in the presence of pores and large shrinkage cavities, which extend with crack-like morphology along the fiber axis. Critical defects were external facets, intercolony pores and other stress

concentrators contained within the low toughness Al_2O_3 phase that is in residual tension. Future studies will concentrate on strengthening the Al_2O_3 phase and increasing the amount of deflection experienced at the Al_2O_3 – ZrO_2 interfaces through use of dopants to achieve a combination of high strength and an acceptable toughness.

References

- [1] Schmid F, Viechnicki D. Oriented eutectic microstructures in the system $\text{Al}_2\text{O}_3/\text{ZrO}_2$. *J Mat Sci* 1970;5:470–3.
- [2] Cocks FH, Pollock JTA, Bailey JS. Preparation of in situ composites. Conf on In situ Composites, NMAB-308, vol. 1, 1973.
- [3] Hulse CO, Batt JA. Effects of eutectic microstructures on the mechanical properties of ceramic oxides, Report UARL N910803, 1974.
- [4] Ashbrook RL. *J Am Ceram Soc* 1976;60:428.
- [5] Mazerolles L, Michel D, Portier R. Microstructure and mechanical behaviour of Al_2O_3 – $\text{ZrO}_2(\text{Y}_2\text{O}_3)$ oriented eutectics. *J de Phys* 1986;47.
- [6] Mazerolles L, Michel D, Portier R. *J Am Ceram Soc* 1986;69:252.
- [7] Borodin VA, Starostin MYu, Yalovets TN. Structure and related mechanical properties of shaped eutectic Al_2O_3 – $\text{ZrO}_2(\text{Y}_2\text{O}_3)$ composites. *J Cryst Growth* 1990;104:148–53.
- [8] Bates HE. *Ceram Engng Sci Proc* 1992;13(7–8):190.
- [9] Courtright EL, Haggerty HS, Sigalovsky J. *Ceram Engng Sci Proc* 1993;14(7–8):671–81.
- [10] Farmer SC, Sayir A, Dickerson PO. Mechanical and microstructural characterization of directionally-solidified alumina–zirconia eutectic fibers. In: *In situ composites science and technology*. Warrendale: TMS; 1993 (167–82).
- [11] Sayir A, Farmer SC, Dickerson PO, Yun HM. High temperature mechanical properties of Al_2O_3 – $\text{ZrO}_2(\text{Y}_2\text{O}_3)$ fibers. In: *Proceedings of the Material Research Society Symposium*, vol. 365. Warrendale: MRS; 1995. p. 21–7.
- [12] Pena JJ, Merino RI, de la Fuente GF, Orera VM. *Adv Mater* 1996;8:909.
- [13] Pardo JA, Merino RI, Orera VM, Pena JJ, Gonzalez C, Pastor JY, Llorca L. Piezospectroscopic study of residual stresses in Al_2O_3 – ZrO_2 directionally solidified eutectics. *J Am Ceram Soc* 2000;83(11):2745–52.
- [14] Stubican VS, Hink RC, Ray SP. *J Am Ceram Soc* 1978;61:8–21.
- [15] Dominguez-Rodriguez A, Heuer AH, Castaing J. Dislocations and the mechanical properties of stabilized ZrO_2 . *Radiat Eff Defects Solids* 1991;119:569–759.
- [16] Dominguez-Rodriguez A, Lanteri V, Heuer AH. High temperature precipitation hardening of two-phase Y_2O_3 partially-stabilized ZrO_2 single crystals: a first report. *J Am Ceram Soc* 1986;69(3):285–7.
- [17] Lopato LM, Nazarenko LV, Gerasimiyuk GI, Shevchenko AV. Interaction in ZrO_2 – Y_2O_3 – Al_2O_3 system at 1650°C. *Inorg Matl* 1990;26(4):701–4.
- [18] Fischer GR, Manfredo LH, McNally RN, Doman RC. The eutectic and liquidus in the Al_2O_3 – ZrO_2 system. *J Mat Sci* 1981;16:3447–51.
- [19] Ingel RP, Lewis D, Bender BA, Rice RW. Physical microstructural and thermomechanical properties of ZrO_2 single crystals. In: Claussen N, Ruhle M, Heuer AH, editors. *Advances in ceramics*, vol. 12. Columbus, OH: American Ceramic Society Inc; 1984.
- [20] Tropsch WJ, Thomas M, Harris TJ. *Handbook of properties of crystals and glasses*. New York: McGraw-Hill; 1995.
- [21] Pastor JY, Poza P, Llorca J, Pena JJ, Merino RI, Orera VM. Mechanical properties of directionally-solidified Al_2O_3 – $\text{ZrO}_2(\text{Y}_2\text{O}_3)$ eutectics, in press.

TENSILE STRENGTH OF DIRECTIONALLY SOLIDIFIED CHROMIA-DOPED SAPPHIRE

J.J. Quispe-Cancapa, A.R. de Arellano-López, J. Martínez-Fernández
Departamento de Física de la Materia Condensada, Universidad de Sevilla

A. Sayir
NASA Glenn Research Center

Submitted to
Journal of the European Ceramic Society

May 2003

ABSTRACT

Tensile fracture properties of directionally solidified chromia-doped c-axis sapphire fibers have been studied in a range of temperature (room temperature up to 1400°C) and dopant content (0, 300 ppm and 1 % of Cr_2O_3). Delayed failure of the fibers was studied by measuring the dependence of the tensile strength on the loading rate and by fractographic studies on the fracture surfaces of the fibers. In all the temperature range, the fibers doped with 300 ppm of Cr_2O_3 are slightly stronger than the pure sapphire fibers. The least strong fibers are those containing 1 % of Cr_2O_3 . For this badge of material, the beneficial effect of solution hardening is counterweighted by increasing amount of defects caused by a faster fabrication. Slow crack growth appears to be the process controlling delayed failure at higher temperature. Little contribution of slow crack growth to delayed failure is found at the lower temperature.

Keywords

Sapphire, chromium oxide, tensile fracture, slow crack growth, fractography

1.- Introduction

Directional solidification (DS) fabrication methods are ideal for the obtention of ceramics with special compositions and microstructures. Ceramic single-crystal and eutectic fibers is one of the significant examples [1-8]. They can be fabricated systematically, even commercially, by DS with controlled composition, allowing important fundamental studies on the physical properties of materials.

Fibers are ideal for tensile fracture studies. With a relatively simple configuration numerous fibers can be tested, addressing the intrinsic statistical behavior of fracture [9], and a wide range of temperature can be covered.

In recent years, a systematic effort has focused on the study of the effect of dopants in fracture properties of sapphire ($\alpha\text{-Al}_2\text{O}_3$), using DS fibers [1-6,10]. The addition of dopants to sapphire is known to change structural properties [11,12], by the microscopic mechanisms of solution hardening [13]. Studies by H. Sayir et al. [3] showed that enhanced high temperature (HT) strength is obtained in MgO-doped sapphire, while the most efficient dopant at room temperature (RT) is Ti^{4+} . Extending a previous study by Heydt et al. [6], that measured a clear increase in tensile strength in 100-300 ppm Cr_2O_3 -doped sapphire at 1200 and 1400°C, our work intends to complete the understanding of the effect of the addition of Cr^{3+} to the tensile fracture of $\alpha\text{-Al}_2\text{O}_3$. The extension of the mentioned research follows two lines. First larger amount of dopant is used in a new badge of fibers, specially fabricated for this study. Second, the range of temperature covers from RT to 1400°C.

There exist several approached to the study of fracture. It is well known, for instance, that subcritical crack growth is a limitation to fracture strength

in ceramics [9,14]. The stable growth of flaws under applied stresses less than that for fast fracture (slow crack growth, SCG) is experimentally studied by considering the phenomenological equation:

$$v = AK_I^N \quad (1)$$

where v is the crack velocity, K_I is the stress intensity factor, and N is a constant. If N is bigger, the less likely is the material to undergo SCG [14].

When SCG is active, both static and dynamic fatigue are important in ceramics. Static fatigue causes delayed failure and also makes the strength dependent on the rate of increase of the stress on the material. The faster the stress is applied, the higher the strength is. Using this phenomenon, it is possible to calculate N by means of experiments in which the average strength is measured under different stressing rates [9,14]. The operant equation can be demonstrated to be [15]:

$$\sigma_f^{N+1} = B(N+1)\sigma_i^{N-2} \left(\frac{d\sigma}{dt} \right) \quad (2)$$

where σ_f is the fracture stress for a given stressing rate, σ_i is the instantaneous fracture stress, and B depends on the fracture toughness, K_{Ic} , and on geometrical aspects of the critical flaw. Equation 2 can be transformed to allow the determination of N :

$$\log(\sigma_f) = \left(\frac{1}{N+1} \right) \log \left(\frac{d\sigma}{dt} \right) + \log D \quad (3)$$

by plotting the failure stress vs. the stressing rate.

2.- Materials

All the materials for this study have been fabricated using directional solidification techniques. Chromia-doped sapphire (ruby) fibers were fabricated using a laser-heated floating-zone technique (LHFZ) which has been described elsewhere [6,15]. Compositions of the starting powders were 300 ppm and 10 wt.% $\text{Cr}_2\text{O}_3\text{-Al}_2\text{O}_3$ (sample designations NASA-L and NASA-H). Cr_2O_3 presents complete solubility in Al_2O_3 [15], however it is well known that chromium volatilizes at temperatures over 1000°C [17], an effect that has even been reported in certain conditions over 600°C [18], so actual compositions after fabrication and after the heating cycle in the mechanical testing are to be determined.

Additionally, highly-pure sapphire fibers were bought from Saphikon Inc. (Milford, NH). Saphikon fibers are fabricated by a micro-pull down technique [19]. In all cases, c-axis oriented crystals are used as seeds, so resulting fibers are well oriented in the c-axis [4,5,6]. Typical diameters of the fibers range from 110-140 μm (see Table I for details).

Fibers with low chromium content (NASA-L) were the subject of a previous study by Heydt et al [6,20]. Tensile rupture tests were run at both 1200°C and 1400°C , under constant strain rate. The composition of the as-fabricated and thermally cycled samples was detailed studied by secondary-ion mass-spectrometry (SIMS) and will be discussed below.

3.- Experimental procedure

3.1.- Mechanical tests

Mechanical experiments covered a wide range of temperature. Tensile rupture tests were performed at 25 (RT), 800, 1200 and 1400°C. The experimental setups for 25°C and for 1200 and 1400°C have been described previously [9,21,22]. In the first case fibers length is 2.5 cm. In the second, 15 cm fibers are need, but the hottest zone in the MoSi₂ furnace is only 2.5 cm long. For experiments at 800°C a MoSi₂ horizontal furnace was built and calibrated for this study. This setup uses 8 cm long fibers, and again the hottest furnace zone is 2.5 cm. Effective material volume equivalent for every condition. Experiments are only considered valid when fracture occurred in the 2.5 cm of reference, meaning less that 50% of the approximately 300 fibers that were broken in this study.

The fibers were tested under different loading rates with a device specially built and calibrated for this study. This device works by adding water to a container with a constant flow rate, ensuing a constant stressing rate. Available loading rates were 3.50×10^{-3} , 3.90×10^{-2} , 4.60×10^{-1} and 12.60 N.s^{-1} . The flow of water stops when the fiber breaks, and then the water in the container is weighted. This method allows the measurement of the tensile load of rupture with an error that can be assess to be about 1% for the slowest stressing rates and about 4.4% for the fastest, that was only used at room temperature. Typical heating and testing time is about 100 min.

3.2.- Microprobe analysis and fractography

Electron microprobe analysis was conducted in a Philips XL30 scanning electron microscope equipped with secondary (SE) and backscattered (BSE)

electron detectors and with a Si(Li) energy-dispersive x-ray (EDX) detector with an ultrathin window.

Semi-quantitative chemical analysis was conducted on the NASA-H samples, both as fabricated and subject to the testing thermal cycle, by EDX spectra using EDAX analytical software. Pure Al and pure Cr standards were used for quantification. Both the exterior and the interior of the fibers was analyzed. For studying sample inside, the fibers were epoxy-mounted and polished flat down to 1 μm using diamond paste. In all cases carbon was evaporated on the surfaces to make the samples conductive, with negligible effect on the spectra.

Fracture surfaces were extensively studied to identify the critical defect that originated the rupture, and also the characteristics of the crack growth. Fracture ends of the fibers were identified and saved for these fractography analysis. In the experiments run with the 15 cm fibers (higher temperature), elastic recoil after rupture was responsible for multiple fracture of the upper part of the fiber, making it impossible to identify the fracture surface. To avoid catastrophic recoil, fibers upper end was beaded [23] to hold the fiber to a syringe, that was then gripped for testing.

4.- Results

4.1.- Microprobe analysis

Chromium content of the different fibers are listed in Table I. Composition of Saphikon fibers is the advertised one. The composition of NASA-L fibers was measured by Heydt et al. [6,20]. NASA-H fiber composition was measured in this work.

Figure 1 shows representative EDX composition maps for Al, Cr and O, and an SE electron micrograph of the analyzed area for an as-fabricated NASA-H sample. Aluminum and oxygen are homogeneously distributed throughout the fiber section. Chromium, however, presents a larger concentration on the outside of the fiber, while the interior shows a lower and homogeneous concentration of the dopant.

The surface concentration of Cr in the as-fabricated samples is ~14.5 at%, with a large variation along the fiber. Interior Cr measurements correspond to spectral peaks well over the reference minimum detectable quantity (~0.1%), and present a small error bar. When the fibers are cycled up to 800°C, no significant change is found in the internal and external composition. The situation changes at 1200°C, in good agreement with the expected volatilization of chromium over 1000°C. On one hand the exterior of the fiber loses chromium down to half the values for lower cycle temperature, and on the other the interior gains some Cr, but the increase is still within the error bar. When cycled at 1400°C, the composition of the interior and the exterior of the fibers balances at 1.1%. Some of the Cr evaporates, but part of it may diffuse to the inside. Again, the composition of the fiber interior appears to be homogeneous.

Figure 2 shows additional Cr maps in sections cycled at different temperature. The corona of Cr concentration is lost at 1200°C, as the composition of the surface and inside of the fibers balances. The loss of Cr on the surface of the sample is also evident in the optical microscopy observations, included in the figure. As-fabricated fibers present a deep red color (darker gray in the picture), that is lost as the Cr of the surface volatilizes. All these features do not mean any change in the fiber morphology or diameter, as seen in the SE micrographs in figure 2.

As a general result, the interior of the NASA-H fibers contains ~ 1 at% of chromium for all the temperature interval. Effectively the range of fiber

compositions then covers 0 Cr% (Saphikon), ~ 300 Cr ppm (NASA-L) and ~ 1 Cr% (NASA-H).

4.2.- Mechanical tests

In mechanical experiments rupture stress, σ_r , is measured for different stressing rates, $\dot{\sigma}$. Rupture stress vs. stressing rate plots from our study, for different temperature and type of fibers are shown in figures 3, 4, 5 and 6, and the average values are listed in Table II, along with corresponding error bars. The listed results for NASA-L fibers at 1200 and 1400°C are taken from the previous work by Heydt et al. [6,20], that tested the fibers using a constant strain rate apparatus, and calculated the stressing rate assuming elastic conditions.

Fracture is an statistical phenomenon, that is dominated by the presence of critical defects [6], so it is typical to find large scatter in the rupture stress. Even under this consideration, several trends are evident. The tensile strength decreases systematically with temperature for every type of fiber. NASA-L fibers are the strongest ones at every temperature, but results are within the experimental error when compared to the Saphikon fibers. NASA-H fibers, with the largest Cr content, are the weakest, with a lost of strength near to 50% when compared to NASA-L fibers.

Additionally, an increase of the average tensile strength with stressing rate is evident, at every temperature. This means that a value of N can be calculated according to equation 3. When this value is large (> 40), then the slope of the σ_r vs $\dot{\sigma}$ curve is very flat, so more experiments are need for a better determination of N , with a wider interval of stressing rates, as seen in the table (10^{-1} to 10^3 MPa.s $^{-1}$, in orders of magnitude). Such is the case for the room temperature results (figure 3). At this temperature more experiments are possible because the testing technique uses smaller fibers.

As a general scope, N is larger at room temperature and 800°C than at 1200 and 1400°C. The N values are determined by linear regression when three data points are available. In all cases $R^2 > 0.90$.

4.3.- Fractography

Representative fracture surfaces of the fibers are shown in the micrographs of figures 7, 8, 9 and 10, for fibers broken at room temperature, 800, 1200 and 1400°C, under different stressing rates. In all cases fracture origin is a fiber defect, either internal or external. No difference on fracture surface features has been found to be correlated to stressing rate.

The qualitative features of fracture surfaces are typical, and are a result of changes in the crack growth velocity [9,24]. Micrographs in figures 9 and 10, corresponding to the higher temperature experiments, present all the significant characteristics: the fracture source is easily identified, and it is surrounded by a small region that is considered to be originated by the slow crack growth [4,24,25]. Micrographs in figure 11 show details of this type of feature generally found in NASA-H fibers broken at 1200 and 1400°C. Around it, a smooth mirror region is clearly seen. When the crack front is large enough, when high crack velocity has been reached, crack branching is evident [24,25], probably following sapphire crystallographic planes.

As the testing temperature decreases, the slow crack growth region disappears and the mirror region is smaller. This observation is clear in the micrographs in figures 6 and 7. In Saphikon fibers broken at room temperature, the mirror region is absent.

5.- Discussion

Some studies on strength of pure and doped sapphire are now classical [11,12,27]. The tensile strength results of sapphire-based fibers, with different dopants and compositions, are presented in figure 12. The results of this study, plotted for comparison in this graph, correspond to the fracture stress in the experiments using the slowest stressing rates, that are the lowest at each temperature, as presented in Table II. The results from other studies [3,4,5] correspond to different stressing rate conditions, not always specified. It is to be heard in mind, however, that even large changes in the stressing rates only cause small changes in average tensile strength, so qualitative comparison is possible.

The general trend of our results is parallel to that of other works, in terms of the reduction of strength with temperature. Results on Saphikon fibers is similar in the different studies at RT and at the highest temperature, but not in the intermediate range. At 800°C, for instance, Newcomb and Tressler [4] report a tensile strength higher than that reported by A. Sayir [5], and twice the value measured in this study. It will be shown below, that it is also in the range RT to 800°C where larger differences in the exponent N are found between different studies.

For similar dopant content of a few hundred parts per million, it is apparent that Cr is less effective than Mg and Ti as additive for improving strength. Sapphire doped with cations with ionic radius larger than Al^{3+} is expected to be stronger than pure sapphire due to the mechanism of solution hardening [13,28]. Larger ions cause a deformation of the network, and make the sliding of dislocations more difficult. An increasing size of the cations produce a larger deformation of the network, and eventually increasing strengths. Considering Mg, Ti and Cr, the expected result is: $\sigma_{Mg^{2+}} > \sigma_{Ti^{4+}} > \sigma_{Cr^{3+}}$ [11] which is the measured result at HT.

The classical model of solution hardening by a small concentration of discrete obstacles [28] establishes that the improved yield strength, σ , is:

$$\sigma \propto f^{3/2} c^{1/2} \quad (4)$$

where f is related to the energy barrier of each obstacle, then related to the cation size, and c is the dopant concentration. For small additions of dopant, the main effect on strength is related to the energy barrier to dislocation sliding imposed the solute.

Considering equation 4, increasing dopant concentration should result in bigger yield stress. This is not our observation, however. The addition of larger amounts of Cr, up to 1 at%, reduces strength in all the temperature range. Most likely explanation is the possibility of being the NASA-H fibers more imperfect than other formulations. To achieve larger Cr contents in the fibers, a more rapid laser-heating cycle is needed, which probably results in more internal cavities. This type of defects are always the origin of fracture in NASA-H fibers in the whole range of temperature. In Saphikon and NASA-L fibers both internal and external defects are detected to be fracture origin.

Previous studies [21,22] reported that RT Weibull modulus is about 4 for Saphikon and NASA-L and about 8 for NASA-H fibers, which would support the suggestion of a larger defect population in the NASA-H fibers. The evolution of Weibull modulus with temperature (800-1400°C range) in Saphikon fibers was studied by A. Sayir. He found an increase in the modulus from about 5 to about 18, with increasing temperature, and correlated the effect with an growing activity of SCG with temperature [5].

In the plots of figure 13, the results listed in Table II are compared with literature results. When these literature results are from constant strain rate experiments, the transformation to constant stressing rate is made

assuming a elastic behavior, with a representative $E_{[0001]}=335$ GPa. The dependence of this value with temperature is weak [9]. The results on the NASA-L fibers at 1200 and 1400°C are taken from the work of Heydt et al. [6]. Previous assertions on strength, now under different stressing rates, hold. A dependence of strength on stressing rate has been measured at every temperature, suggesting that static fatigue may be active. Such result, however, is indisputable only as temperature increases.

All the plots in figure 13 used the same scale in the axis, so the slopes are directly comparable. These slopes are more flat at RT than at 1200 or 1400°C, meaning a decrease in the value of N with temperature. In figure 14, the N values calculated in this study are plot vs. temperature, including some literature results [4,5]. Two regions are clearly distinguishable. From RT up to 1000°C, N is larger than 20. Results by different authors present a significant scatter, but N as high as 54 has been calculated in our study for NASA-H at RT. From 1100 up to 1500°C, the interval for N is in the range 10-20.

When combine with the fractographic observations, it is possible to suggest that SCG plays a role in the HT tensile strength of Cr-doped sapphire fibers, then explaining the observed dependence of the strength on the stressing rate. At lower temperature, N values are high, meaning a weak dependence of the strength on the stressing rate, and fracture surfaces do not present evidence of SCG. Static fatigue by SCG is then basically a HT phenomenon is DS sapphire-based fibers, confirming observations by several authors [3-6,12].

Several microscopic mechanisms have been claimed responsible for the SCG process, from which we consider four: stress corrosion [29], diffusive cavitation [30], dislocation assisted crack growth [31] and thermally activated bond rupture [32]. Microstructural observations that may support the activity of these mechanisms are quite difficult, when not impossible for

the characteristics of the samples, fibers in this case, so speculation may only rule out a mechanisms tentatively.

In the range of temperature for which SCG is active, the HT range, fracture origin is typically an internal defect, with some exceptions in some experiments on Saphikon fibers at 1400°C, so stress corrosion is unlikely to be the SCG mechanism. Pore diffusive-growth in crack-like manner is also quite unlikely in sapphire, given the shortness of the experiment, and the slow diffusivities of atomic species in Al_2O_3 . More detailed arguments can be found in the literature [4]. Dislocation-assisted mechanisms can be also ruled out. Given the orientation of the fibers, and the experimental conditions, if plastic deformation was important at the crack tips twinning should be observed [33]. Mirror surfaces are flat and smooth and no striations are observed in the exterior of the fibers.

The most plausible SCG mechanism is thermally activated bond rupture. Newcomb and Tressler [4] suggest the mechanisms of lattice trapping [32] for HT-SCG in Saphikon fibers, and provide several qualitative supporting features, both mechanical and microstructural. Among the last, the topography of the fracture surfaces is of most importance. The particular shape of the branching along crystallographic planes, which is dominated by the differences in crack propagation velocity through those planes, is predicted by the lattice trapping mechanisms.

6.- Conclusions

Directionally solidified pure sapphire and chromia-doped sapphire c-axis fibers, have been studied in tension from room temperature to high temperature under a range of stressing rates. NASA-L fibers are stronger than Saphikon fibers, and both stronger than NASA-H fibers. Solution hardening is suggested to be responsible for the increase of tensile strength

in the fibers with low dopant content, and internal defects are considered responsible of the reduction of tensile strength in the fibers with high dopant content. High-temperature static fatigue is found in all the fibers. Slow crack growth is the dominant process to explain the dependence of the tensile strength on the stressing rate. Thermally activated bond rupture is suggested to be the microscopic mechanism controlling HT-SCG in these sapphire-based fibers.

Acknowledgements

This research was funded at NASA by AFOSR Grant #F49620-00-1-0048, NASA NCC3-850 and in Spain by MCyT grant MAT2000-1533-C03-03.

References

1. Haggerty, S., Growth of titanium and chromium strengthened sapphire fibers. Technical Report AFML-TR-73-2, *Air Force Materials Laboratory*, WPAFB, OH, 1972
2. Crane, R.L., An investigation of the mechanical properties of silicon carbide and sapphire filaments. Technical Report AFML-TR-72-180, *Air Force Materials Laboratory*, WPAFB, OH 1972
3. Sayir, H., Farmer, S.C., Lagerlof, K.P.D., Sayir, A., Temperature dependent fracture strength of doped single-crystal alumina fibers, in Advanced Ceramic-Matrix Composites II, Ed. J.P. Singh, N.P. Bansal, *Ceramic Transactions*, Vol. 73, 53-63 (1994)
4. Newcomb, S.A., Tressler, R.E., Slow crack growth in sapphire fibers at 800° to 1500°C, *J. Am Ceram Soc.*, 1993, 76, [10], 2505-2512
5. Sayir, A., Time dependent strength of sapphire fibers at high temperatures, *Adv. Ceram Matrix Composites*, 1993, 691-703

6. Heydt, P.E., Tressler, R.E., Sayir, A., Delayed failure of Cr³⁺-doped sapphire fibers, in Advances in Ceramic Composites III, Ceramic Transactions, Ed. N. Bansal and J.P. Singh, American Ceramic Society, Westerville, OH, 1996
7. McClellan, K.J., Sayir, H., Heuer, A.H., Sayir, A., Haggerty, J.S., Sigalovsky, J., High-temperature creep-resistant Y₂O₃-stabilized cubic ZrO₂ single-crystal fibers, in Advanced Ceramic-Matrix Composites II, Ed. J.P. Singh, N.P. Bansal, *Ceramic Transactions*, Vol. 73, 63-73 (1994)
8. Martinez-Fernández, J., Sayir, A., Farmer, S.C., High-temperature creep deformation of directionally solidified Al₂O₃/Er₃Al₅O₁₂, *Acta Mater.*, 2003, 51, 1705-1720
9. Wachtman, J.B., Mechanical Properties of Ceramics, Wiley, 1996
10. Quispe Cancapa, J.J., de Arellano Lopez, A.R., Sayir, A., High-temperature mechanical properties of directionally solidify Cr³⁺ sapphire fibers, *Ceram Engg. Sci. Proc.*, 2002, 23 [3] 665-673
11. Radford, K.C., Pratt, P.L., The mechanical properties of impurity-doped alumina single crystal, *British Ceramic Society*, 1970, 15, 185-202.
12. Pletka, M.L., Mitchell, T.E., Heuer, A.H., Strengthening mechanisms in sapphire, in Fracture Mechanics of Ceramics 1974, Vol.2, pp.181-194, Ed. R. Bradt et al., Plenum, NY.
13. Butt, M.Z., Feltham, P., Review of solid-solution hardening, *J. Mater. Sci.*, 1993, 28, 2557
14. Barsoum, M.W., Fundamentals of Ceramics, McGraw-Hill, 1997
15. Westfall, L., Sayir, A., Penn, W., System grows single-crystal fiber", *NASA Tech. Briefs*, 1994, 18, [8] 77
16. Bunting, E.N., Phase diagrams Al₂O₃-Cr₂O₃, *Bureau of Standards Journal of Research*, 1931, 6 [6] 948
17. CRC Handbook of Materials Science, Vol. I, Ed. C.T. Lynch, CRC Press, 1986
18. Åsteman, H., Svensson, J.E., Johansson, L.G., Norell, M., Indication of chromium-oxide hydroxide evaporation during oxidation of 304L at

- 873 K in the presence of 10-percent water-vapor, *Oxidation of Metals* 1999, 52 [1-2] 95-111
19. REFERENCE OF MICRO-PULL-DOWN TECHNIQUE
 20. Heydt, P.E., Master Thesis, Pennsylvania State University, 1996
 21. Quispe Cancapa, J.J., de Arellano Lopez, A.R., Sayir, A., Room- and high-temperature tensile fracture of directionally solidified chromia-doped sapphire fibers, in print in *Ceram Engg. Sci. Proc.*, 2003
 22. Quispe Cancapa, J.J., Master Thesis, Universidad de Sevilla, 2002
 23. Kotchick, D.M., Ph.D. Thesis, Pennsylvania State University, 1978
 24. Rice, R.W., in Fractography of Glasses and Ceramics, Ed. J.R. Varner, V.D. Frechette, *Avances in Ceramics*, Vol. 22, 3-56 (1986)
 25. Rice, R.W., Becher, P.F., Comment of creep deformation of 0° sapphire, *J. Am Ceram. Soc.*, 1977, 60 [3-4] 186-188
 26. Kirchner, H.P., Brittleness dependence of crack branching in ceramics, *J. Am Ceram. Soc.*, 1986, 89 [4] 339-342
 27. Firestone, R.F., Heuer, A. H., Creep deformation of 0° sapphire, *J. Am Ceram. Soc.*, 1976, 59, [1-2], 24-29
 28. Chandrasekaran, D., Solution hardening - a comparison of two models, *Mater. Sci. and Engg.*, 2001, A309-310, 184-189
 29. Wiederhorn, S.E., in Fracture Mechanics of Ceramics, 1974, Vol.2, pp. 613-646, Ed. R. Bradt et al., Plenum, NY.
 30. Chuang, T., A diffusive crack-growth model for creep fracture, *J. Am Ceram. Soc.*, 1982, 65 [2] 93-103
 31. Lawn, B.R., Physics of fracture, *J. Am Ceram Soc.*, 1983, 66 [2] 83-91
 32. Thomson, R., Hsieh, C., Rana, V., Lattice trapping of fracture cracks, *J. Appl. Phys.*, 1971, 42, 3154-3160.
 33. Castaing, J., Muñoz, A., Gome Garcia, D., Dominguez Rodriguez, A., Basal slip in sapphire (α -Al₂O₃), *Mater. Sci. and Engg.*, 1997, A233, 121-125

Table I. Fiber morphological and compositional characteristics*

	Diameter (μm)	Temperature ($^{\circ}\text{C}$)	Composition (Cr at%)	
			Interior	Exterior
Saphikon	140	25-1400		
NASA-L	120	25-1400		
NASA-H	110	25	0.8 ± 0.2	14.5 ± 6.0
		800	0.8 ± 0.2	13.5 ± 8.5
		1200	0.9 ± 0.1	6.0 ± 5.0
		1400	1.1 ± 0.1	1.1 ± 0.1

* Data for NASA-L fibers are taken from Heydt [20]

Table II. Comprehensive summary of mechanical results*

Fibers	25°C					800°C					1200°C					1400°C				
	σ (MPa.s ⁻¹)	α (MPa)	$\Delta\alpha$ (MPa)	N		σ (MPa.s ⁻¹)	α (MPa)	$\Delta\alpha$ (MPa)	N		σ (MPa.s ⁻¹)	α (MPa)	$\Delta\alpha$ (MPa)	N		σ (MPa.s ⁻¹)	α (MPa)	$\Delta\alpha$ (MPa)	N	
Saphikon	0.38	2572	630			0.3	987	119			0.3	659	58			0.37	487	51		
	35	2884	624	44		1.8	1050	79	24		1.8	752	70	19		5.0	582	51	13	
	950	3061	735			29.9	1189	236			29.9	836	60			41.5	675	13		
NASA-L	0.47	2683	650			0.2	1177	144												
	48	2966	788	45		35	1406	129	28											
	1274	3189	630																	
NASA-H	0.52	1674	198			0.31	730	221			0.28	447	95			0.5	397	67		
	44	1731	248	54		33	800	152	50		45	604	86	16		5.0	455	110	19	
	1353	1938	253													41.5	515	103		

* Results for NASA-L fibers at 1200 and 1400°C are taken from Heydt [20]

Figure Captions

Figure 1.- Energy-dispersive x-ray maps, for aluminum, chromium and oxygen, and corresponding secondary electron SEM micrograph of an as-fabricated NASA-H fiber. The accumulation of Cr on the exterior of the fiber is evident.

Figure 2.- Optical microscopy, SEM, and EDS mapping micrographs of NASA-H fibers cycled up to 800, 1200 and 1400°C. The morphology of the fiber is unchanged, but the volatilization of Cr is evident for 1200- and 1400°C-cycled fibers, both by the loose of deep-red color of the fibers (grey in the micrographs), and the absence of the Cr corona in the exterior of the fibers as seen in the EDS maps.

Figure 3.- Room-temperature tensile rupture results for (a) Saphikon, (b) NASA-L and (c) NASA-H fibers.

Figure 4.- 800°C tensile rupture results for (a) Saphikon, (b) NASA-L and (c) NASA-H fibers.

Figure 5.- 1200°C tensile rupture results for (a) Saphikon and (b) NASA-H fibers.

Figure 6.- 1400°C tensile rupture results for (a) Saphikon and (b) NASA-H fibers.

Figure 7.- SEM micrographs of fracture surfaces of (a) Saphikon, (b) NASA-L and (c) NASA-H fibers fractured at room-temperature.